PONTIFÍCIA UNIVERSIDADE CATÓLICA
DO RIO DE JANEIRO

**Julio de Lima Nicolini**

# Investigation of Electromagnetic Propagation in Plasma Structures Through Eigenfunction Expansions and FDTD Techniques

**Dissertação de Mestrado**

Dissertation presented to the Programa de Pós–Graduação em Engenharia Elétrica of PUC-Rio in partial fulfilment of the requirements for the degree of Masters em Engenharia Elétrica.

Adviser: Prof. José Ricardo Bergmann

Rio de Janeiro
March 2017

PONTIFÍCIA UNIVERSIDADE CATÓLICA
DO RIO DE JANEIRO

**Julio de Lima Nicolini**

# Investigation of Electromagnetic Propagation in Plasma Structures Through Eigenfunction Expansions and FDTD Techniques

Dissertation presented to the Programa de Pós–Graduação em Engenharia Elétrica of PUC-Rio in partial fulfilment of the requirements for the degree of Masters em Engenharia Elétrica. Approved by the undersigned Examination Committee.

**Prof. José Ricardo Bergmann**
Adviser
Centro de Estudos em Telecomunicações – PUC-Rio

**Prof. Flavio Jose Vieira Hasselmann**
Centro de Estudos em Telecomunicações – PUC-Rio

**Prof. Marcela Silva Novo**
Departamento de Engenharia Elétrica – UFBA

**Prof. Márcio da Silveira Carvalho**
Vice Dean of Graduate Studies
Centro Técnico Científico – PUC-Rio

Rio de Janeiro, March 17, 2017

**Julio de Lima Nicolini**

Received the Bachelor of Science degree in Electrical Engineering from the Pontifícia Universidade Católica do Rio de Janeiro (Rio de Janeiro, Brazil) in 2015. Research interests include topics in mathematical physics, nuclear fusion, plasma physics and computational electromagnetics.

Bibliographic data

Nicolini, Julio de Lima

Investigation of Electromagnetic Propagation in Plasma Structures Through Eigenfunction Expansions and FDTD Techniques / Julio de Lima Nicolini; adviser: José Ricardo Bergmann. – 2017.

v., 125 f: il. color. ; 30 cm

Dissertação (mestrado) - Pontifícia Universidade Católica do Rio de Janeiro, Departamento de Engenharia Elétrica.

Inclui bibliografia

1. Engenharia Elétrica – Teses. 2. Eletromagnetismo Computacional. 3. Física de Plasmas. 4. Propagação em Plasmas. 5. Casamento de Modos. 6. Expansão em Autofunções. 7. Método das Diferenças Finitas no Domínio do Tempo. I. Bergmann, José Ricardo. II. Pontifícia Universidade Católica do Rio de Janeiro. Departamento de Engenharia Elétrica. III. Título.

CDD: 621.3

# Acknowledgements

I would like to thank, in no particular order,

- my adviser, prof. José Ricardo Bergmann, for his friendship, wisdom and advice;
- CNPq and PUC-Rio, for the scholarships and infrastructure without which this work could not have been completed;
- my parents, without whom I would not be here;
- my friend Isabela, for the companionship and emotional support without which these two years would have been much harder;
- my friend Tiana, for her patience with my incessant English questions and for putting up with my daily antics;
- my friends Adell, Daniel, Kateland and Thomas, for brightening my days and proving that friendship transcends geographical distance;
- my friend and colleague Lucianno, for many engaging conversations on mathematical physics and for his help with displaying data and typesetting documents;
- my friend and colleague Michael, for many interesting discussions on fundamental physics concepts and for his help revising some aspects of the text;
- my friend and colleague Guilherme, for many engaging conversations on numerical algorithms and electromagnetism, and also for the research work we have performed together;
- my teachers from the Dept. of Electrical Engineering, for everything they have taught me over the years, and particularly prof. Flavio, for the research work we have performed together;
- my friends and colleagues from the Dept. of Physics and the Dept. of Electrical Engineering, for many fruitful discussions and for their companionship during these two years;
- the students I was responsible for teaching in undergraduate classes, for constantly making me re-evaluate preconceived notions and confirming my love for teaching.

# Abstract

Nicolini, Julio de Lima; Bergmann, José Ricardo (Adviser). **Investigation of Electromagnetic Propagation in Plasma Structures Through Eigenfunction Expansions and FDTD Techniques**. Rio de Janeiro, 2017. 125p. Dissertação de Mestrado – Centro de Estudos em Telecomunicações, Pontifícia Universidade Católica do Rio de Janeiro.

Plasma is one of the four fundamental states of matter, present on Earth in natural form at the ionosphere, in lightning strikes and in the flames resulting from combustion, as well as in artificial form in neon signs, fluorescent light bulbs and industrial processes. Plasma behaviour is extraordinarily complex and varied, e.g. the spontaneous formation of interesting spatial features over a wide range of length scales. A plasma antenna, on the other hand, is a radiating structure based in a plasma element instead of a metallic conductor, which creates several technological advantages and useful characteristics. In this present work, an investigation of electromagnetic propagation inside of plasma structures is performed through both theoretical and numerical means as a first step towards constructing appropriate models for the study of plasma antennas.

# Keywords

Computational Electromagnetics; Plasma Physics; Plasma Propagation; Mode Matching; Eigenfunction Expansion; Finite-Differences Time-Domain Method.

# Resumo

Nicolini, Julio de Lima; Bergmann, José Ricardo. **Investigação de Propagação Eletromagnética em Estruturas de Plasma Através de Expansões em Autofunções e Técnicas FDTD**. Rio de Janeiro, 2017. 125p. Dissertação de Mestrado – Centro de Estudos em Telecomunicações, Pontifícia Universidade Católica do Rio de Janeiro.

Plasma é um dos quatro estados fundamentais da matéria, presente em forma natural na Terra na ionosfera, em relâmpagos e nas chamas resultantes de combustão, assim como em forma artificial em lâmpadas de neônio, lâmpadas fluorescentes e processos industriais. O comportamento de plasmas é extraordinariamente complexo e variado, como por exemplo a formação espontânea de características espaciais interessantes em variadas escalas diferentes de comprimento. Uma antena de plasma, por sua vez, é uma estrutura radiante baseada em um elemento de plasma em vez de um condutor metálico, o que gera diversas vantagens e características úteis de um ponto de vista tecnológico. Nesse presente trabalho, uma investigação da propagação eletromagnética dentro de estruturas de plasma é realizada através de métodos teóricos e numéricos como um primeiro passo em direção ao desenvolvimento de modelos apropriados para o estudo de antenas de plasma.

# Palavras-chave

Eletromagnetismo Computacional; Física de Plasmas; Propagação em Plasmas; Casamento de Modos; Expansão em Autofunções; Método das Diferenças Finitas no Domínio do Tempo.

# Table of contents

# List of figures

# List of tables

# 1
# Introduction

A plasma dipole is an antenna with a radiating structure based on a plasma element instead of a metallic conductor [1–4]. The plasma, kept activated by an ionizing source, is the conducting material that acts as the source for electromagnetic fields, which can then be modulated and used to carry information in telecommunication links. This is achieved by applying a secondary signal source to the plasma, which will then re-emit the signal as electromagnetic radiation.

One possible set-up for a plasma antenna is shown in figure 1.1, which is the same structure used in [3], to exemplify the operation of one such device. A thin dielectric shell containing an inert gas is inserted in a grounded metallic cage, with the ionizing and signal sources connected to the hidden portion of the cylinder. The ionizing source is a copper collar that carries the electromagnetic excitation necessary to ionize the gas within the dielectric cylinder. The basic mechanism is that a strong-intensity electric field is created between the collar and the grounded metallic shielding, allowing for a process of ionization to begin in the plasma if the electric field intensity is higher than the dielectric breakdown voltage of the gas. This ionization process is carried throughout the whole column and then maintained by a surface wave travelling through the dielectric cylinder [5,6].

The metallic shielding also blocks electromagnetic interference from the outside from affecting the sources, as well as preventing spurious radiation from the collars from affecting measurements. The signal source is a copper collar that transfers a desired transmitted signal into the plasma, or detects a received signal from the plasma and into an analyser. The part of the plasma column that is not shielded can act as a transmitting/receiving dipole antenna when the reflective effect of the metallic box is taken into account.

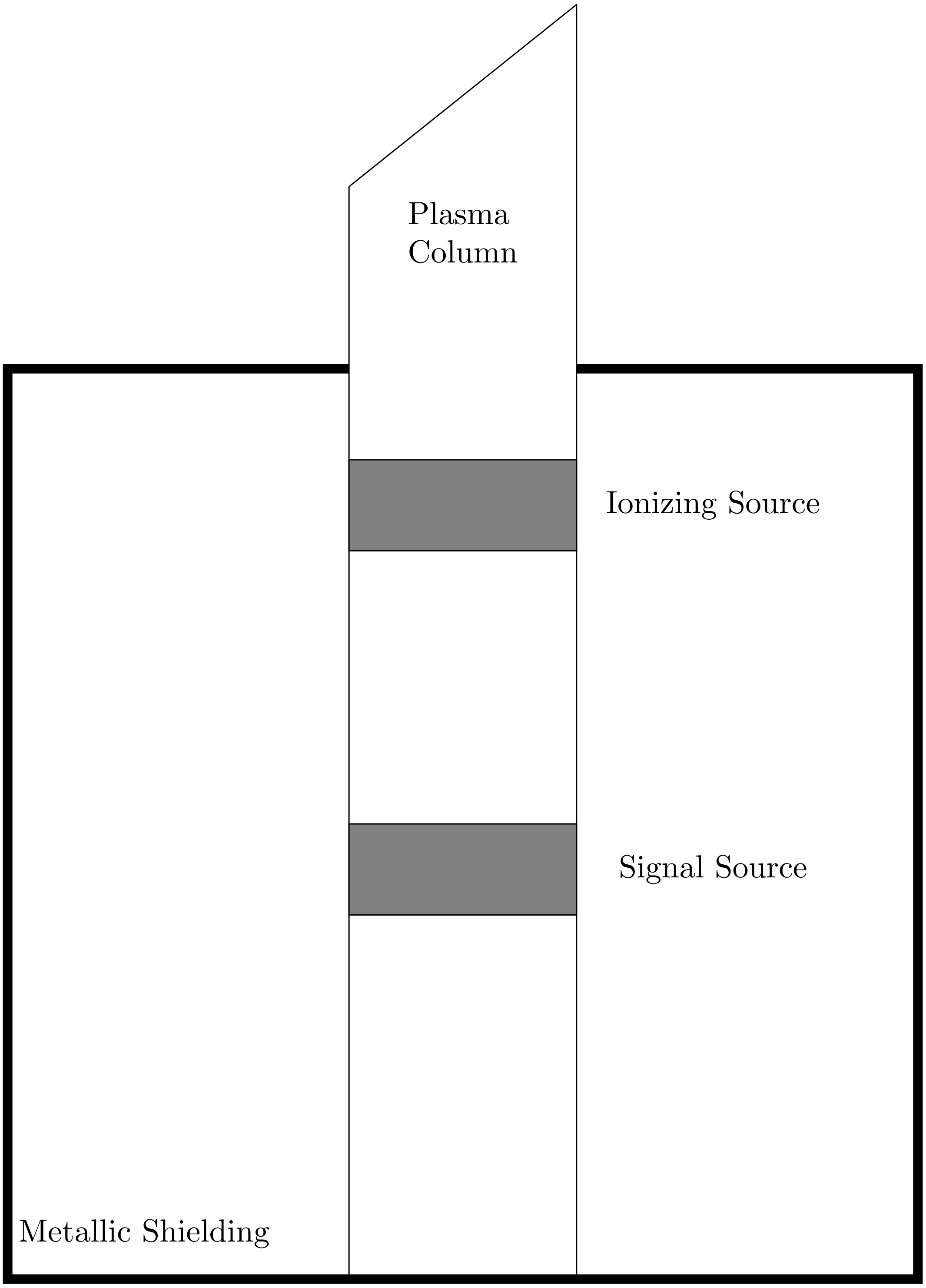

Figure 1.1: Possible set-up for a plasma antenna configuration. The ionizing source is a copper collar that carries the electromagnetic excitation necessary to ionize the gas within the dielectric cylinder. The signal source is a copper collar that transfers a desired transmitted signal into the plasma, or detects a received signal from the plasma and into an analyser. The metallic shielding blocks electromagnetic interference from the outside from affecting the sources, as well as prevents spurious radiation from the collars from affecting measurements.

One of the advantages of plasma antennas is that, differently from their metallic counterparts, their physical characteristics (and therefore their radiation characteristics) can be controlled through the parameters of the ionizing source. This results in an antenna that is not restricted to its original fabrication characteristics, and that can be reconfigured with simplicity and in real time [7, 8]. Additionally, if the ionizing source is turned off, the plasma antenna is deactivated, becoming an inert element that is invisible to electromagnetic radiation, eliminating coupling problems with other antenna elements.

One of the great challenges in the synthesis of antennas for telecommunication links is the lack of flexibility in changing parameters, like for example the radiation pattern, once the antenna is ready. This problem can be avoided by application of antenna arrays, where control over the excitation of each element allows the radiation pattern to be conformed. These antenna arrays are particularly interesting for use in reconfigurable antennas in mobile communications and satellite link applications [9–11], but the presence of metallic elements creates additional complexity in the synthesis process due to parasitic interactions. Plasma antennas provide an alternative to metallic elements in these arrays, as they remain inert when deactivated and therefore parasitic interactions are minimized.

Despite the advantages in utilizing plasmas as conducting elements in antennas, there are still several difficulties and obstacles for this technology. Obtaining the real characteristics of a plasma antenna, in a generic situation, requires the complete description of the plasma configuration [8], which creates theoretical and numerical difficulties when trying to analyse such systems. In particular, the behaviour of electromagnetic waves within a plasma structure is not always trivial to be analysed.

In light of these difficulties, this work seeks to investigate electromagnetic propagation inside of plasma structures through both theoretical and numerical means as a first step towards constructing appropriate models for the study of plasma antennas.

The rest of this work is organized as follows.

Chapter 2 presents some fundamental concepts of plasma physics, as well as different ways to model the plasma structures of interest. Of note is the dielectric description of plasmas, which can be readily incorporated into the standard theory of computational electromagnetics.

Chapter 3 provides an analytical formulation to study electromagnetic propagation through homogeneous and inhomogeneous dielectric cylinders in which the fields are expanded in a basis of eigenfunctions. This method will be utilized to validate the numerical simulations presented in later chapters.

Chapter 4 presents the basic concepts of numerical simulations performed with a Finite Differences Time Domain (FDTD) method, as well as the details necessary to perform FDTD simulations of the problem under consideration.

Chapter 5 provides validating results for both the eigenfunction method and the FDTD simulations presented in previous chapters, as well as results that explore the characteristics of electromagnetic propagation through plasma.

Finally, chapter 6 presents the concluding remarks and future perspectives for this work.

# 2
# Plasma Fundamentals

Plasma is one of the four fundamental states of matter, and the most abundant ordinary matter in the universe, most of which is found in rarefied intergalactic regions and in stars, including the Sun. It is also present on Earth in natural form at the ionosphere, in lightning strikes and in the flames resulting from combustion, as well as in artificial form in neon signs, fluorescent light bulbs and industrial processes, to name a few examples. Plasma behaviour is extraordinarily complex and varied, e.g. the spontaneous formation of interesting spatial features over a wide range of length scales. This complexity in observed phenomena motivates the usage of various models to theoretically describe plasmas; some of these will be briefly presented in this chapter.

## 2.1
## Particle Description

One way to model a plasma is to treat each particle in the ionized gas separately, applying Newton's laws of motion to each individual electron, ion and neutral charge, and using the Lorentz force

$$\vec{F} = q[\vec{E} + (\vec{v} \times \vec{B})] \tag{2-1}$$

as the coupling between the mechanical dynamics of the system and the electromagnetic behaviour prescribed by Maxwell's equations. This model is perhaps the most direct of plasma models, as there are no simplifications or assumptions being made.

Despite its apparent simplicity, the particle description has limitations for either analytical or numerical treatment of most practical problems, as the number of particles in an usual plasma device (say, a photonic crystal) or an usual region (say, a part of the ionosphere or the region within a gas discharge tube) is upwards of $10^{20}$ electrons and ions [12]. Analytical treatment of so many particles becomes unwieldy, and despite advances in computational hardware and simulation software, it doesn't seem likely that computers will have enough memory to store all the necessary information in the foreseeable future, preventing numerical treatment as well. Particle-in-Cell (PIC) simulation methods use “macroparticles” that represent a large number of actual particles to try and circumvent this limitation, but computational restrictions still exist.

## 2.2
## Kinetic Theory and Magnetohydrodynamics

Another avenue is to treat plasmas as dynamic systems in the context of kinetic theory, ascribing a distribution function $f_s$ to represent particles of type $s$ (electrons, ions or neutral charges) and treating the plasma as a thermodynamic system [13]. The time evolution of such a system obeys the Boltzmann equation, which states that the total rate of change in the distribution function of each species is given by a collision term,

$$\frac{\mathrm{d}f_s}{\mathrm{d}t} = \left(\frac{\partial f_s}{\partial t}\right)_c, \tag{2-2}$$

where the subscript $s$ stands for each species type (electrons, ions, neutral charges). Since $f = f(\vec{x}, \vec{v}, t)$ is a time-dependent function in six-dimensional phase space[1], the left hand side of the equation can be expanded,

$$\frac{\partial f_s}{\partial t} + \vec{v} \cdot \nabla_x f_s + \frac{\vec{F}}{m_s} \cdot \nabla_v f_s = \left(\frac{\partial f_s}{\partial t}\right)_c, \tag{2-3}$$

where $m_s$ is the species’ mass, $\vec{F}$ is the total instantaneous force applied to the particle, $\vec{v}$ is the instantaneous velocity of the particle, $\nabla_x$ is the gradient in position space and $\nabla_v$ is the gradient in velocity space.

The distribution function $f_s$ can be seen as a time-varying functional distribution in the six-dimensional phase space $(x, y, z, v_x, v_y, v_z)$ of a single particle of type $s$ in the plasma system, i.e. a point $f_s(x_0, y_0, z_0, v_{0x}, v_{0y}, v_{0z}, t_0)$ represents the probability of finding a particle of type $s$ in a neighbourhood of $(x_0, y_0, z_0)$ with approximate velocity $(v_{0x}, v_{0y}, v_{0z})$ at time $t_0$, or the number of particles of type $s$ in a neighbourhood of $(x_0, y_0, z_0)$ with approximate velocity $(v_{0x}, v_{0y}, v_{0z})$ at time $t_0$, depending on chosen normalization for $f$. The use of this one-particle distribution function to describe macroscopic quantities and collective phenomena is well supported by the literature [13,14]. While the $xyz$ coordinate system and the $v_x v_y v_z$ velocity system have been used so far, the

---

[1] “Phase space” is the name given to a space which represents all the possible states of a system under consideration, with each possible state corresponding to one unique point in the phase space. For a plasma, the phase space comprises the set of possible positions and velocities for its particles.

more general approach is to take $f$ as a function of generalized coordinates $\vec{q}$ and generalized momenta $\vec{p}$.

Choosing to normalize by density, the constitutive relation for the total number of particles of type $s$ in the plasma is given by

$$N_s(t) = \int \mathrm{d}x\mathrm{d}y\mathrm{d}z\mathrm{d}v_x\mathrm{d}v_y\mathrm{d}v_z f_s(x,y,z,v_x,v_y,v_z,t) = \int f_s(\vec{x},\vec{v},t)\mathrm{d}^3\vec{x}\mathrm{d}^3\vec{v}, \tag{2-4}$$

where $\mathrm{d}^3\vec{x}$ is taken to mean "the volume element of three-dimensional coordinate space" and $\mathrm{d}^3\vec{v}$ is taken to mean "the volume element of three-dimensional velocity space". This is intuitive, as the sum of all possible particle velocities values in all possible coordinate points must yield the total number of particles up to a normalization constant, which was chosen to be unity. From equation (2-4) a local particle density can be defined as

$$n_s(\vec{x},t) = \int f_s(\vec{x},\vec{v},t)\mathrm{d}^3\vec{v}, \tag{2-5}$$

which allows for the definition of a local expectation value for any operator $O(\vec{x},\vec{v},t)$ as

$$\langle O(\vec{x},t)\rangle = \frac{1}{n(\vec{x},t)}\int f(\vec{x},\vec{v},t)O(\vec{x},\vec{v},t)\mathrm{d}^3\vec{v}. \tag{2-6}$$

With (2-6), another useful quantity can be defined: the local flow velocity $\vec{u}_s$, which represents the bulk movement of the species, as

$$\vec{u}_s(\vec{x},t) = \langle\vec{v}_s\rangle = \frac{1}{n_s(\vec{x},t)}\int \vec{v}_s f_s(\vec{x},\vec{v},t)\mathrm{d}^3\vec{v}. \tag{2-7}$$

The electromagnetic description is given by the microscopic Maxwell's equations,

$$\nabla\cdot\vec{E} = \frac{\rho}{\epsilon_0}, \tag{2-8a}$$

$$\nabla\cdot\vec{B} = 0, \tag{2-8b}$$

$$\nabla\times\vec{E} = -\frac{\partial\vec{B}}{\partial t}, \tag{2-8c}$$

$$\nabla\times\vec{B} = \mu_0\vec{J} + \mu_0\epsilon_0\frac{\partial\vec{E}}{\partial t}. \tag{2-8d}$$

The coupling between the mechanical and electromagnetic dynamics is present both in the force term of the Boltzmann equation, which takes the form of the Lorentz force[2], and in the constitutive relations given by

$$\rho = \int \sum_s q_s f_s \mathrm{d}^3\vec{v} = \sum_s q_s n_s, \tag{2-9a}$$

$$\vec{J} = \int \sum_s q_s f_s \vec{v}_s \mathrm{d}^3\vec{v} = \sum_s q_s n_s \vec{u}_s, \tag{2-9b}$$

where the spatial and temporal dependences have been left implicit, $q_s$ is the electrical charge of a single particle of species $s$, and the summations are done over all different species present in the plasma.

The Boltzmann equation can be simplified as done first by Vlasov [15]. First, consider the rest mass of the species present in the plasma. Protons have a rest mass that is 1836.15 times greater than that of an electron, and the ions in a typical plasma are composed of several protons. Therefore, ions can be approximated as stationary positive charges, and the only species that will act as a fluid will be the electrons.

Second, consider the interactions these electrons will suffer as they flow through the plasma. Considering the system isolated from any external forces, interactions between particles will occur only through short-distance collisions and long-range Coulomb interactions. Vlasov's argument is that, for an electron fluid under typical plasma conditions, Coulomb interactions will dominate, and therefore the collision term on the right-hand side of the Boltzmann equation can be neglected.

Thus the modified Boltzmann equation, commonly called the Vlasov equation, is given by

$$\frac{\partial f_e}{\partial t} + \vec{v} \cdot \nabla_x f_e + \frac{q_e}{m_e}[\vec{E} + (\vec{v} \times \vec{B})] \cdot \nabla_v f_e = 0, \tag{2-10}$$

and the constitutive relations reduce to

$$\rho = q_e n_e, \tag{2-11a}$$

$$\vec{J} = q_e n_e \vec{u}_e. \tag{2-11b}$$

The Vlasov equation is useful in describing the plasma situation for when a steady-state discharge has been reached, and there are no further ionization processes. To model ionization, a different equation should be used, such as the Fokker-Planck equation [16].

The problem has been reduced to the microscopic distribution function of a single particle, but it can still be a complicated function to evaluate

---

[2] Gravitational forces can be neglected as their intensity are orders of magnitude smaller than the intensity of electromagnetic interactions.

and work with. The coupling between the dynamics is made through the macroscopic quantities $n_e$ and $\vec{u}_e$, so it is worthwhile to try and recast the Vlasov equation using macroscopic variables, which gives rise to the theory of magnetohydrodynamics, or the fluid description for plasmas. This can be done by computing the moments of the Vlasov equation. Since only electrons will be considered from here onwards, the species' subscript for each quantity will be dropped.

The first step is to integrate the Vlasov equation over the entire momentum space,

$$\int \left[ \frac{\partial f}{\partial t} + \frac{\vec{p}}{m} \cdot \nabla f + q[\vec{E} + (\vec{v} \times \vec{B})] \cdot \frac{\partial f}{\partial \vec{p}} \right] \mathrm{d}^3\vec{p} = 0. \tag{2-12}$$

The first term is given by

$$\int \frac{\partial f}{\partial t} \mathrm{d}^3\vec{p} = \frac{\partial}{\partial t} \int f \mathrm{d}^3\vec{p} = \frac{\partial n}{\partial t}. \tag{2-13}$$

For the second term, $\vec{p}$ and $\vec{q}$ are independent variables in phase space, so the operator $\nabla$ does not affect the momentum and it can be written

$$\int \frac{\vec{p}}{m} \cdot \nabla f \mathrm{d}^3\vec{p} = \int \nabla \cdot \left( \frac{\vec{p}}{m} f \right) \mathrm{d}^3\vec{p} = \nabla \cdot \int \left( \frac{\vec{p}}{m} f \right) \mathrm{d}^3\vec{p}. \tag{2-14}$$

To evaluate the integral, the canonical momentum of a moving charged particle is explicitly given by [17]

$$\vec{p} = \frac{m\vec{v}}{\sqrt{1 - \frac{v^2}{c^2}}} + \frac{q}{c}\vec{A}, \tag{2-15}$$

where $\vec{A}$ is the vector potential, $c$ is the speed of light and the first term is the relativistic correction of the classical linear momentum. Taking the classical limit $v \ll c$, the electron's canonical momentum simplifies to the usual expression at first order and it can be written

$$\nabla \cdot \int \left( \frac{\vec{p}}{m} f \right) \mathrm{d}^3\vec{p} = \nabla \cdot \int \vec{v} f \mathrm{d}^3\vec{p} = \nabla \cdot (n\vec{u}). \tag{2-16}$$

For the electric force term,

$$\int q\vec{E} \cdot \frac{\partial f}{\partial \vec{p}} \mathrm{d}^3\vec{p} = \int \frac{\partial}{\partial \vec{p}} \cdot (q\vec{E}f) \mathrm{d}^3\vec{p}, \tag{2-17}$$

since the electrical field is independent of the particle's velocity. Applying the divergence theorem in velocity space on equation (2-17),

$$\int \frac{\partial}{\partial \vec{p}} \cdot (q\vec{E}f)\mathrm{d}^3\vec{p} = \oint (q\vec{E}f) \cdot \mathrm{d}S = \int (qf\vec{E} \cdot \vec{s})|\vec{v}|^2 \mathrm{d}\Omega, \tag{2-18}$$

where the contour is closed at infinity and $\vec{s}$ is the outward unitary vector on the surface. Thus, if $|f| \to 0$ faster than $\frac{1}{|\vec{v}|^2}$ as $|\vec{v}| \to \infty$, as required for $f$ to be a distribution with finite energy, this term's contribution is zero.

For the magnetic force term, the vector identity $\nabla \cdot (f\vec{C}) = f\nabla \cdot \vec{C} + \vec{C} \cdot \nabla f$ can be used to write

$$\int q(\vec{v} \times \vec{B}) \cdot \frac{\partial f}{\partial \vec{p}} \mathrm{d}^3\vec{p} = \int \left[ \frac{\partial}{\partial \vec{p}} \cdot [fq(\vec{v} \times \vec{B})] - f\frac{\partial}{\partial \vec{p}} \cdot (q\vec{v} \times \vec{B}) \right] \mathrm{d}^3\vec{p}, \tag{2-19}$$

where the second term vanishes because $\vec{v} \times \vec{B}$ is perpendicular to $\vec{v}$, and therefore perpendicular to the operator $\frac{\partial}{\partial \vec{p}}$. For the first term, the divergence theorem can be applied as was done in equation (2-18). Now, however, because of the $\vec{v}$ factor in the vectorial product, the distribution function must fall off faster than $\frac{1}{|\vec{v}|^3}$ as $|\vec{v}| \to \infty$. While this is not necessarily true for all possible functions, it is true for Maxwellian distributions (which fall to zero faster than any polynomial). Since the Maxwellian is the equilibrium distribution, this condition's validity can be safely assumed for stable plasma systems.

Collecting terms,

$$\frac{\partial n}{\partial t} + \nabla \cdot (n\vec{u}) = 0, \tag{2-20}$$

which is the continuity equation for the plasma system.

Now, to obtain the first moment of the Vlasov equation, eq. (2-10) is multiplied by $\vec{p}$ and integrated over momentum space,

$$\int \left[ \vec{p}\frac{\partial f}{\partial t} + \vec{p}\frac{\vec{p}}{m} \cdot \nabla f + \vec{p}q[\vec{E} + (\vec{v} \times \vec{B})] \cdot \frac{\partial f}{\partial \vec{p}} \right] \mathrm{d}^3\vec{p} = 0. \tag{2-21}$$

For the first term,

$$\begin{aligned} \int \left( \vec{p}\frac{\partial f}{\partial t} \right) \mathrm{d}^3\vec{p} &= m\frac{\partial}{\partial t} \int (\vec{v}f)\, \mathrm{d}^3\vec{p}, \\ &= m\frac{\partial}{\partial t}(n\vec{u}), \\ &= m\vec{u}\frac{\partial n}{\partial t} + mn\frac{\partial \vec{u}}{\partial t}, \end{aligned} \tag{2-22}$$

where the factor $\vec{p}$ could be taken inside the time derivative because $\vec{p}$ denotes independent variables in phase space, and thus are unrelated to the variable

$t$. This can be shown formally through Lagrangian mechanics [18] or through probability theory [19], as the Vlasov equation is a statistical description of an ensemble.

For the second term,

$$\int \left( \vec{p}\frac{\vec{p}}{m} \cdot \nabla f \right) \mathrm{d}^3\vec{p} = m\nabla \cdot \int (\vec{v}\vec{v}f)\mathrm{d}^3\vec{p}, \tag{2-23}$$

from which (2-6) can be applied to obtain

$$\int \left( \vec{p}\frac{\vec{p}}{m} \cdot \nabla f \right) \mathrm{d}^3\vec{p} = m\nabla \cdot \langle n\vec{v}\vec{v} \rangle . \tag{2-24}$$

Now the particle's velocity $\vec{v}$ is separated into its fluid and thermal components, $\vec{v} = \vec{u} + \vec{w}$. From the linearity of expected values,

$$\begin{aligned} m\nabla \cdot \langle n\vec{v}\vec{v} \rangle &= m\nabla \cdot \left( n\vec{u}\vec{u} + n\vec{u} \langle \vec{w} \rangle + n \langle \vec{w} \rangle \vec{u} + n \langle \vec{w}\vec{w} \rangle \right), \\ &= m\nabla \cdot \left( n\vec{u}\vec{u} + n \langle \vec{w}\vec{w} \rangle \right), \\ &= \nabla \cdot (mn\vec{u}\vec{u}) + \nabla \cdot (mn \langle \vec{w}\vec{w} \rangle), \end{aligned} \tag{2-25}$$

where the fact that the average thermal velocity is zero was used. The first term in (2-25) can be rewritten

$$\begin{aligned} \nabla \cdot (mn\vec{u}\vec{u}) &= \nabla \cdot (mnu_x\vec{u} + mnu_y\vec{u} + mnu_z\vec{u}) , \\ &= \frac{\partial}{\partial x}(mnu_x\vec{u}) + \frac{\partial}{\partial y}(mnu_y\vec{u}) + \frac{\partial}{\partial z}(mnu_z\vec{u}), \\ &= \frac{\partial}{\partial x}(mnu_x)\vec{u} + mnu_x\frac{\partial}{\partial x}\vec{u} + \frac{\partial}{\partial y}(mnu_y)\vec{u} + \\ &\quad + mnu_y\frac{\partial}{\partial y}\vec{u} + \frac{\partial}{\partial z}(mnu_z)\vec{u} + mnu_z\frac{\partial}{\partial z}\vec{u}, \\ &= \nabla \cdot (mn\vec{u})\vec{u} + mn(\vec{u} \cdot \nabla)\vec{u}. \end{aligned} \tag{2-26}$$

Using the continuity equation (2-20) for the divergence term,

$$\nabla \cdot (mn\vec{u}\vec{u}) = -m\frac{\partial n}{\partial t}\vec{u} + mn(\vec{u} \cdot \nabla)\vec{u}. \tag{2-27}$$

For the second term of (2-25), average of the product of the thermal velocities is recognized as a tensor of type (0,2), commonly called the *kinetic pressure dyad* [20], given by

$$\mathcal{P} = mn \langle \vec{w}\vec{w} \rangle , \tag{2-28}$$

so that the second term of the first moment of the Vlasov equation can be written as

$$\int \left( \vec{p}\frac{\vec{p}}{m_e} \cdot \nabla f_e \right) \mathrm{d}^3\vec{p} = -m\frac{\partial n}{\partial t}\vec{u} + mn(\vec{u}\cdot\nabla)\vec{u} + \nabla\cdot\mathcal{P}. \tag{2-29}$$

For the electric force term,

$$\begin{aligned}
\int \left( \vec{p}q\vec{E}\cdot\frac{\partial f}{\partial \vec{p}} \right) \mathrm{d}^3\vec{p} &= \int \left( q\vec{E}\frac{\partial}{\partial\vec{p}}\cdot(\vec{p}f) - q\vec{E}f\cdot\frac{\partial\vec{p}}{\partial\vec{p}} \right) \mathrm{d}^3\vec{p}, \\
&= \int \left( \frac{\partial}{\partial\vec{p}}\cdot(q\vec{E}\vec{p}f) \right) \mathrm{d}^3\vec{p} - \int \left( q\vec{E}f \right) \mathrm{d}^3\vec{p}, \\
&= \oint (q\vec{E}\vec{p}f)\cdot\mathrm{d}S - q\vec{E}n,
\end{aligned} \tag{2-30}$$

where the surface integral vanishes for the same reasons as before.

For the magnetic force term,

$$\begin{aligned}
\int \left( \vec{p}q(\vec{v}\times\vec{B})\cdot\frac{\partial f}{\partial\vec{p}} \right) \mathrm{d}^3\vec{p} &= \int \left( q\frac{\partial}{\partial\vec{p}}\cdot\left[\vec{p}(\vec{v}\times\vec{B})f\right] - qf\vec{p}\frac{\partial}{\partial\vec{p}}\cdot(\vec{v}\times\vec{B}) \right. \\
&\qquad \left. - qf(\vec{v}\times\vec{B})\cdot\frac{\partial\vec{p}}{\partial\vec{p}} \right) \mathrm{d}^3\vec{p}, \\
&= -qn(\vec{u}\times\vec{B}),
\end{aligned} \tag{2-31}$$

where the two first integrals vanished for the same reasons as in eq. (2-19).

Collecting terms,

$$mn\left(\frac{\partial}{\partial t} + \vec{u}\cdot\nabla\right)\vec{u} + \nabla\cdot\mathcal{P} = qn(\vec{E} + \vec{u}\times\vec{B}), \tag{2-32}$$

which is the equation of motion for the plasma system, and the fundamental equation of magnetohydrodynamics. The same process can be used to derive similar equations of motion for other species, if they are being considered.

The next moment of the Vlasov equation can be obtained by multiplying it by the kinetic energy term $\frac{m\vec{v}\vec{v}}{2}$ and integrating over the momentum space to obtain the equation of energy transfer. However, a simplifying assumption that can sometimes be made is that there is no heat transfer within the plasma. Then, the energy transfer equation can be ignored, as its terms will all vanish. This also means ignoring effects from the thermal motion of the particles and the force generated by the diverging pressures within the plasma i.e. setting the term $\nabla\cdot\mathcal{P}$ to zero. This is called the *cold plasma model.*

The relevant equations that govern the cold plasma system are therefore given by

$$\nabla \times \vec{E} = -\frac{\partial \vec{B}}{\partial t}, \tag{2-33a}$$

$$\nabla \times \vec{B} = \mu_0 q_e n \vec{u} + \mu_0 \epsilon_0 \frac{\partial \vec{E}}{\partial t}, \tag{2-33b}$$

$$\frac{\partial n}{\partial t} + \nabla \cdot (n\vec{u}) = 0, \tag{2-33c}$$

$$m_e \left( \frac{\partial}{\partial t} + \vec{u} \cdot \nabla \right) \vec{u} = q_e (\vec{E} + \vec{u} \times \vec{B}). \tag{2-33d}$$

Another important parameter that can be defined through kinetic theory for collisional plasmas, and that will be important in the dielectric description presented in the following section, is the electron collision frequency $\nu$, i.e. the frequency in which electrons collide with others electrons.

To define $\nu$, consider a differential volume $\mathrm{d}^3\vec{x}$ containing electrons at density given by $n$, i.e. there are $n$ electrons per unit volume. Consider also that these electrons are opaque spheres with cross-sectional area given by $\sigma(\vec{v})$. The effective area within the differential volume that is blocked by electrons is then given by $n\sigma(\vec{v})$.

If the flux of incoming electrons travelling through a differential length $\mathrm{d}l$ in the plasma is given by $\Gamma$ and assuming that the plasma is isotropic, then the flux of outgoing electrons is given by $\Gamma_{out} = (1 - n\sigma(\vec{v})\mathrm{d}l)\Gamma$; this situation is depicted in figure 2.1.

The change in flux is thus given by

$$\mathrm{d}\Gamma = \Gamma_{out} - \Gamma = -n\sigma(\vec{v})\mathrm{d}l\Gamma, \tag{2-34}$$

so that

$$\frac{\mathrm{d}\Gamma}{\mathrm{d}l} = -n\sigma(\vec{v})\Gamma, \tag{2-35}$$

and the flux after travelling some length $l$ in the plasma is given by

$$\Gamma(l) = \Gamma_{in} e^{-n\sigma(\vec{v})l} = \Gamma_{in} e^{-\frac{l}{\lambda}}. \tag{2-36}$$

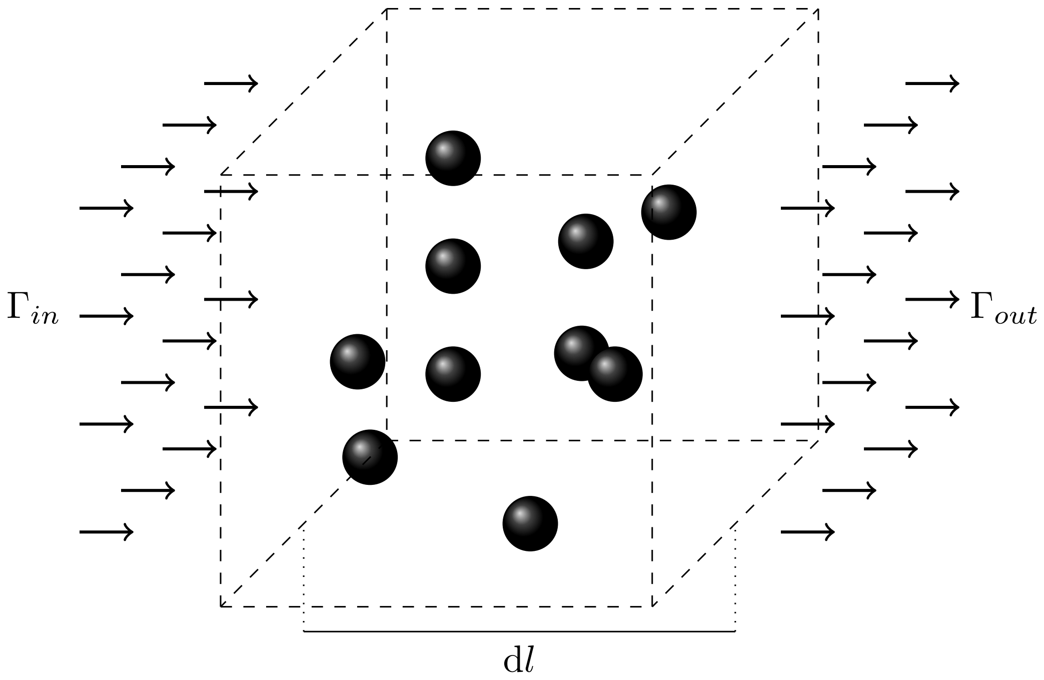

Figure 2.1: Electron flux $\Gamma$ travelling through a differential length d$l$ in isotropic plasma. Electrons within the differential volume element shown are depicted as opaque spheres and are characterized by a density $n$ and cross-sectional area $\sigma(\vec{v})$.

The quantity $\lambda = \frac{1}{n\sigma(\vec{v})}$ is the mean free path for a collision, which is in other words the mean distance an electron travels before experiencing a collision. For electrons with velocity $\vec{v}$, the mean time $\tau(\vec{v})$ between collisions is then given by

$$\tau(\vec{v}) = \frac{\lambda}{\vec{v}} = \frac{1}{n\sigma(\vec{v})\vec{v}}. \tag{2-37}$$

The collision frequency $\nu$ is given by averaging over all possible velocities with the application of eq. (2-6), viz.

$$\nu = \left\langle \frac{1}{\tau(\vec{v})} \right\rangle = \frac{1}{n} \int n\sigma(\vec{v})\vec{v}\mathrm{d}^3\vec{v} = \int \sigma(\vec{v})\vec{v}\mathrm{d}^3\vec{v}. \tag{2-38}$$

A collision frequency can also be defined for species other than electrons, if necessary, by repeating the analysis made here but utilizing density and cross-sectional areas appropriate to the species being considered. In practice, this parameter can be measured from experimental data instead of calculated, and is responsible for a damping factor in electromagnetic waves propagating through a collisional plasma.

## 2.3
## Dielectric Description

Study of electromagnetic propagation through plasma has also been performed by treating the plasma as a dielectric medium with complex permittivity dependent on the plasma parameters, which is especially useful for applications in radio physics and technology. For the dielectric description, the Appleton-Hartree or Appleton-Lassen equation, formulated initially by German radio physicist H. K. Lassen gives the relative permittivity for electromagnetic wave propagation in a cold, isotropic, magnetized plasma as [21]

$$\epsilon_r = 1 - \frac{X}{1 - iZ - \frac{\frac{1}{2}Y^2\sin^2\theta}{1-X-iZ} \pm \frac{1}{1-X-iZ}\left(\frac{1}{4}Y^4\sin^4\theta + Y^2\cos^2\theta\,(1-X-iZ)^2\right)^{1/2}}, \tag{2-39}$$

where the terms are given by

$$X = \frac{\omega_p^2}{\omega^2}, \tag{2-40a}$$

$$Y = \frac{\omega_H}{\omega}, \tag{2-40b}$$

$$Z = \frac{\nu}{\omega}, \tag{2-40c}$$

$$\omega_p = 2\pi f_p = \sqrt{\frac{ne^2}{\epsilon_0 m}}, \tag{2-40d}$$

$$\omega_H = 2\pi f_H = \frac{B_0|e|}{m}, \tag{2-40e}$$

and where $\omega$ is the wave radial frequency, $\nu$ is the electron collision frequency, $n$ is the electron density, $B_0$ is the ambient magnetic field strength, $e$ is the electron charge, $m$ is the electron mass, and $\theta$ is the angle between the ambient magnetic field vector and the wave vector.

By making $B_0 = 0$, the electromagnetic wave propagation in a cold isotropic plasma with no background magnetic field can be characterized by the relative permittivity

$$\epsilon_r = 1 - \frac{\omega_p^2}{\omega^2 - i\omega\nu}. \tag{2-41}$$

Equating the previous result with the relative permittivity of an arbitrary lossy material,

$$\epsilon_r = \epsilon_r' - \frac{i\sigma}{\omega\epsilon_0}, \tag{2-42}$$

allows an effective conductivity $\sigma_{ef}$ to be found as

$$\sigma_{ef} = \frac{\epsilon_0 \omega_p^2}{\nu + i\omega}, \tag{2-43}$$

which gives rise to a plasma current density given by, in the frequency domain,

$$\vec{\tilde{J}}_p = \sigma_{ef} \vec{\tilde{E}}. \tag{2-44}$$

The propagation of electromagnetic waves through the dielectric plasma then must follow the following form of Maxwell's equations, expressed in the frequency domain,

$$\nabla \cdot \vec{\tilde{E}} = 0, \tag{2-45a}$$

$$\nabla \cdot \vec{\tilde{B}} = 0, \tag{2-45b}$$

$$\nabla \times \vec{\tilde{E}} = -i\omega\mu_0 \vec{\tilde{H}}, \tag{2-45c}$$

$$\nabla \times \vec{\tilde{H}} = \vec{J}_p + i\omega\epsilon_0 \vec{\tilde{E}}. \tag{2-45d}$$

Since the relative permittivity of the plasma depends on the plasma frequency $\omega_p$ and collision frequency $\nu$, which in the most general case can be functions of position, the plasma needs to be treated as a dispersive and inhomogeneous dielectric.

# 3
# Analytical Eigenfunction Method

The dielectric description presented in the previous chapter provides a simple way of studying the interaction between electromagnetic waves and plasma structures by restricting all of the complexities related to plasma phenomena into the dielectric constant and therefore allowing for usual techniques of solving electromagnetic problems to be employed. To explore that possibility, an analytical model based on eigenfunctions expansion is described in this chapter to study the expected field behaviour when an electromagnetic wave impinges on a dielectric cylinder. This chapter is based primarily on the ideas presented in [22–25].

Fields throughout this chapter are expressed in the frequency domain, with an harmonic dependence of $e^{i\omega t}$, but both the tilde notation and the exponential factor are suppressed throughout.

## 3.1
## Normal Plane Wave Incidence on an Homogeneous Infinite Cylinder

Consider a transverse magnetic to $z$ ($\mathrm{TM}_z$) plane wave travelling in the $+x$ direction through free space impinging on an infinite dielectric cylinder parallel to the $z$-axis and concentric with the origin of the $xy$-plane with radius $r$, as shown on figure 3.1.

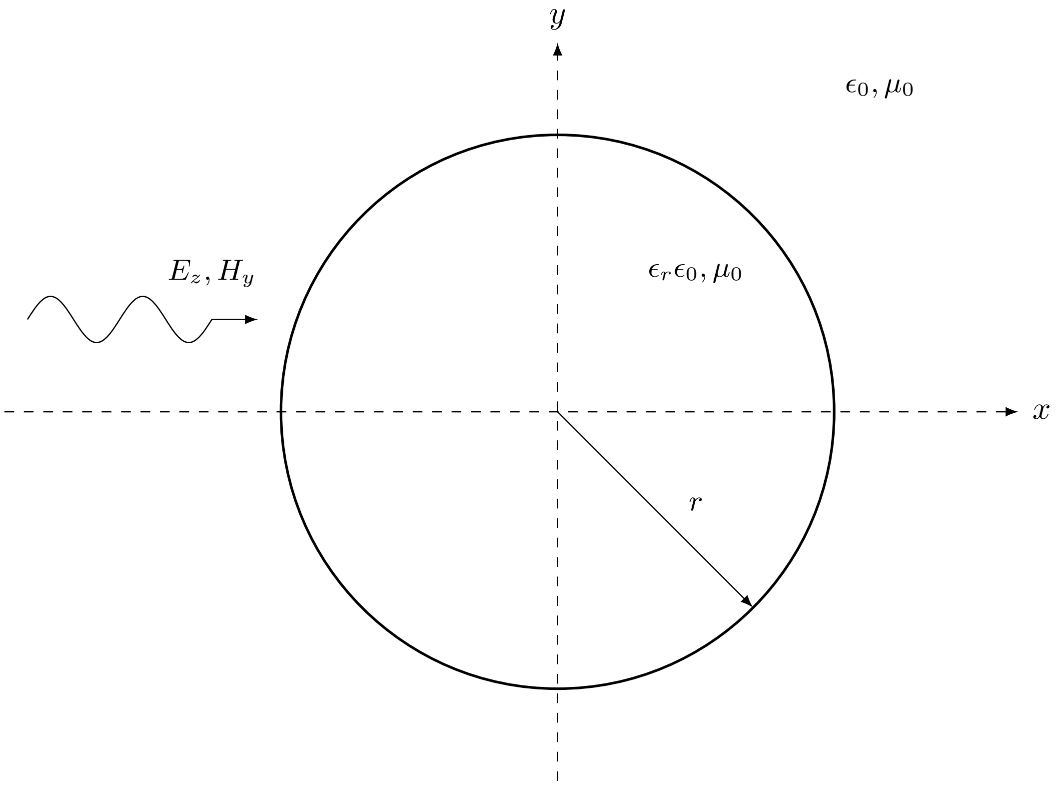

Figure 3.1: Plane wave incidence on the dielectric cylinder.

The electric and magnetic vector potentials related to this incident wave can be written as

$$\vec{F} = \vec{0} \qquad \text{and} \qquad \vec{A} = \psi_{in}\hat{z}, \tag{3-1}$$

where $\psi_{in}$ is the incident wave function given by

$$\psi_{in} = e^{-ik_0 x} = e^{-ik_0\rho\cos\phi}, \tag{3-2}$$

where $k_0 = \omega\sqrt{\epsilon_0\mu_0}$ is the wave number of free space.

Field components are obtained through

$$\vec{E} = -\frac{1}{\epsilon}\nabla \times \vec{F} + i\omega\vec{A} + \frac{i}{\omega\mu\epsilon}\nabla(\nabla\cdot\vec{A}), \tag{3-3a}$$

$$\vec{H} = \frac{1}{\mu}\nabla \times \vec{A} + i\omega\vec{F} + \frac{i}{\omega\mu\epsilon}\nabla(\nabla\cdot\vec{F}). \tag{3-3b}$$

This incident wave will impinge on the boundary with the infinite cylinder and suffer both reflection from and transmission into the cylinder. The fields outside the cylinder are now characterized by a new wave function $\psi_0$, whereas the fields within the cylinder are characterized by another wave function $\psi_1$.

All fields must satisfy the Helmholtz equation in cylindrical coordinates, which has Bessel functions and complex exponentials as its eigenfunctions (see Appendix A). The wave functions $\psi_0$ and $\psi_1$ can therefore be written as a linear combination of Bessel and exponential functions, viz.

$$\psi_0 = \sum_{n=-\infty}^{\infty} \left(a_n J_n(k_0\rho) + b_n H_n^{(2)}(k_0\rho)\right) e^{in\phi}, \tag{3-4a}$$

$$\psi_1 = \sum_{n=-\infty}^{\infty} \left(c_n J_n(k_1\rho) + d_n H_n^{(2)}(k_1\rho)\right) e^{in\phi}, \tag{3-4b}$$

where the unknown coefficients $a_n, b_n, c_n$ and $d_n$ must be found by application of boundary conditions. The choice of which Bessel functions to use in the expansion is arbitrary as long as they are linearly independent, so the Hankel function was chosen for its simple asymptotic form.

Since the origin of the coordinate system is within the domain of $\psi_1$, it is immediately found that $d_n = 0$ for all $n$ due to the pole at the origin present in the Hankel function. By expanding the incident wave function $\psi_{in}$ through a Fourier series in $\phi$, the incident wave function can be written

$$e^{-ik_0\rho\cos\phi} = \sum_{n=-\infty}^{\infty} J_n(k_0\rho)e^{in\phi}, \tag{3-5}$$

so it is also immediately found that $a_n = 1$ for all $n$, justifying the previous choice of wave function. The remaining coefficients may be found by application of the continuity conditions for tangential fields at the boundary, i.e.

$$E_z^0|_{\rho=r} = E_z^1|_{\rho=r} \qquad \text{and} \qquad H_\phi^0|_{\rho=r} = H_\phi^1|_{\rho=r}, \tag{3-6}$$

which leads to the solution

$$\begin{bmatrix} c_n \\ b_n \end{bmatrix} = \begin{bmatrix} J_n(k_1r) & H_n^{(2)}(k_0r) \\ k_1 J_n'(k_1r) & -k_0 H_n'^{(2)}(k_0r) \end{bmatrix}^{-1} \begin{bmatrix} J_n(k_0r) \\ k_0 J_n'(k_0r) \end{bmatrix}, \tag{3-7}$$

where $J_n'$ and $H_n'^{(2)}$ denote the derivatives of the Bessel and Hankel functions, respectively, and $\epsilon_r$ is the relative permittivity of the dielectric cylinder. With the set of coefficients found, the electromagnetic fields at all points in space are fully characterized, viz.

$$E_z^0 = i\omega \sum_{n=-\infty}^{\infty} i^{-n} \left( J_n(k_0\rho) + b_n H_n^{(2)}(k_0\rho) \right) e^{in\phi}, \tag{3-8a}$$

$$H_\phi^0 = \frac{1}{\mu_0} \sum_{n=-\infty}^{\infty} i^{-n} \left( k_0 J_n'(k_0\rho) + b_n k_0 H_n'^{(2)}(k_0\rho) \right) e^{in\phi}, \tag{3-8b}$$

$$H_\rho^0 = \frac{1}{\mu_0}\frac{1}{\rho} \sum_{n=-\infty}^{\infty} n i^{-n} \left( J_n(k_0\rho) + b_n H_n^{(2)}(k_0\rho) \right) e^{in\phi}, \tag{3-8c}$$

outside the cylinder and

$$E_z^1 = i\omega \sum_{n=-\infty}^{\infty} i^{-n} c_n J_n(k_1\rho) e^{in\phi}, \tag{3-9a}$$

$$H_\phi^1 = \frac{1}{\mu_0} \sum_{n=-\infty}^{\infty} i^{-n} c_n k_1 J_n'(k_1\rho) e^{in\phi}, \tag{3-9b}$$

$$H_\rho^1 = \frac{1}{\mu_0}\frac{1}{\rho} \sum_{n=-\infty}^{\infty} n i^{-n} c_n J_n(k_1\rho) e^{in\phi}, \tag{3-9c}$$

inside the cylinder.

Due to the two-dimensional nature of the problem, the radiated (or scattered) electric field far from the dielectric cylinder ($k_0\rho \gg r$) propagates as a cylindrical wave (see Appendix B),

$$E_z^s = A(\phi) \frac{e^{-ik_0\rho}}{\sqrt{\rho}}, \tag{3-10}$$

where $A(\phi)$ is the scattering amplitude. Taking the asymptotic expansion of the field present in free-space and ignoring the Bessel term related to the incident field,

$$E_z^s = \sum_{n=-\infty}^{\infty} \sqrt{\frac{2}{\pi k_0 \rho}} b_n e^{-i(k_0\rho - \frac{n\pi}{2} - \frac{\pi}{4})} e^{in\phi}. \tag{3-11}$$

By equating the two expressions, the scattering amplitude is found to be

$$A(\phi) = \sqrt{\frac{2}{\pi k_0}} e^{i\frac{\pi}{4}} \sum_{n=-\infty}^{\infty} b_n e^{in(\phi + \frac{\pi}{2})}. \tag{3-12}$$

## 3.2
## Normal Plane Wave Incidence on an Inhomogeneous Infinite Cylinder

Consider now an infinite dielectric similar to the one studied in the previous section, but with an inhomogeneous relative permittivity described by a radial function $\epsilon_r(\rho)$. Directly solving the field equations for an inhomogeneous medium is not a simple matter, so the strategy employed is to treat the inhomogeneous cylinder as a series of homogeneous concentric cylindrical shells with constant permittivity chosen so that the overall variation inside the cylinder approximates the inhomogeneous profile.

Analysis of the homogeneous shells follows the same overall idea described in the previous section, with fields within each shell being expanded into an infinite series of Bessel and complex exponential functions with coefficients to be determined by application of boundary conditions.

The method is illustrated by an arbitrary example on figure 3.2. It is clear that the quality of this approximation depends on the number of homogeneous shells used; the error in the staircase approximation of the inhomogeneous permittivity must be small for the results to be valid.

Suppose that the inhomogeneous cylinder has been divided into $p$ shells. The wave function in free space $\psi_0$ is given by equation (3-4a), repeated here for convenience,

$$\psi_0 = \sum_{n=-\infty}^{\infty} \left(a_n J_n(k_0\rho) + b_n H_n^{(2)}(k_0\rho)\right) e^{in\phi}, \tag{3-4a}$$

and the wave-function within the $m^{\text{th}}$ shell can be written as

$$\psi_m = \sum_{n=-\infty}^{\infty} \left(c_{nm} J_n(k_m\rho) + d_{nm} H_n^{(2)}(k_m\rho)\right) e^{in\phi}, \tag{3-13}$$

where $a_n, b_n, c_{nm}$ and $d_{nm}$ are coefficients to be determined by application of boundary conditions.

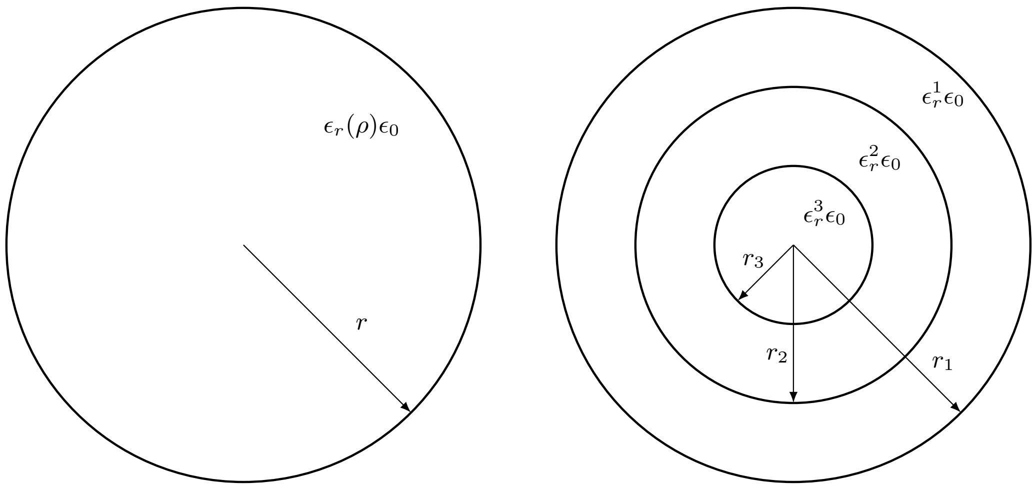

3.2(a): Inhomogeneous cylinder with radially-dependent permittivity.

3.2(b): Approximation of the inhomogeneous cylinder as a series of homogeneous shells. The outer radius is equal to the original inhomogeneous cylinder's radius, $r_1 = r$.

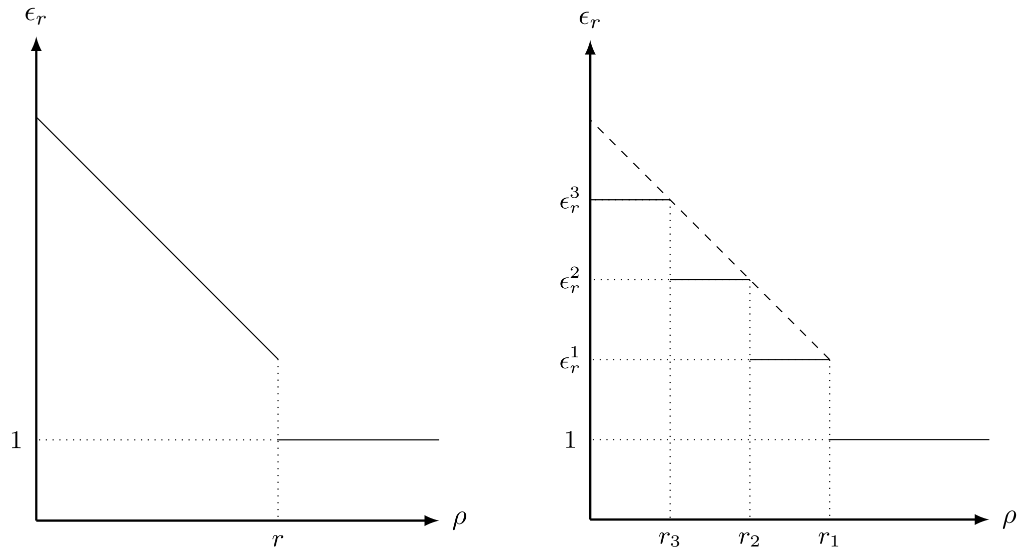

3.2(c): Arbitrary linear permittivity profile for the inhomogeneous cylinder.

3.2(d): Permittivity profile for the homogeneus shell approximation. The outer radius is equal to the original inhomogeneous cylinder's radius, $r_1 = r$.

Figure 3.2: Illustrative example of the approximation of an arbitrary inhomogeneous cylinder with a linear permittivity profile by a series of homogeneous shells.

Application of the continuity condition for tangential fields, eq. (3-6), at the boundary between free space and the first layer yields the system of equations

$$\begin{bmatrix} J_n(k_1r_1) & H_n^{(2)}(k_1r_1) \\ k_1J_n'(k_1r_1) & k_1H_n'^{(2)}(k_1r_1) \end{bmatrix} \begin{bmatrix} c_{n1} \\ d_{n1} \end{bmatrix} = \begin{bmatrix} J_n(k_0r_1) & H_n^{(2)}(k_0r_1) \\ k_0J_n'(k_0r_1) & k_0H_n'^{(2)}(k_0r_1) \end{bmatrix} \begin{bmatrix} a_n \\ b_n \end{bmatrix}, \tag{3-14}$$

which can be rearranged into

$$\begin{bmatrix} c_{n1} \\ d_{n1} \end{bmatrix} = T_1 \begin{bmatrix} a_n \\ b_n \end{bmatrix}, \tag{3-15}$$

where

$$T_1 = \begin{bmatrix} J_n(k_1r_1) & H_n^{(2)}(k_1r_1) \\ k_1J_n'(k_1r_1) & k_1H_n'^{(2)}(k_1r_1) \end{bmatrix}^{-1} \begin{bmatrix} J_n(k_0r_1) & H_n^{(2)}(k_0r_1) \\ k_0J_n'(k_0r_1) & k_0H_n'^{(2)}(k_0r_1) \end{bmatrix} \tag{3-16}$$

is the transmission matrix for the first shell, and its dependency on each mode $n$ was left implicit.

Application of the continuity condition at the $m^{\text{th}}$ shell, $1 < m \leq p$, yields

$$\begin{bmatrix} c_{nm} \\ d_{nm} \end{bmatrix} = T_m \begin{bmatrix} c_{nm-1} \\ d_{nm-1} \end{bmatrix}, \tag{3-17}$$

where

$$\begin{aligned} T_m = & \begin{bmatrix} J_n(k_mr_m) & H_n^{(2)}(k_mr_m) \\ k_mJ_n'(k_mr_m) & k_mH_n'^{(2)}(k_mr_m) \end{bmatrix}^{-1} \times \\ & \times \begin{bmatrix} J_n(k_{m-1}r_m) & H_n^{(2)}(k_{m-1}r_m) \\ k_{m-1}J_n'(k_{m-1}r_m) & k_{m-1}H_n'^{(2)}(k_{m-1}r_m) \end{bmatrix} \end{aligned} \tag{3-18}$$

is the transmission matrix for the $m^{\text{th}}$ shell.

Now the coefficients for the $p^{\text{th}}$ shell can be written

$$\begin{bmatrix} c_{np} \\ d_{np} \end{bmatrix} = T_g \begin{bmatrix} a_n \\ b_n \end{bmatrix}, \tag{3-19}$$

where $T_g = T_p \times ... \times T_1$ is the global transmission matrix from free space to the innermost shell. Additionally, as before, $a_n = 1$ due to the incident wave under consideration and $d_{np} = 0$ due to the Hankel's function pole located at the origin. Equation (3-19) can be solved for $b_n$, yielding

$$b_n = -\frac{T_{g_{2,1}}}{T_{g_{2,2}}}, \tag{3-20}$$

where $T_{g_{i,j}}$ denotes the matrix element of the global transmission matrix at the $i^{\text{th}}$ row and $j^{\text{th}}$ column.

With $b_n$ known, the scattering amplitude due to the inhomogeneous cylinder can be found. As before, by taking the asymptotic expression for the Hankel function and equating it with a cylindrical propagating wave, equation (3-12) is recovered, repeated here for convenience

$$A(\phi) = \sqrt{\frac{2}{\pi k_0}} e^{i\frac{\pi}{4}} \sum_{n=-\infty}^{\infty} b_n e^{in(\phi+\frac{\pi}{2})}. \tag{3-12}$$

With both $a_n$ and $b_n$ known, equation (3-15) can be applied to find $c_{n1}$ and $d_{n1}$. The process can then be repeated by means of equation (3-18), i.e., by applying the $m^{\text{th}}$ transmission matrix to the $(m-1)^{\text{th}}$ known coefficients until all field coefficients are found. The field components within the cylinder, for each shell, are then given by

$$E_z^m = i\omega \sum_{n=-\infty}^{\infty} i^{-n} \left( c_{nm} J_n(k_m\rho) + d_{nm} H_n^{(2)}(k_m\rho) \right) e^{in\phi}, \tag{3-21a}$$

$$H_\phi^m = \frac{1}{\mu_0} \sum_{n=-\infty}^{\infty} i^{-n} \left( c_{nm} k_m J_n'(k_m\rho) + d_{nm} k_m H_n'^{(2)}(k_m\rho) \right) e^{in\phi}, \tag{3-21b}$$

$$H_\rho^m = \frac{1}{\mu_0}\frac{1}{\rho} \sum_{n=-\infty}^{\infty} n i^{-n} \left( c_{nm} J_n(k_m\rho) + d_{nm} H_n^{(2)}(k_m\rho) \right) e^{in\phi}, \tag{3-21c}$$

whereas the field components in free space are again given by equation (3-8), repeated here for convenience.

$$E_z^0 = i\omega \sum_{n=-\infty}^{\infty} i^{-n} \left( J_n(k_0\rho) + b_n H_n^{(2)}(k_0\rho) \right) e^{in\phi}, \tag{3-8a}$$

$$H_\phi^0 = \frac{1}{\mu_0} \sum_{n=-\infty}^{\infty} i^{-n} \left( k_0 J_n'(k_0\rho) + b_n k_0 H_n'^{(2)}(k_0\rho) \right) e^{in\phi}, \tag{3-8b}$$

$$H_\rho^0 = \frac{1}{\mu_0}\frac{1}{\rho} \sum_{n=-\infty}^{\infty} n i^{-n} \left( J_n(k_0\rho) + b_n H_n^{(2)}(k_0\rho) \right) e^{in\phi}. \tag{3-8c}$$

# 4
# FDTD Simulation

Numerical simulations are an important tool in understanding physical phenomena as well as designing devices for use in technological applications. Due to the complexity of the theory of plasmas for structures of interest, simulations are particularly useful in understanding the characteristics and the effects of plasma interactions on electromagnetic waves.

Much interest has been shown in the simulation of plasmas through Particle-in-Cell (PIC) codes, where specific “macroparticles” are tracked through the computational domain and their behaviour simulated, including some recent breakthroughs [26, 27], or through Eulerian solvers for the density function, where it is discretized over grid points in the computational domain and numerically solved [28, 29]. For this work the finite-difference time-domain (FDTD) method of simulation was chosen, with the plasma characteristics being added to usual electromagnetic algorithms.

The FDTD method consists, at its most basic, of simulating the local behaviour of fields at nodes present in a a discretized version of the region or structure under consideration [30, 31]. To that end, Maxwell’s equations are solved numerically for all field components at each node in a self-consistent scheme that allows the electromagnetic solution for the problem at hand to be explicitly calculated in the time domain.

## 4.1
## The Finite-Differences Approximation

Consider a scalar one-dimensional differential equation of the form

$$\frac{\partial}{\partial t} y(t,x) = f(x), \qquad \text{with} \qquad y(0,x) = y_0(x). \tag{4-1}$$

The finite-differences method consists of approximating derivatives by finite differences as a means of discretizing the equation of interest [32]. Using a forward difference around the point $t$, equation (4-1) can be written

$$\frac{y(t+\Delta_t,x) - y(t,x)}{\Delta_t} = f(x) \tag{4-2}$$

or, rearranging terms,

$$y(t+\Delta_t, x) = y(t, x) + \Delta_t f(x). \tag{4-3}$$

By setting the initial condition $y(0, x) = y_0(x)$, where $y_0(x)$ is a known function, and assuming the values of both $y(t, x)$ and $f(x)$ can be sampled at points $x = i\Delta_x$, $i \in \mathbb{N}$ without loss of information, equation (4-3) provides an explicit time-marching procedure for calculating the numerical solution of equation (4-1) at all points $t = q\Delta_t$, $q \in \mathbb{N}$ that can be readily implemented in a computer system.

To quantify the quality of this approximation, one must analyse the magnitude of the error between the finite difference and the actual function derivative. This can be performed through a Taylor expansion for $y(t+\Delta_t, x)$,

$$y(t+\Delta_t, x) = y(t, x) + \Delta_t \frac{\partial}{\partial t} y(t, x) + \mathcal{O}(\Delta_t^2), \tag{4-4}$$

such that dividing through by $\Delta_t$ and rearranging terms gives

$$\frac{y(t+\Delta_t, x) - y(t, x)}{\Delta_t} - \frac{\partial}{\partial t} y(t, x) = \mathcal{O}(\Delta_t), \tag{4-5}$$

thus the discretization time-step $\Delta_t$ must be small in some sense to ensure a good approximation.

Consider now the set of equations

$$\frac{\partial}{\partial t} f(t, x) = \frac{\partial}{\partial x} g(t, x) \qquad \text{and} \qquad \frac{\partial}{\partial t} g(t, x) = \frac{\partial}{\partial x} f(t, x), \tag{4-6}$$

with initial conditions

$$f(0, x) = f_0(x) \qquad \text{and} \qquad g(0, x) = g_0(x). \tag{4-7}$$

Forward differences could be used again to discretize this set of equations as done previously. However, an alternative is to use central differences instead, i.e.

$$\frac{f(t+\frac{\Delta_t}{2}, x) - f(t-\frac{\Delta_t}{2}, x)}{\Delta_t} = \frac{g(t, x+\frac{\Delta_t}{2}) - g(t, x-\frac{\Delta_t}{2})}{\Delta_x}, \tag{4-8a}$$

$$\frac{g(t+\frac{\Delta_t}{2}, x) - g(t-\frac{\Delta_t}{2}, x)}{\Delta_t} = \frac{f(t, x+\frac{\Delta_t}{2}) - f(t, x-\frac{\Delta_t}{2})}{\Delta_x}, \tag{4-8b}$$

or, rearranging terms,

$$f(t+\frac{\Delta_t}{2},x) = f(t-\frac{\Delta_t}{2},x) + \frac{\Delta_t}{\Delta_x}\left(g(t,x+\frac{\Delta_t}{2}) - g(t,x-\frac{\Delta_t}{2})\right), \tag{4-9a}$$

$$g(t+\frac{\Delta_t}{2},x) = g(t-\frac{\Delta_t}{2},x) + \frac{\Delta_t}{\Delta_x}\left(f(t,x+\frac{\Delta_t}{2}) - f(t,x-\frac{\Delta_t}{2})\right). \tag{4-9b}$$

Setting the initial conditions $f_0(x)$ and $g_0(x)$ at time $t = 0$ once more allows for the algorithm to explicitly compute the numerical solution, provided appropriate discretizations $\Delta_t$ and $\Delta_x$ are chosen. The advantage of using central instead of forward differences is that the error for the derivative approximation is now given by e.g. for the time derivative,

$$\left|\frac{\partial}{\partial t}f(t,x) - \frac{f(t+\frac{\Delta_t}{2},x) - f(t-\frac{\Delta_t}{2},x)}{\Delta_t}\right| = \mathcal{O}(\Delta_t^2), \tag{4-10}$$

which leads to a better approximation for the same step size. The apparent cost is in the complexity of discretization, as functions must now be stored for integer and half-integer values of the discretized variables. However, the computational domain discussed in the next section resolves that complexity.

## 4.2
## Computational Domain

The problem of interest is two-dimensional, and propagation of modes transverse-magnetic to $z$ (TM$_z$) are considered, that is, magnetic fields are restricted to $\vec{H} = H_x\hat{x} + H_y\hat{y}$ and electric fields are given by $\vec{E} = E_z\hat{z}$.

The basic scheme laid out by Yee [33] in his seminal paper is used to create the computational domain. Assuming the time step is given by $\Delta_t$ and the spatial steps are given by $\Delta_s = \Delta_x = \Delta_y$, a function $f$ of space and time evaluated at a discrete point in space-time $(n\Delta_t, i\Delta_x, j\Delta_y)$, where $n, i, j$ are integers or half-integers, is denoted as

$$f(n\Delta_t, i\Delta_x, j\Delta_y) = f^n(i,j). \tag{4-11}$$

A necessary condition for the convergence of solutions obtained explicitly by the FDTD method is the Courant–Friedrichs–Lewy condition [34], which can be stated, for two-dimensional problems, as

$$\frac{\Delta_t}{\Delta_s} \leq \frac{1}{\sqrt{2}c}, \tag{4-12}$$

where $c$ is the speed of light.

Electromagnetic fields are spatially discretized over a finite Cartesian grid as per figure 4.1. Of note is that electric and magnetic fields are shifted by half-steps from each other both spatially and in time, that is, electric fields are stored at integer times and positions, while magnetic fields are stored at half-integer times and positions. This allows for Maxwell's equations to be readily discretized as per equation (4-9), becoming

$$H_x^{n+\frac{1}{2}}(i,j+\frac{1}{2}) = H_x^{n-\frac{1}{2}}(i,j+\frac{1}{2}) - \frac{\mu_0\Delta_t}{\Delta_s}\left(E_z^n(i,j+1) - E_z^n(i,j)\right), \tag{4-13a}$$

$$H_y^{n+\frac{1}{2}}(i+\frac{1}{2},j) = H_y^{n-\frac{1}{2}}(i+\frac{1}{2},j) - \frac{\mu_0\Delta_t}{\Delta_s}\left(E_z^n(i+1,j) - E_z^n(i,j)\right), \tag{4-13b}$$

$$\begin{aligned} E_z^{n+1}(i,j) = {} & E_z^n(i,j) + \frac{\Delta_t}{\epsilon_0\Delta_s}\Bigg(H_y^{n+\frac{1}{2}}(i+\frac{1}{2},j) - H_y^{n+\frac{1}{2}}(i-\frac{1}{2},j) - \\ & H_x^{n+\frac{1}{2}}(i,j+\frac{1}{2}) - H_x^{n+\frac{1}{2}}(i,j-\frac{1}{2})\Bigg), \end{aligned} \tag{4-13c}$$

which can be used to propagate electromagnetic waves through discretized free space within the computational domain.

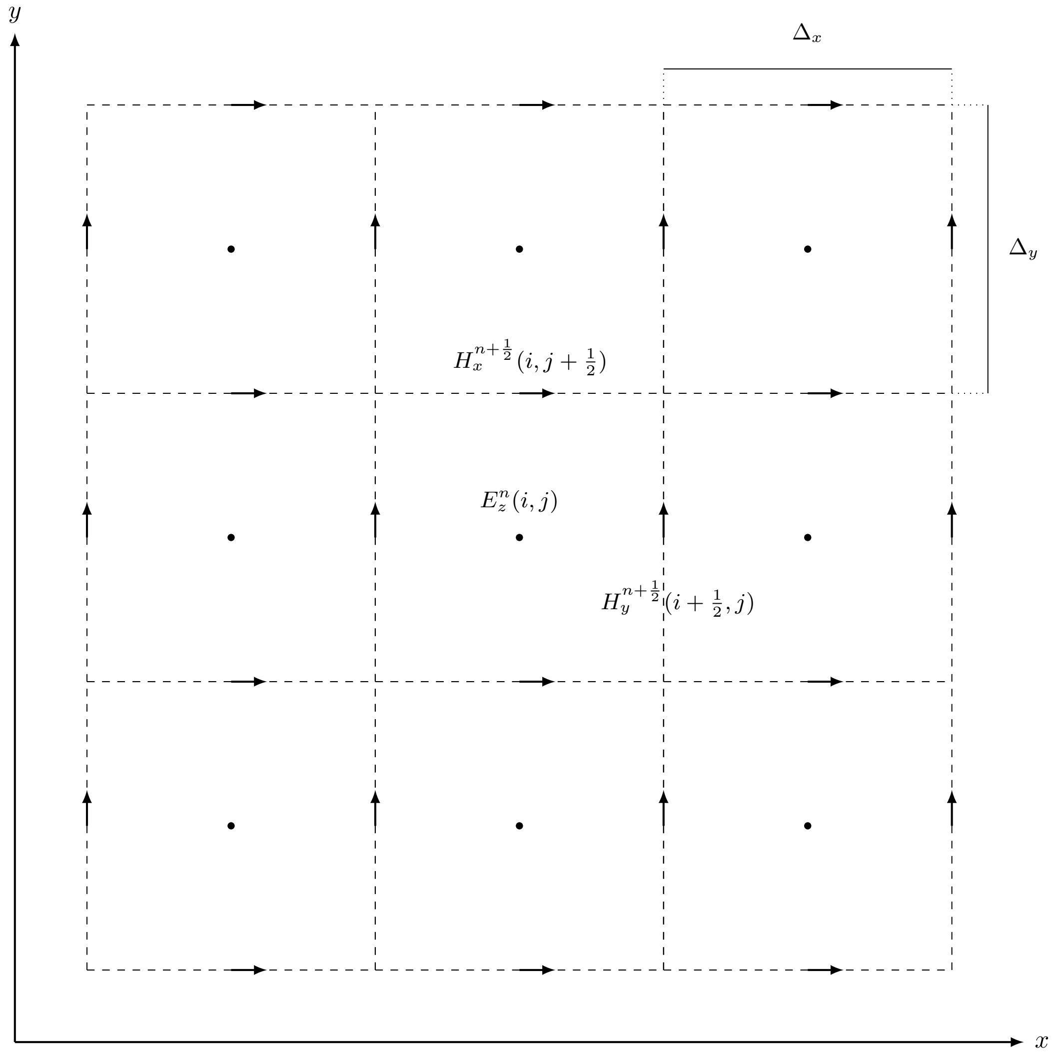

Figure 4.1: Generic cartesian spatial cell $(i, j)$ and surrounding cells in the 2D computational domain. Stored values for each cell are the $z$-component of the electric field at time $n$ and position $(i, j)$, the $x$-component of the magnetic field at time $n+\frac{1}{2}$ and position $(i, j+\frac{1}{2})$ and the $y$-component of the magnetic field at time $n+\frac{1}{2}$ and position $(i+\frac{1}{2}, j)$.

## 4.3
## Plasma Propagation

The update equations for the electromagnetic wave propagating within the plasma must be derived from equations (2-45c) and (2-45d) instead of the usual Maxwell's equation, repeated here for convenience:

$$\nabla \times \vec{E} = -\mu_0 \frac{\partial \vec{H}}{\partial t}, \tag{2-45c}$$

$$\nabla \times \vec{H} = \vec{J_p} + \epsilon_0 \frac{\partial \vec{E}}{\partial t}. \tag{2-45d}$$

The only difference from the usual Maxwell equations used in the previous section is the appearance of the plasma current term given by, in the frequency domain, $\vec{\tilde{J}_p} = \sigma_{ef}\vec{\tilde{E}} = \frac{\epsilon_0 \omega_p^2}{\nu + i\omega}\vec{\tilde{E}}$. This term can be efficiently handled by means of an Auxiliary Differential Equation (ADE) formulation as follows. Considering only the $\tilde{J}_z$ component due to the nature of the problem at hand and multiplying throughout by $\nu + i\omega$,

$$i\omega \tilde{J}_z = \epsilon_0 \omega_p^2 \tilde{E}_z - \nu \tilde{J}_z. \tag{4-15}$$

Taking the inverse Fourier transform, the time-domain version of equation (4-15) is given by

$$\frac{\partial J_z}{\partial t} = \epsilon_0 \omega_p^2 E_z - \nu J_z, \tag{4-16}$$

which can be readily discretized using finite differences to yield

$$\begin{aligned} \left(\frac{J_z^{n+1}(i,j) - J_z^n(i,j)}{\Delta_t}\right) =& \epsilon_0 \Big(\omega_p(i,j)\Big)^2 \left(\frac{E_z^{n+1}(i,j) + E_z^n(i,j)}{2}\right) \\ & - \nu(i,j) \left(\frac{J_z^{n+1}(i,j) + J_z^n(i,j)}{2}\right), \end{aligned} \tag{4-17}$$

where the time-averages on the right-hand side were taken so that the discrete time-step was in accordance with the central difference approximation used on the left-hand side.

Equation (4-17) can be solved for $J_z^{n+1}(i,j)$ to yield

$$J_z^{n+1}(i,j) = \kappa_p(i,j) J_z^n(i,j) + \beta_p(i,j) \left(E_z^{n+1}(i,j) + E_z^n(i,j)\right), \tag{4-18}$$

where

$$\kappa_p(i,j) = \frac{1 - \nu(i,j)\frac{\Delta_t}{2}}{1 + \nu(i,j)\frac{\Delta_t}{2}} \qquad \text{and} \qquad \beta_p(i,j) = \frac{\Big(\omega_p(i,j)\Big)^2 \epsilon_0 \frac{\Delta_t}{2}}{1 + \nu(i,j)\frac{\Delta_t}{2}}. \tag{4-19}$$

The update equations for the magnetic field components remain unchanged, but the update equation for the electric field requires knowledge of the plasma current at time-step $n + \frac{1}{2}$. This is again obtained by a simple time average such that the final update equation for the electric field is given by

$$\begin{aligned} E_z^{n+1}(i,j) = &\left(\frac{2\epsilon_0 - \Delta_t \beta_p(i,j)}{2\epsilon_0 + \Delta_t \beta_p(i,j)}\right) E_z^n(i,j) + \left(\frac{2\Delta_t}{2\epsilon_0 + \Delta_t \beta_p(i,j)}\right) \times \\ &\times \left(\nabla \times \vec{H}^{n+\frac{1}{2}} - \frac{1+\kappa_p(i,j)}{2} J_z^n(i,j)\right), \end{aligned} \tag{4-20}$$

where

$$\begin{aligned} \nabla \times \vec{H}^{n+\frac{1}{2}} = &\Big( H_y^{n+\frac{1}{2}}(i+\frac{1}{2},j) - H_y^{n+\frac{1}{2}}(i-\frac{1}{2},j) - \\ &H_x^{n+\frac{1}{2}}(i,j+\frac{1}{2}) - H_x^{n+\frac{1}{2}}(i,j-\frac{1}{2})\Big). \end{aligned} \tag{4-21}$$

## 4.4
## Grid Termination

The problem under investigation includes fields that must radiate to infinity. The computational domain, however, is necessarily finite. Therefore, some way of terminating the computational grid must be employed that maintains the radiation condition at infinity for the fields, like absorbing boundary conditions (ABCs) or perfectly-matched layers (PMLs). Due to their ease of implementation and great efficiency in two dimensions, ABCs based on one-way wave-equations were chosen.

Consider a node the edge of the computational domain, e.g. at the rightmost boundary. Fields at this node must be allowed to propagate outwards towards infinity, in the positive $x$ direction, without back-reflections into the computational domain. This can be illustrated through analysis of the one-dimensional scalar wave equation, i.e.,

$$\left(\frac{\partial^2}{\partial t^2} - c^2 \frac{\partial^2}{\partial x^2}\right)\psi = 0, \tag{4-22}$$

where the one-dimensional wave operator can be decomposed into

$$\left(\frac{\partial}{\partial t} + c\frac{\partial}{\partial x}\right)\left(\frac{\partial}{\partial t} - c\frac{\partial}{\partial x}\right)\psi = 0. \tag{4-23}$$

The wave equation (4-22) admits solutions of the form

$$\psi = F(x - ct) + G(x + ct), \tag{4-24}$$

where $F$ is an arbitrary wave propagating in the positive $x$ direction and $G$ is an arbitrary wave propagating in the negative $x$ direction. The advection equation

$$\left(\frac{\partial}{\partial t} \pm c\frac{\partial}{\partial x}\right)\psi = 0, \tag{4-25}$$

on the other hand, admits solutions of the form $\psi(x \pm ct)$ of a single wave propagating in either direction, depending on the sign used in the advection equation, but not both. Engquist and Majda [35] formally showed that the advection equation (or equivalent one-way wave equations) can be used as analytical absorbing boundary conditions at the edge of the computational domain.

Expanding a central-differences approximation at a node on the edge of the computational domain yields an update equation that depends on the values of the node being updated and two interior nodes for the current and previous times-steps. For example, for the left edge of the computational domain, $x = 0$, the update equation for the second-order ABC is given by

$$\begin{aligned} E_z^{n+1}(0,j) =& \frac{-1}{S+2+\frac{1}{S}}\left[S-2+\frac{1}{S}\left(E_z^{n+1}(2,j)+E_z^{n-1}(0,j)\right)+\right. \\ &+2(S-\frac{1}{S})\left(E_z^{n}(0,j)+E_z^{n}(2,j)-E_z^{n+1}(1,j)-E_z^{n-1}(1,j)\right) \\ &\left.-4(S+\frac{1}{S})E_z^{n}(1,j)\right]-E_z^{n-1}(2,j) \end{aligned} \tag{4-26}$$

where

$$S = \frac{\Delta_t}{\sqrt{\mu_0\epsilon_0}\Delta_s}. \tag{4-27}$$

The ABC update equations for the other edges are similar, but with the appropriate positions (for the right edge, e.g., $N_x$, $N_x - 1$ and $N_x - 2$ instead of 0, 1 and 2, respectively).

It is worth noting that this second-order ABC update equation was derived from the one-dimensional advection equation and applied to a two-dimensional problem, but the results observed for the magnitude of numerical reflections are well bellow 1% of the fields incident on the computational boundary.

## 4.5
## Steady-State Fields

For a given electromagnetic problem, it is useful to know the steady-state field solution, in the frequency domain, due to plane wave excitation.

That information can be used to construct solutions to arbitrary excitations and is also at times easier to analyse. The FDTD method provides a time-domain solution, however a Fourier Transform can be employed to find any field component $f$ in the frequency domain,

$$\tilde{f}(\omega) = \int_{-\infty}^{\infty} f(t) e^{-i\omega t} \mathrm{d}t = \int_{0}^{N_t \Delta_t} f(t) e^{-i\omega t} \mathrm{d}t, \tag{4-28}$$

which can be readily implemented concurrently to the leap-frogging algorithm at all grid points by means of

$$\begin{aligned} \tilde{f}(i,j,\omega) \approx \frac{1}{3} \Bigg( & f^0(i,j) + 2 \sum_{n \text{ even}} f^n(i,j) e^{-i\omega n \Delta_t} + \\ & + 4 \sum_{n \text{ odd}} f^n(i,j) e^{-i\omega n \Delta_t} + f^{N_t}(i,j) e^{-i\omega N_t \Delta_t} \Bigg), \end{aligned} \tag{4-29}$$

where Simpson's rule was employed to numerically evaluate the Fourier integral [36] (see Appendix C). Of note is that, in practice, the method implemented to calculate $\tilde{f}(i,j,\omega)$ consists simply of creating an accumulating variable and, at each time-step, adding the appropriate value prescribed by Simpson's rule to the accumulator.

Due to the linearity of the problem at hand, each frequency-domain field component calculated by means of equation (4-29) can be written as

$$Y(\omega) = H(\omega) X(\omega), \tag{4-30}$$

where $H(\omega)$ is the transfer function that relates an arbitrary frequency-domain excitation $X(\omega)$ to its associated frequency response $Y(\omega)$ [37]. In other words, $H(\omega)$ is the frequency response of the structure to an incident harmonic wave of frequency $\omega$ up to a phase factor (see Appendix D). It can be obtained by dividing the resulting frequency-domain fields by the incident pulse utilized in the FDTD, transformed to the frequency domain also by application of equation (4-29), i.e.,

$$H(i,j,\omega) = \frac{Y(i,j,\omega)}{X(i,j,\omega)} = \frac{\tilde{E}(i,j,\omega)}{\tilde{E}_{in}(i,j,\omega)}. \tag{4-31}$$

This process is illustrated with a block diagram in figure 4.2.

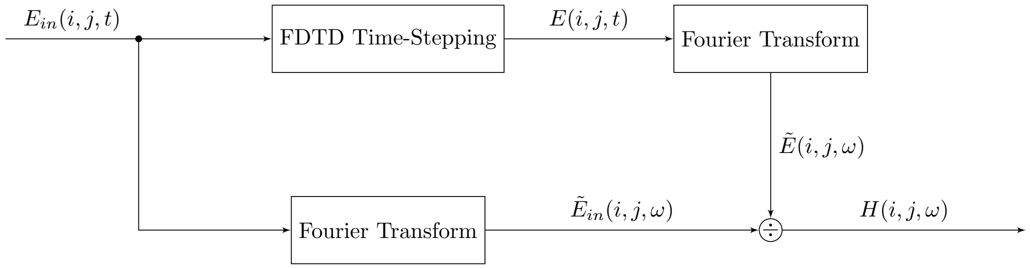

Figure 4.2: Block diagram showing the process for obtaining the frequency response of the structure from the time-domain result given by the FDTD algorithm. The Fourier Transforms are performed according to equation (4-29).

## 4.6
## Total-Field Scattered-Field Technique

To obtain the fields scattered by the structure of interest, a Total-Field Scattered-Field (TFSF) boundary is implemented. The TFSF technique consists of taking advantage of the linearity of Maxwell's equations to write

$$\vec{E}_{tot} = \vec{E}_{inc} + \vec{E}_{scat} \qquad \text{and} \qquad \vec{H}_{tot} = \vec{H}_{inc} + \vec{H}_{scat}, \tag{4-32}$$

where $\vec{E}_{inc}$ and $\vec{H}_{inc}$ are the incident fields assumed to be known at all points of the computational grid at all time steps, and $\vec{E}_{scat}$ and $\vec{H}_{scat}$ are the scattered fields due to the presence of the scattering structure.

The TFSF technique consists of separating the computational domain in two distinct regions, as shown on figure 4.3(a). In region 1, total field components are stored and operated upon by the update equations. In region 2, only the scattered field components are stored and updated, and an ABC is implemented as described on section 4.4. The update equations for field components near the boundary, shown in more detail in figure 4.3(b), are responsible for subtracting the incident known fields and allowing only the scattered field components to propagate into region 2.

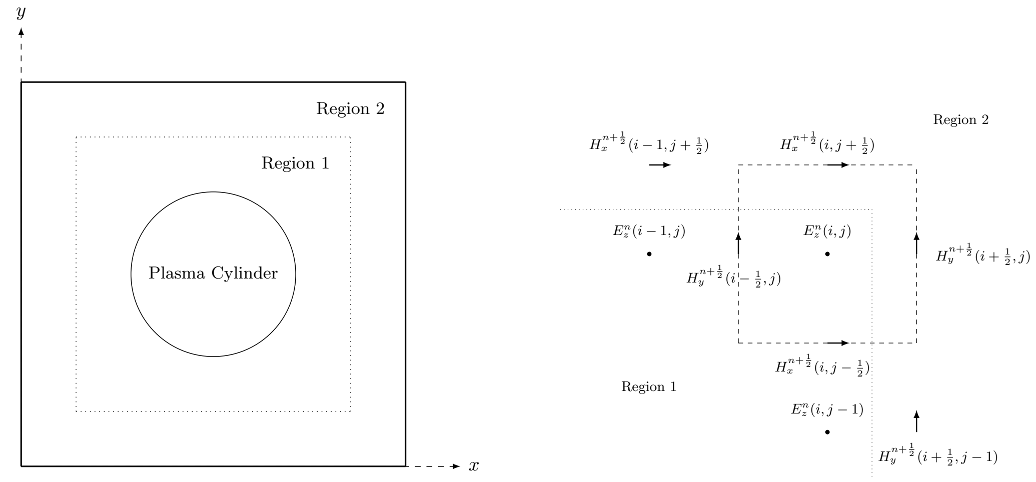

4.3(a): Region separation for the TFSF technique. Region 1 consists of total fields while region 2 consists only of scattered fields.

4.3(b): Detailed view of the field components adjacent to the TFSF boundary. A computational cell at the corner of the TFSF boundary is shown.

Figure 4.3: Total-Field Scattered-Field technique.

The strategy for implementing the TFSF boundary consists of concurrently running an auxiliary one-dimensional FDTD simulation to account for the propagation of the incident field, which can then be subtracted appropriately across the TSFS boundary to let only the scattered fields propagate into region 2. It is worth noting that this solution is only possible if the incident wave propagates along one of the coordinate axes; for the problem under consideration, however, that requirement is irrelevant because the structure can always be rotated so that the incident wave propagates along e.g. the $x$-axis.

The algorithm for updating the fields and applying the TFSF boundary at each time step is thus given by the following procedure:

1. Update the magnetic field components in the 2D grid;
2. Correct the magnetic field components adjacent to the TFSF boundary utilizing the electric field value from the same position in the 1D grid;
3. Update the field components in the 1D grid;
4. Correct the electric field component adjacent to the TFSF boundary utilizing the magnetic field value from the same position in the 1D grid;
5. Update the electric field component in the 2D grid.

This implementation has the added benefit of simplifying the initialization of the impinging plane wave. By directly setting a node at the edge of the 1D grid to the desired incident wave form, this perturbation will naturally propagate onto the two-dimensional simulation.

## 4.7
## Near-to-Far-Field Transformation

With the steady-state fields calculated as described in section 4.5 from the nodes in region 2 of the TFSF technique, a Near-to-Far-Field transformation can be employed to numerically obtain the scattering amplitude $A(\phi)$ of the structure of interest. The strategy consists of constructing a fictitious boundary within region 2 and taking advantage of the equivalence principle as shown in figure 4.4.

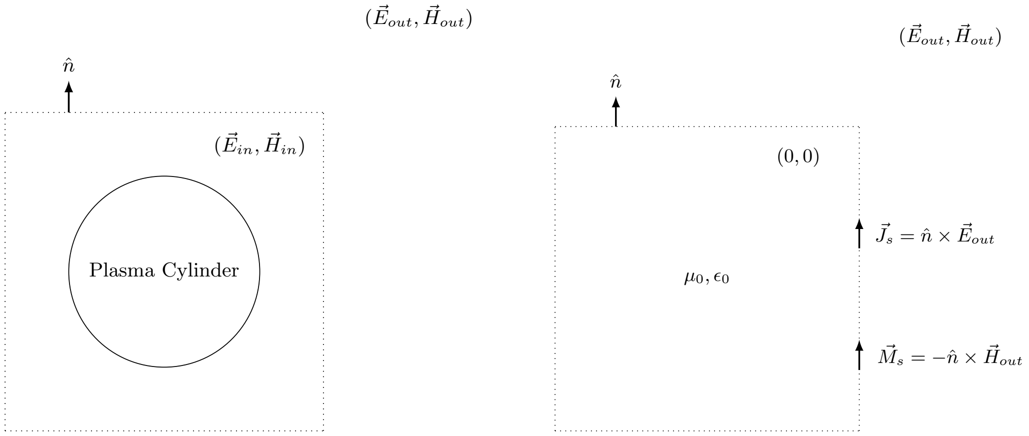

4.4(a): Fictitious boundary for the problem at hand. Fields inside and outside the boundary are continuous across it.

4.4(b): Equivalent problem with fields inside the fictitious boundary set to zero and material properties set to that of free-space.

Figure 4.4: Equivalence principle.

With the equivalent electric and magnetic currents at the fictitious boundary, the electromagnetic potentials for a two-dimensional problem can be written in terms of Green's functions (see Appendix B) as

$$\vec{A}(\vec{\rho}) = -i\frac{\mu}{4}\oint_L \vec{J}_s(\vec{\rho'})H_0^{(2)}(k|\vec{\rho} - \vec{\rho'}|)\mathrm{d}l', \tag{4-33a}$$

$$\vec{F}(\vec{\rho}) = -i\frac{\epsilon}{4}\oint_L \vec{M}_s(\vec{\rho'})H_0^{(2)}(k|\vec{\rho} - \vec{\rho'}|)\mathrm{d}l', \tag{4-33b}$$

where primed coordinates denote points upon the fictitious boundary and the closed path integral is calculated over the boundary.

With the electromagnetic potentials, the scattered fields can be found by means of equation (3-3), repeated here for convenience,

$$\vec{E} = -\frac{1}{\epsilon}\nabla \times \vec{F} + i\omega\vec{A} + \frac{i}{\omega\mu\epsilon}\nabla(\nabla \cdot \vec{A}), \tag{3-3a}$$

$$\vec{H} = \frac{1}{\mu}\nabla \times \vec{A} + i\omega\vec{F} + \frac{i}{\omega\mu\epsilon}\nabla(\nabla \cdot \vec{F}). \tag{3-3b}$$

Additionally, by considering an observation point in the far field, the asymptotic expression for the Hankel function can be used, resulting in, for the $z$-component of the electric field,

$$E_z^s(\vec{\rho}) = -\sqrt{\frac{i}{8\pi k}}\frac{e^{-ik\rho}}{\sqrt{\rho}} \oint\limits_L \left(\omega\mu_0\vec{J}_s(\vec{\rho'}) \cdot \hat{z} - k\vec{M}_s(\vec{\rho'}) \cdot \hat{\phi}\right) e^{ik\rho' \cos\psi}\mathrm{d}l', \tag{4-34}$$

where the angle $\psi$ is given by $\cos\psi = \hat{\rho}\cdot\hat{\rho}'$. The numerical scattering amplitude is then given by

$$A(\phi) = -\sqrt{\frac{i}{8\pi k}} \oint\limits_L \left(\omega\mu_0\vec{J}_s(\vec{\rho'}) \cdot \hat{z} - k\vec{M}_s(\vec{\rho'}) \cdot \hat{\phi}\right) e^{ik\rho' \cos\psi}\mathrm{d}l', \tag{4-35}$$

which can be readily calculated with the application of Simpson's rule, as all necessary quantities are known at the end of the FDTD run.

# 5
# Results

## 5.1
## Validating Results for the Eigenfunction Method

To validate the methods described in the previous chapters and ensure their correct implementation, they are first applied to simpler problems with known solutions.

The eigenfunction method described in Chapter 3 is applied to the dielectric shell depicted in figure 5.1. By making $r_1 = 0.3\lambda$, $r_2 = 0.25\lambda$ and $\epsilon_r = 4$, this dielectric shell is identical to the one studied by Richmond [38]. The dielectric shell is separated into two regions for application of the eigenfunction method, obeying the shell's natural boundaries.

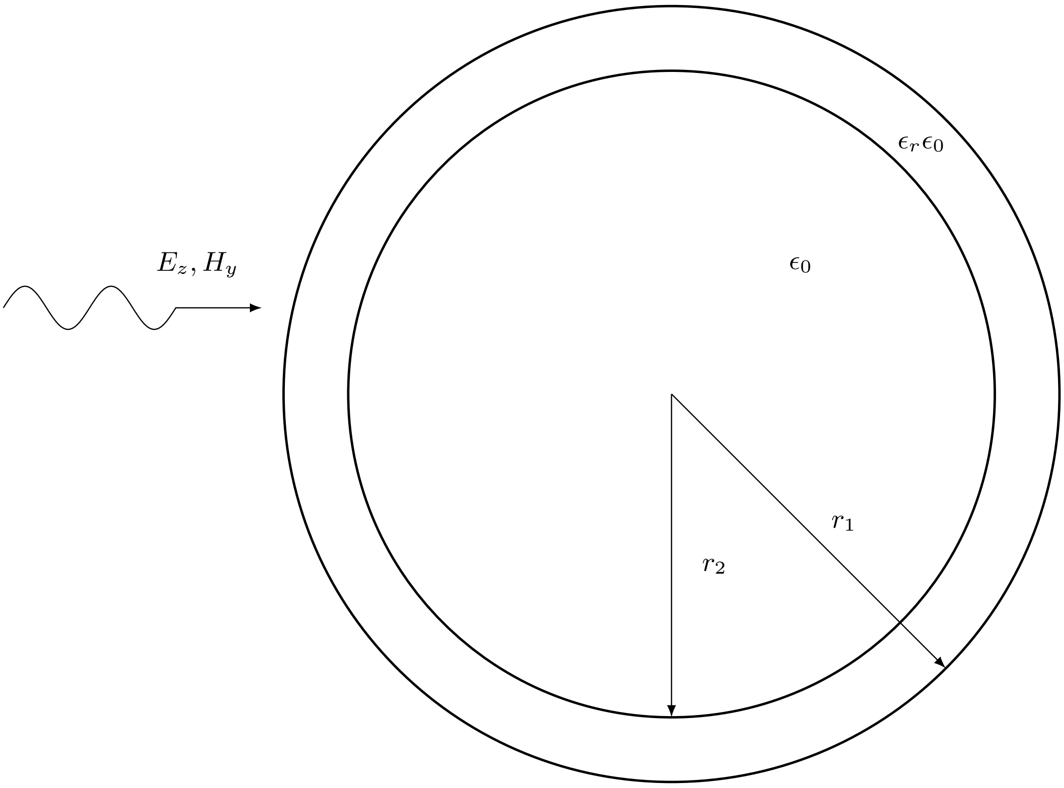

Figure 5.1: Dielectric shell used for the validation of the eigenfunction method. With $r_1 = 0.3\lambda$, $r_2 = 0.25\lambda$ and $\epsilon_r = 4$, this is the same shell studied by Richmond.

Figure 5.2 shows a comparison of the results for the scattering cross-sections of a TMz field incident on the dielectric shell described in figure 5.1 obtained by the application of the eigenfunction method described in Chapter 3 and Richmond's results.

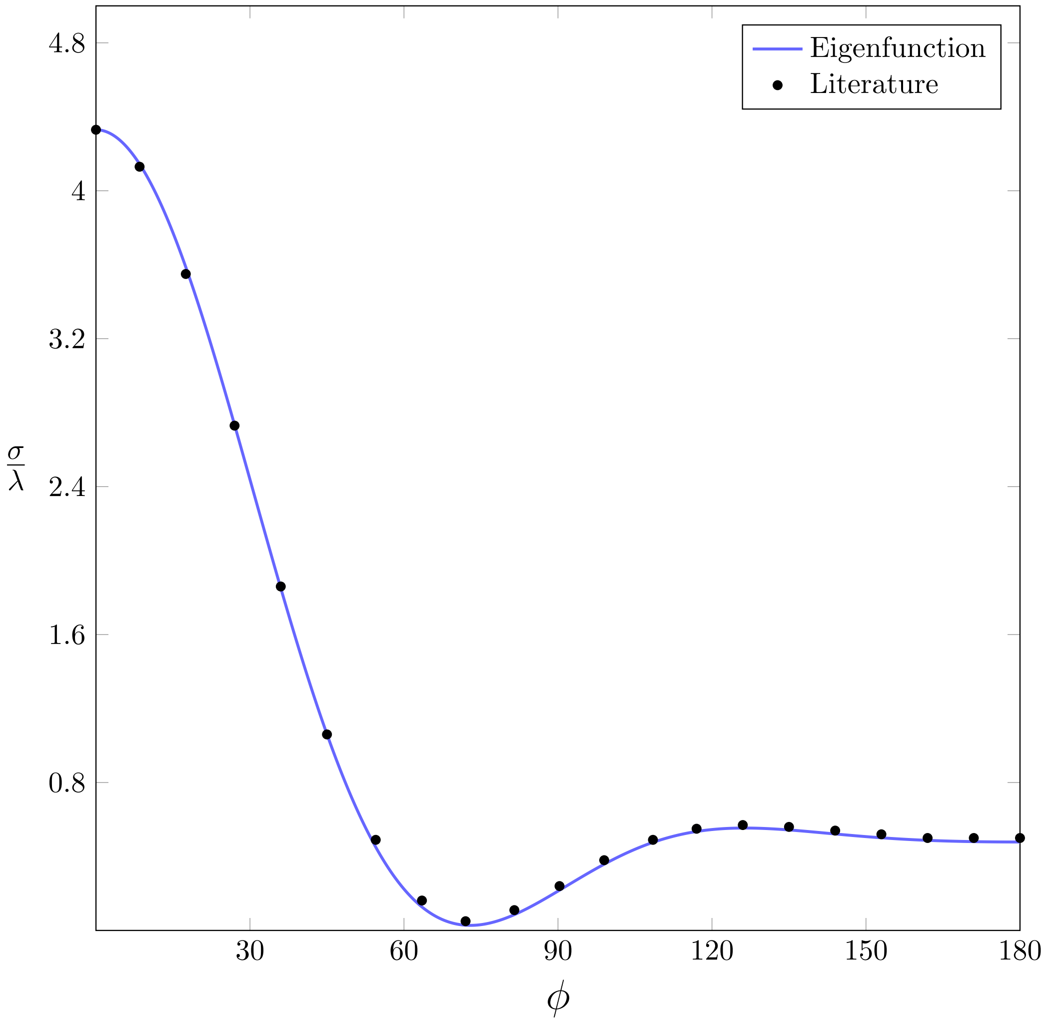

Figure 5.2: Comparison of scattering cross-sections obtained by the eigenfunction method with those from the literature for a TMz field incident on the dielectric shell described in figure 5.1.

Figure 5.3 shows a comparison of the results for the absolute field values within the dielectric shell, at $\rho = \frac{(r_1+r_2)}{2}$, the middle of the dielectric shell, for the same problem.

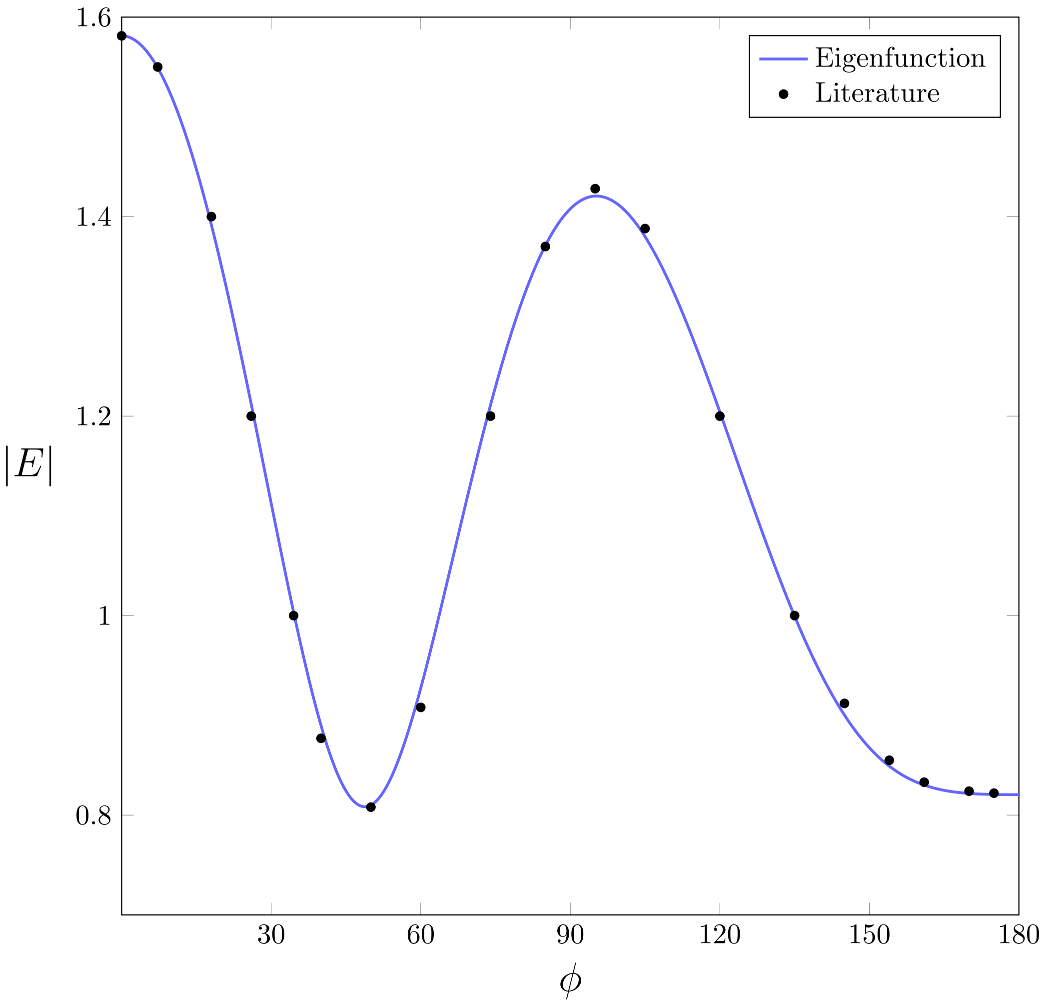

Figure 5.3: Comparison of internal electric fields, in volts/meter, at $\rho = (r_1 + r_2)/2$, the middle of the dielectric shell, obtained by the eigenfunction method with those from the literature for a TMz field incident on the dielectric shell described in figure 5.1.

A second test consists of solving the same problem, but treating the dielectric shell as an inhomogeneous cylinder and separating it into 18 equally spaced regions. The number 18 was chosen so that the arbitrary region separation coincides with the natural shell boundaries at $\rho = r_2$. The results are identical to the previous case, as expected.

A third test consists of applying the eigenfunction method to the lossy multi-layered cylinder depicted in figure 5.4. With $k_0 r_1 = 0.4\pi$, $k_0 r_2 = 0.3\pi$, $\epsilon_1 = 6 - i0.5$ and $\epsilon_2 = 67 - i43$, this is the same structure studied by Bussey and Richmond [39], and their results are used as reference values.

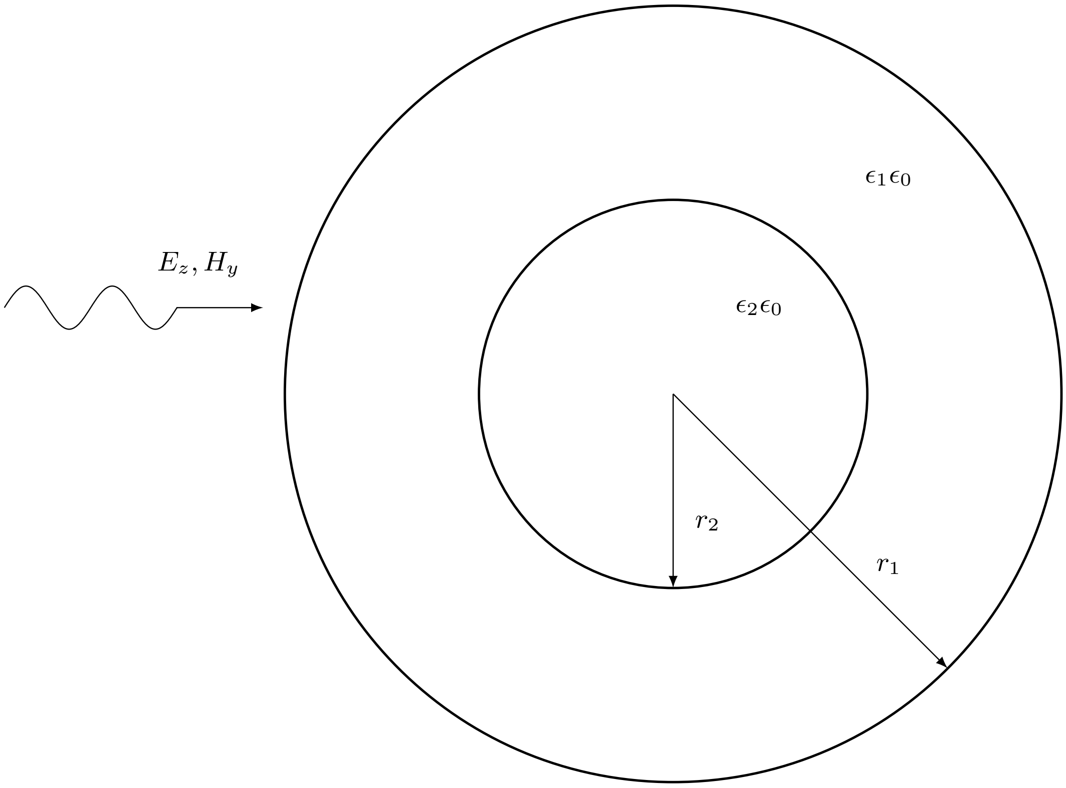

Figure 5.4: Multi-layered lossy dielectric used for the validation of the eigenfunction method. With $k_0r_1 = 0.4\pi$, $k_0r_2 = 0.3\pi$, $\epsilon_1 = 6 - i0.5$ and $\epsilon_2 = 67 - i43$, this is the same structure studied by Bussey and Richmond.

Table 5.1 presents a comparison between the scattering coefficients $b_n$ obtained by the eigenfunction method with those from Bussey and Richmond. The results match up to the precision provided in the reference work.

| | **Eigenfunction** | | **Reference** | |
|---|---|---|---|---|
| n | Real Part | Imaginary Part | Real Part | Imaginary Part |
| 0 | -0.825219 | 0.011070 | -0.82522 | 0.01107 |
| 1 | -0.248603 | 0.266700 | -0.24860 | 0.26670 |
| 2 | -0.036658 | 0.033705 | -0.03666 | 0.03371 |
| 3 | -0.002219 | 0.000467 | -0.00222 | 0.00047 |
| 4 | -0.000048 | -0.000012 | -0.00005 | -0.00001 |
| 5 | $0. \times 10^{-7}$ | $0. \times 10^{-7}$ | -0.00000 | -0.00000 |

Table 5.1: Comparison of scattering coefficients $b_n$ obtained by the eigenfunction method with those from the literature for a TMz field incident on the lossy multi-layered dielectric described in figure 5.4.

## 5.2 Homogeneous Plasma Cylinder

An homogeneous plasma cylinder is now investigated by means of the eigenfunction expansion method and of the FDTD simulations described in chapter 4. A baseline case for comparison purposes is chosen with parameters shown in Table 5.2; these plasma parameters correspond approximately to argon gas maintained at a constant pressure of 133 Pa (1 Torr), a common experimental set-up for contained plasmas used as antennas [4].

| **Parameter** | **Value** |
|---|---|
| Time Discretization $\Delta_t$ | $2.35702 \times 10^{-12}$ s |
| Spatial Discretization $\Delta_s$ | $1 \times 10^{-3}$ m |
| Maximum Temporal Step $N_t$ | 1200 |
| Maximum Spatial Step $N_s$ | 251 |
| Incident Wave Frequency $f_{in}$ | $10 \times 10^9$ Hz |
| Plasma Radius $r$ | 0.09 m |
| Homogeneous Plasma Density $n_0$ | $5 \times 10^{17}$ m$^{-3}$ |
| Plasma Collision Frequency $\nu$ | $500 \times 10^6$ Hz |

Table 5.2: Parameters for the baseline case of the homogeneous plasma cylinder.

The incident wave is a sinusoidal TMz pulse given by the discretized wave function

$$\psi(n) = e^{-\left(\frac{n-3\tau}{\tau}\right)^2} \sin(\omega_{in} n \Delta_t), \tag{5-1}$$

with $\tau = 100$, shown in figure 5.5. The maximum temporal time step was chosen so that the fields excited by this incident wave function within the computational domain have sufficient time to dissipate, thus ensuring the accuracy of the Fourier Transforms applied in the numerical algorithm.

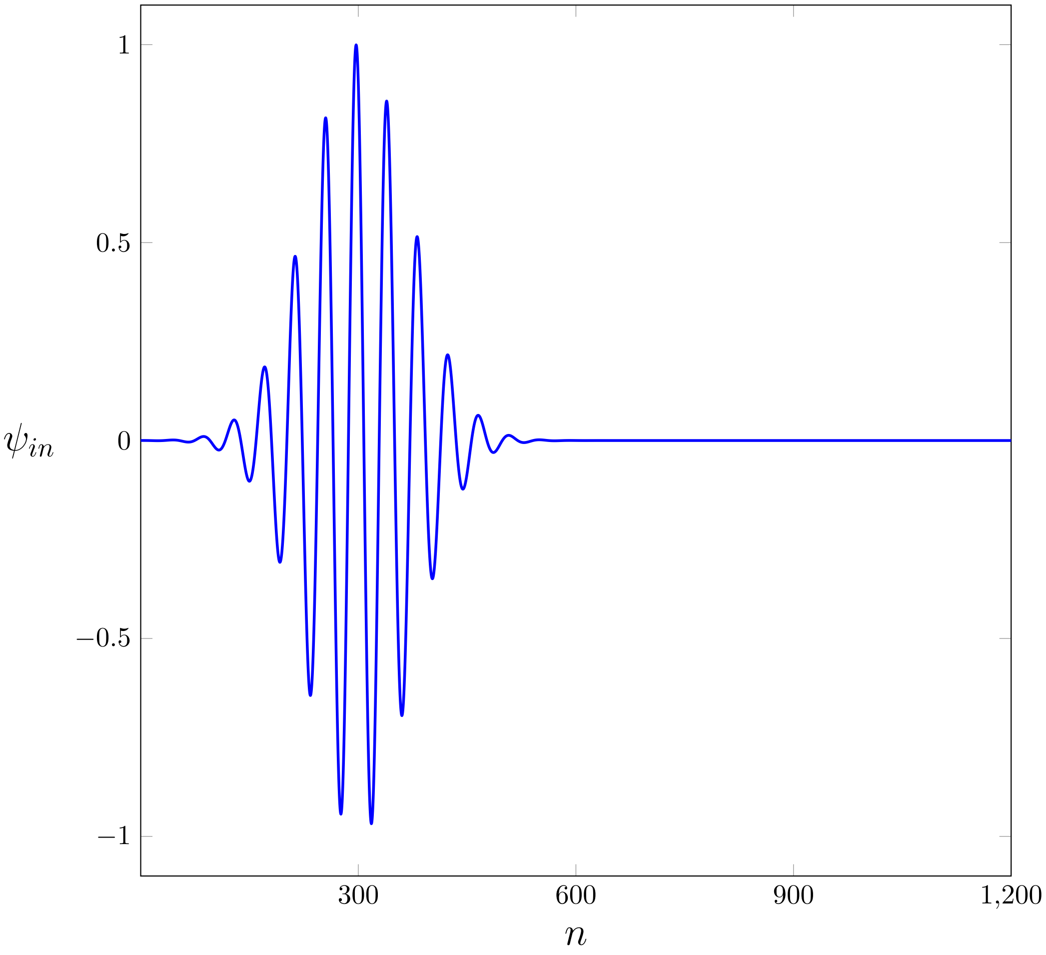

Figure 5.5: Incident wave function versus numerical time-step for the baseline homogeneous plasma cylinder problem given by the parameters in table 5.2.

Figure 5.6 shows the time evolution of the electric field within the homogeneous plasma cylinder for a few chosen time-steps. At the time-step $n = 1000$ there are still non-zero field perturbations within the computational domain, but they have almost vanished; by the maximum time-step $N_t = 1200$ they have completely dissipated.

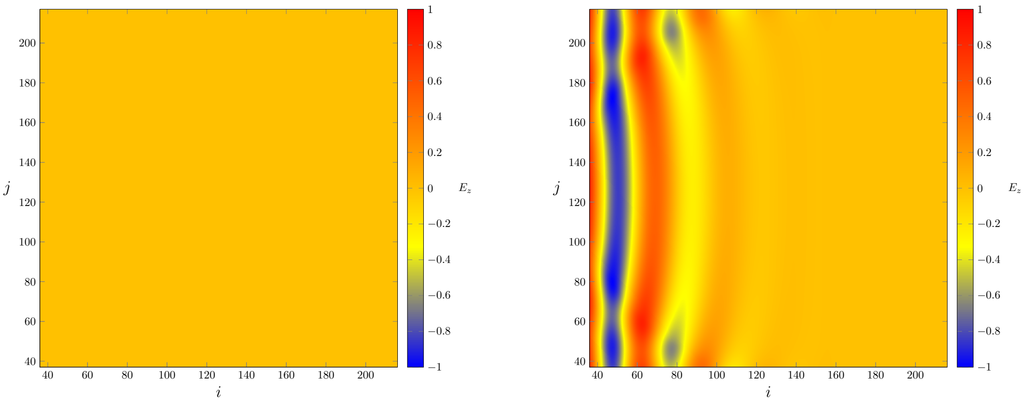

5.6(a): $n = 0$.

5.6(b): $n = 200$.

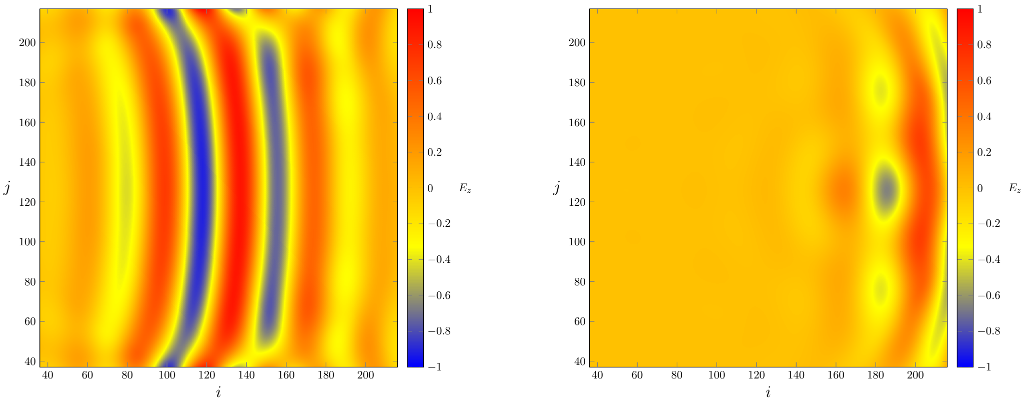

5.6(c): $n = 400$.

5.6(d): $n = 600$.

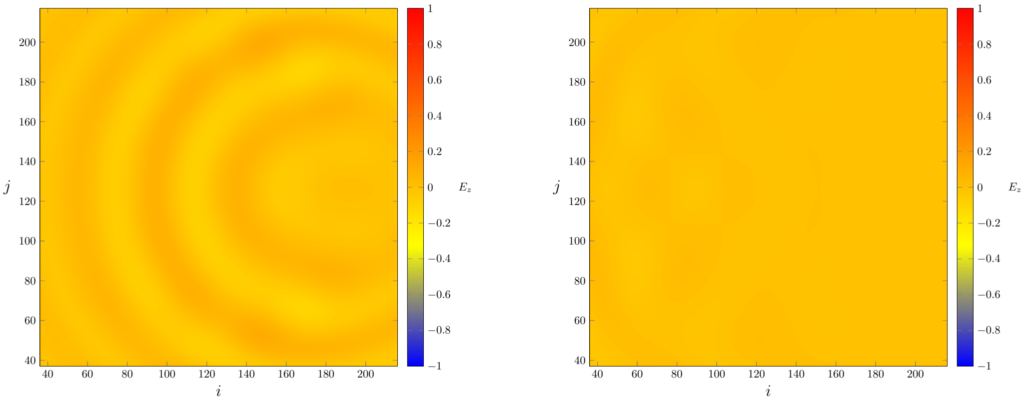

5.6(e): $n = 800$.

5.6(f): $n = 1000$.

Figure 5.6: Time evolution of the numerical solution, in volts/meter, for the baseline homogeneous plasma cylinder problem given by the parameters in table 5.2.

Figure 5.7 shows the comparison between the resulting scattering amplitude for the electric field obtained by the eigenfunction expansion method and the FDTD simulation. Excellent agreement is found between the two approaches.

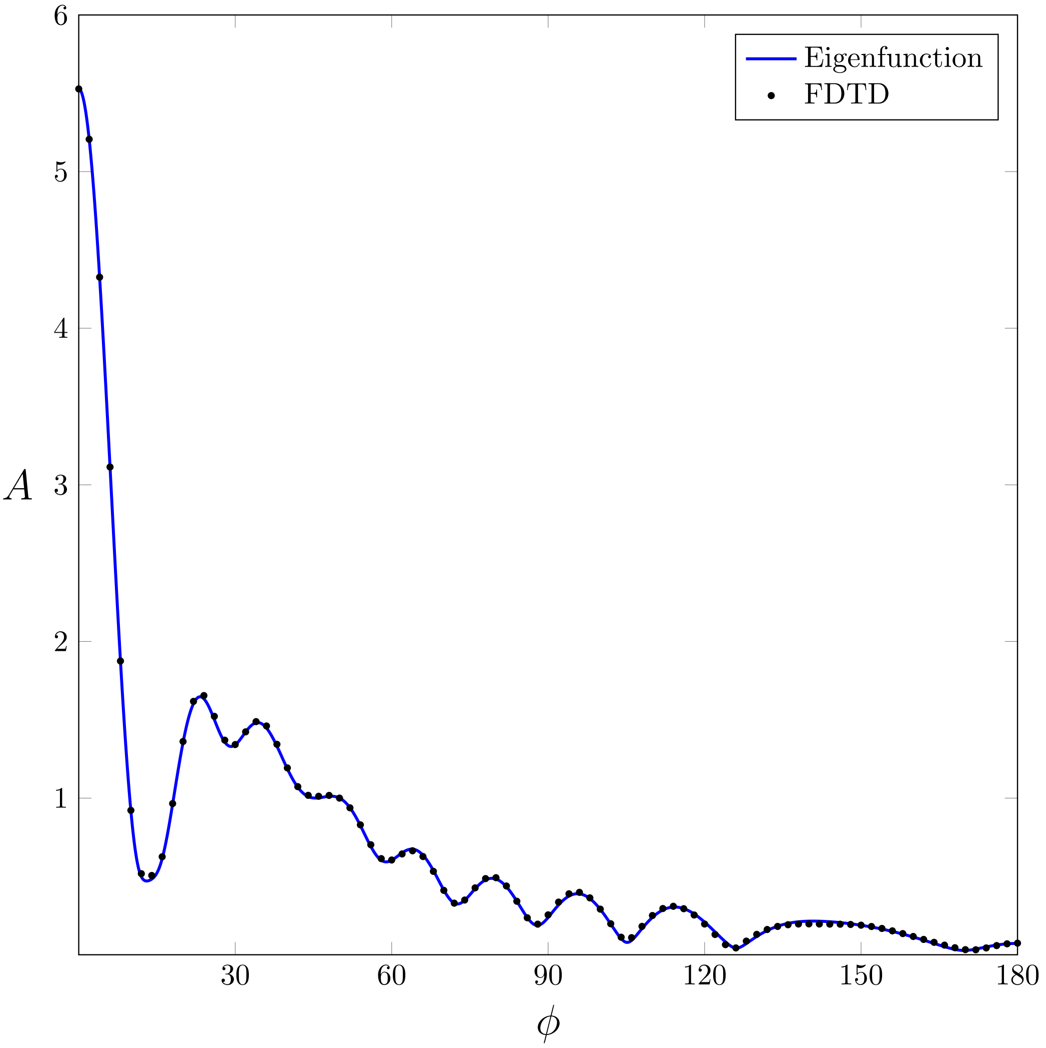

Figure 5.7: Comparison between the scattering amplitudes obtained by the eigenfunction method and the FDTD simulation for the baseline homogeneous plasma cylinder problem given by the parameters in table 5.2.

Figure 5.8 shows the comparison between the magnitude of the electric field within the plasma cylinder obtained by the eigenfunction expansion method and the FDTD simulation.

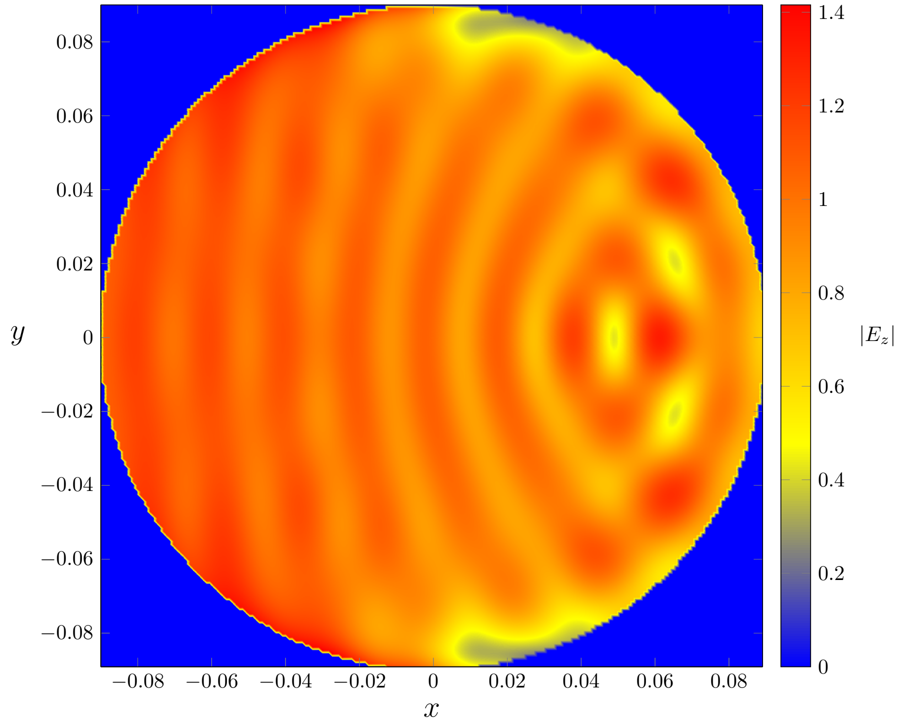

5.8(a): Eigenfunction method.

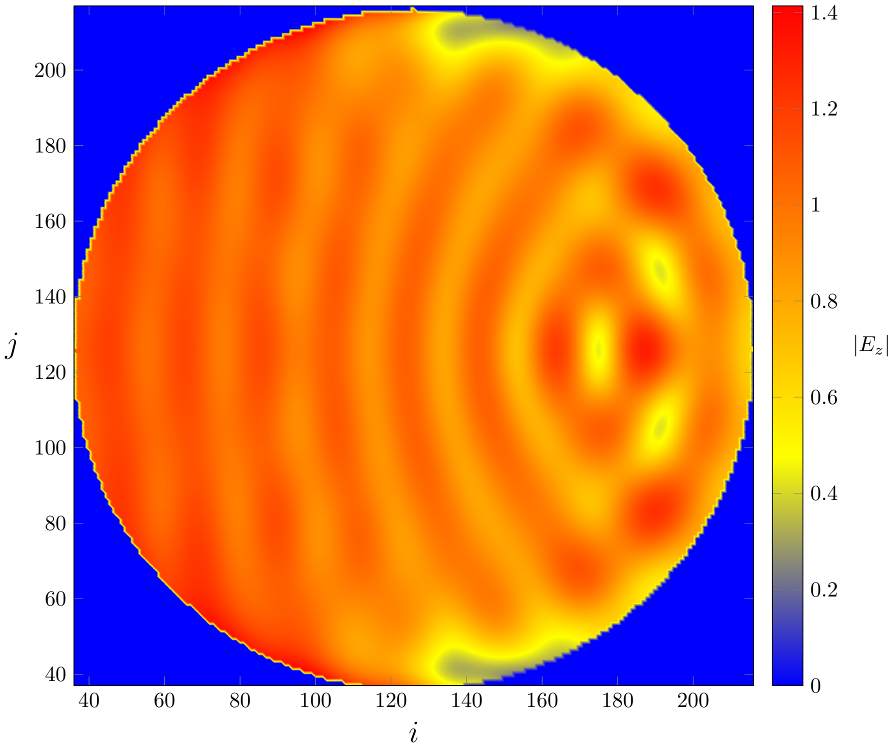

5.8(b): FDTD simulation.

Figure 5.8: Comparison between the magnitude of the electric field, in volts/meter, within the cylinder obtained through the eigenfunction method and the FDTD simulation for the baseline homogeneous plasma cylinder problem given by the parameters in table 5.2.

The electric fields inside the cylinder obtained by the eigenfunction method and by the FDTD simulation seem to be in good agreement, but colour-coded two-dimensional plots are difficult to be precisely analysed. For that reason, figures 5.9 and 5.10 provide linear plots of the magnitude of the electric field for $y = 0$ and $x = 0$ cuts, respectively.

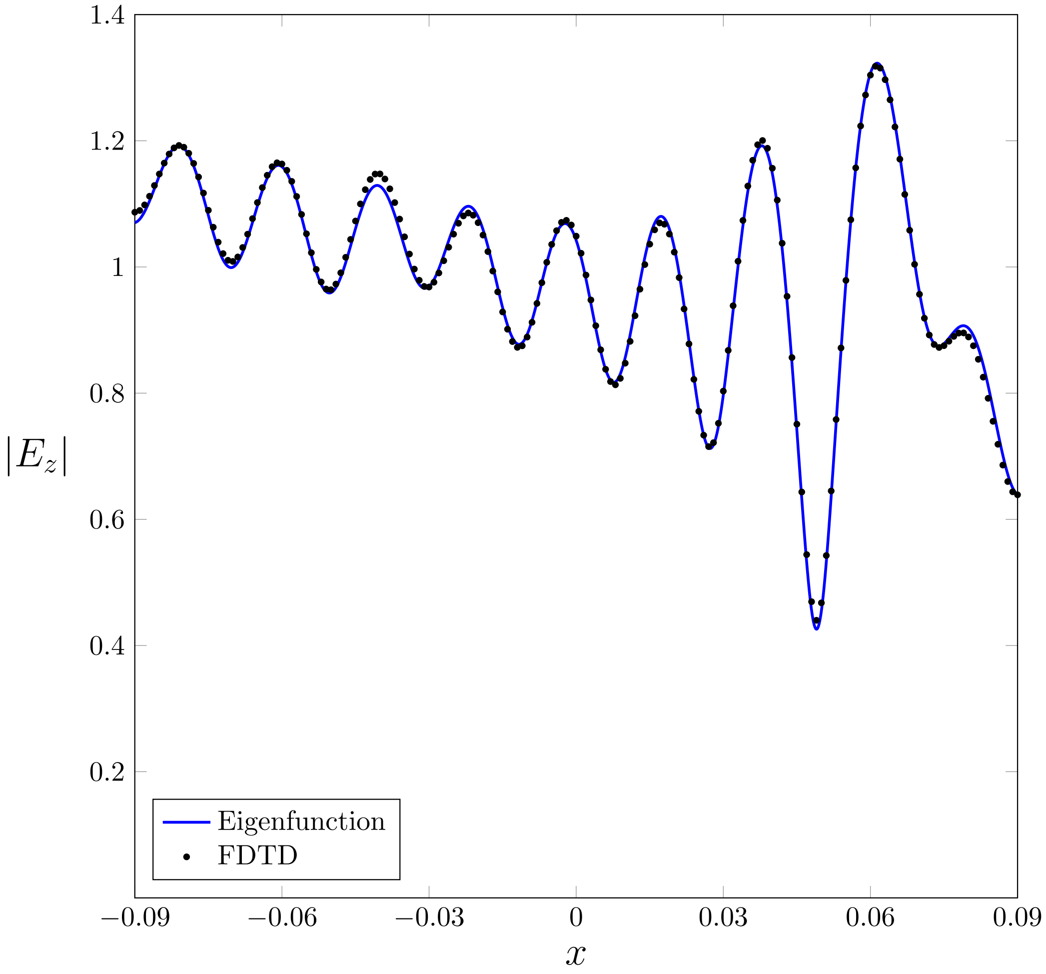

Figure 5.9: Comparison between the absolute electric field, in volts/meter, inside the cylinder for different values of $x$ and for $y = 0$, obtained by the eigenfunction method and the FDTD simulation for the baseline homogeneous plasma cylinder problem given by the parameters in table 5.2.

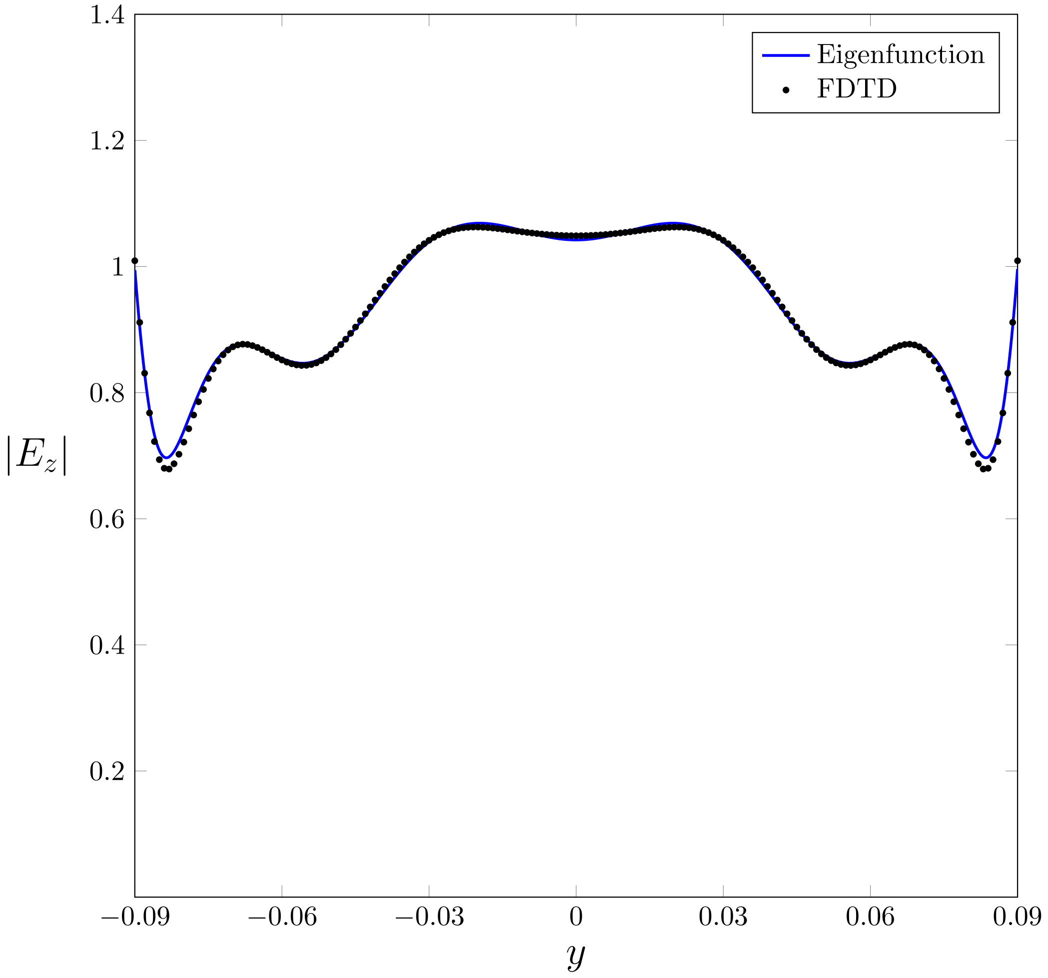

Figure 5.10: Comparison between the absolute electric field, in volts/meter, inside the cylinder for different values of $y$ and for $x = 0$, obtained by the eigenfunction method and the FDTD simulation for the baseline homogeneous plasma cylinder problem given by the parameters in table 5.2.

### 5.2.1
### Incident Wave Frequency Effects

The influence of the incident wave's frequency is now investigated. The incident wave function retains its form, but now the parameter $\tau$ needs to be adjusted such that at least one full period of the sine wave is completed within the Gaussian window; failing to ensure this condition results in numerical errors in the Fourier Transforms employed in the algorithm. This increase in the Gaussian window must be accompanied by an increase in the maximum temporal step so that all fields excited within the computational domain have time to die down to zero, as before, but the simulation and plasma parameters are otherwise unchanged.

Figure 5.11 shows a comparison between the scattering amplitudes obtained by the eigenfunction method and the FDTD simulation for different incident frequencies while maintaining the rest of the parameters fixed to those given by table 5.2. Excellent agreement between the analytical method and the simulations is found for all frequencies.

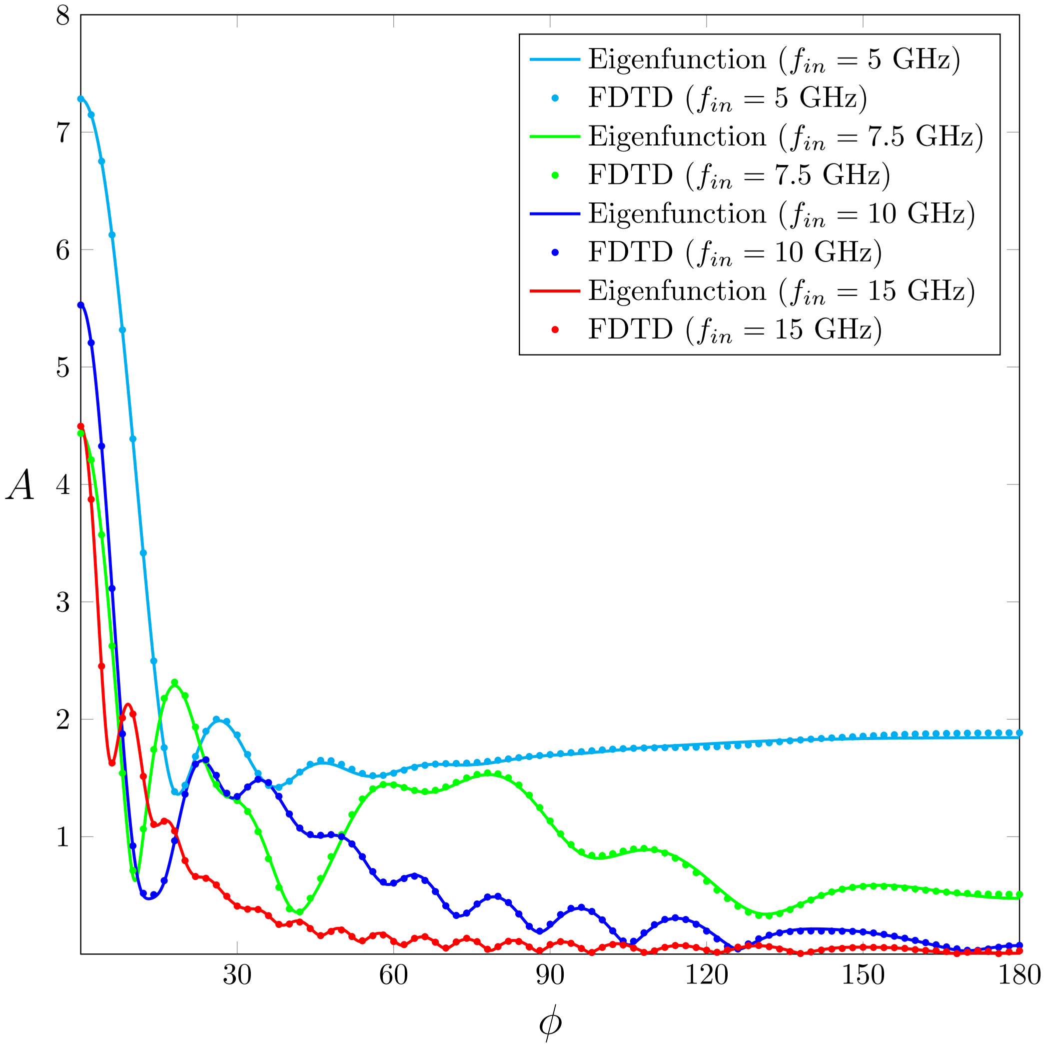

Figure 5.11: Comparison between the scattering amplitudes obtained by the eigenfunction method and the FDTD simulation for different incident frequencies; parameters are otherwise given by table 5.2.

Figure 5.12 shows a side-by-side comparison of colour-coded two-dimensional plots for the magnitude of the electric field inside the cylinder for both the eigenfunction method and the FDTD simulations, for incident frequencies below the baseline frequency of 10 GHz, while Figure 5.13 shows the same, but for incidence frequencies above the baseline frequency of 10 GHz.

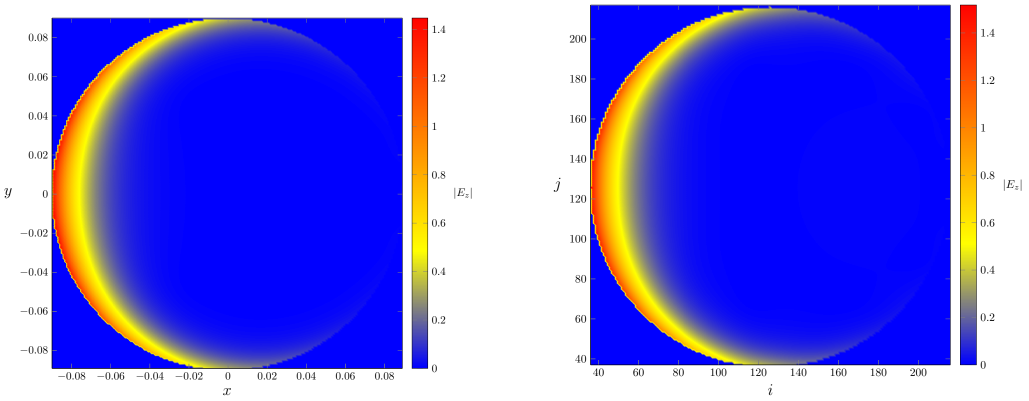

5.12(a): Eigenfunction method, $f_{in} = 5$ GHz.

5.12(b): FDTD simulation, $f_{in} = 5$ GHz.

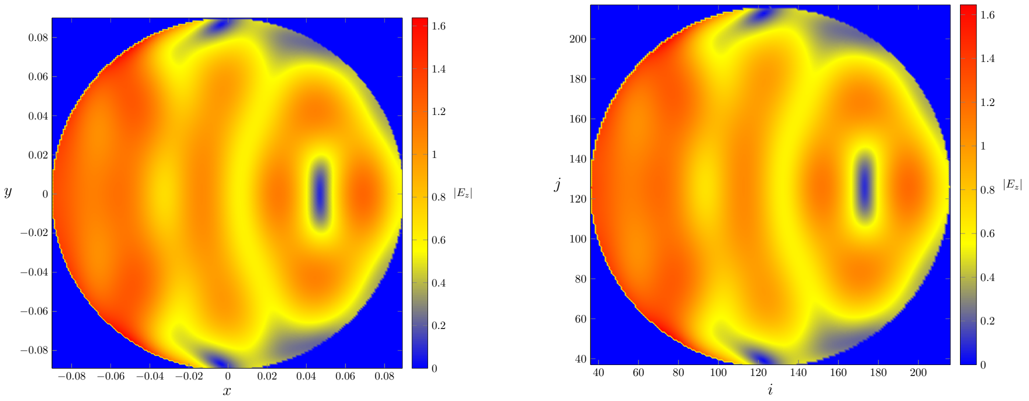

5.12(c): Eigenfunction method, $f_{in} = 7.5$ GHz.

5.12(d): FDTD simulation, $f_{in} = 7.5$ GHz.

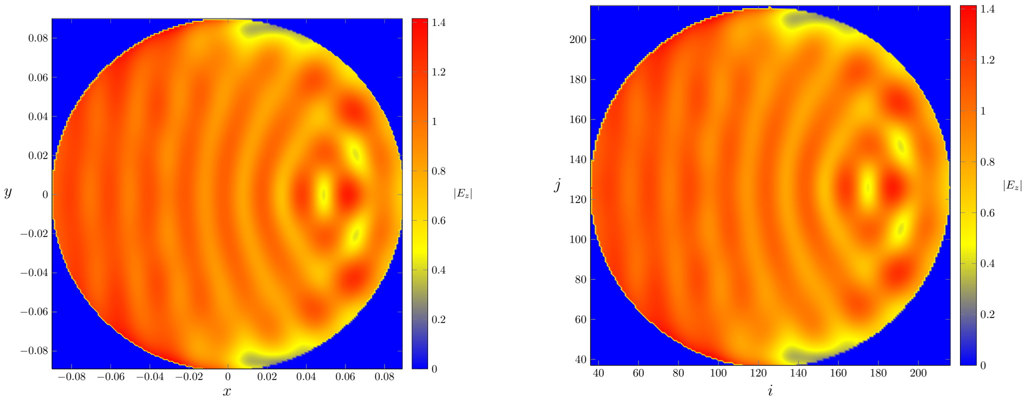

5.12(e): Eigenfunction method, $f_{in} = 10$ GHz.

5.12(f): FDTD simulation, $f_{in} = 10$ GHz.

Figure 5.12: Comparison between the magnitude of the electric field, in volts/meter, within the cylinder obtained by the eigenfunction method and the FDTD simulation for different incident frequencies below the baseline frequency of 10 GHz; parameters are otherwise given by table 5.2.

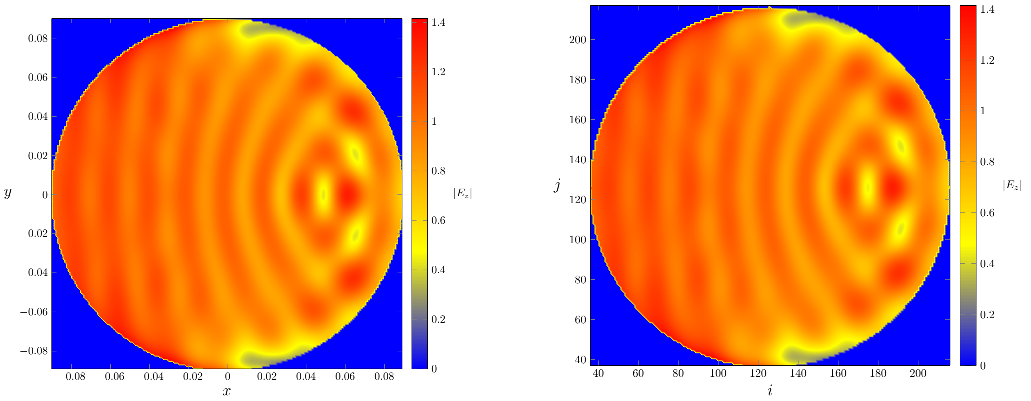

5.13(a): Eigenfunction method, $f_{in} = 10$ GHz.

5.13(b): FDTD simulation, $f_{in} = 10$ GHz.

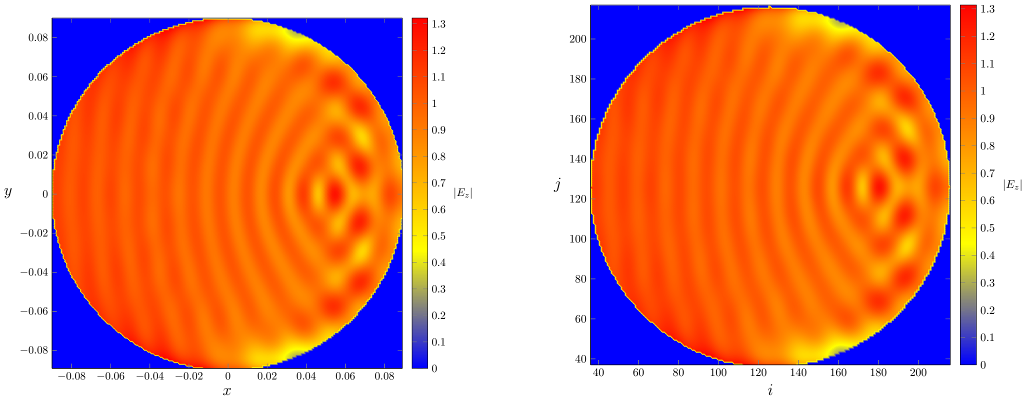

5.13(c): Eigenfunction method, $f_{in} = 12.5$ GHz.

5.13(d): FDTD simulation, $f_{in} = 12.5$ GHz.

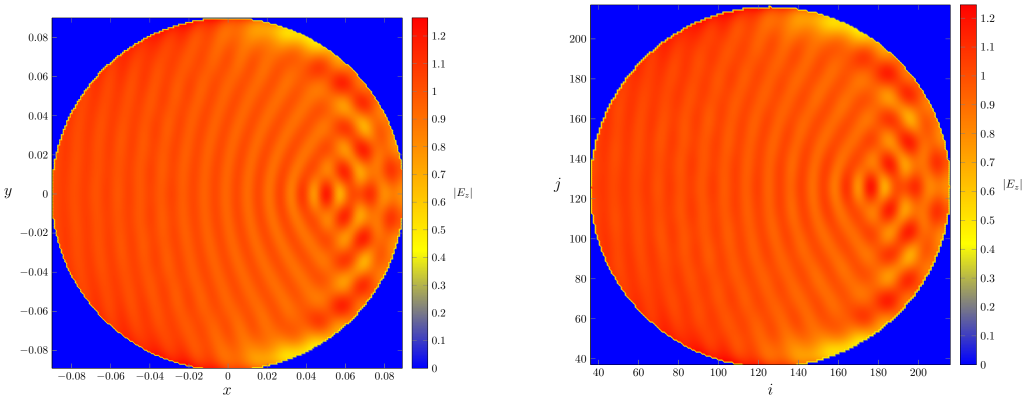

5.13(e): Eigenfunction method, $f_{in} = 15$ GHz.

5.13(f): FDTD simulation, $f_{in} = 15$ GHz.

Figure 5.13: Comparison between the magnitude of the electric field, in volts/meter, within the cylinder obtained by the eigenfunction method and the FDTD simulation for different incident frequencies above the baseline frequency of 10 GHz; parameters are otherwise given by table 5.2.

Again due to the difficulties of precisely comparing colour-coded two-dimensional plots, figures 5.14 and 5.15 show linear plots of the magnitude of the electric field inside the cylinder for $y = 0$ and $x = 0$ cuts, respectively, for the different frequencies under consideration. Since the differences in behaviour between the fields with $f_{in} = 12.5$ GHz and $f_{in} = 15$ GHz are not very large, the results for the former have been suppressed in the linear plots for the sake of not cluttering the graph.

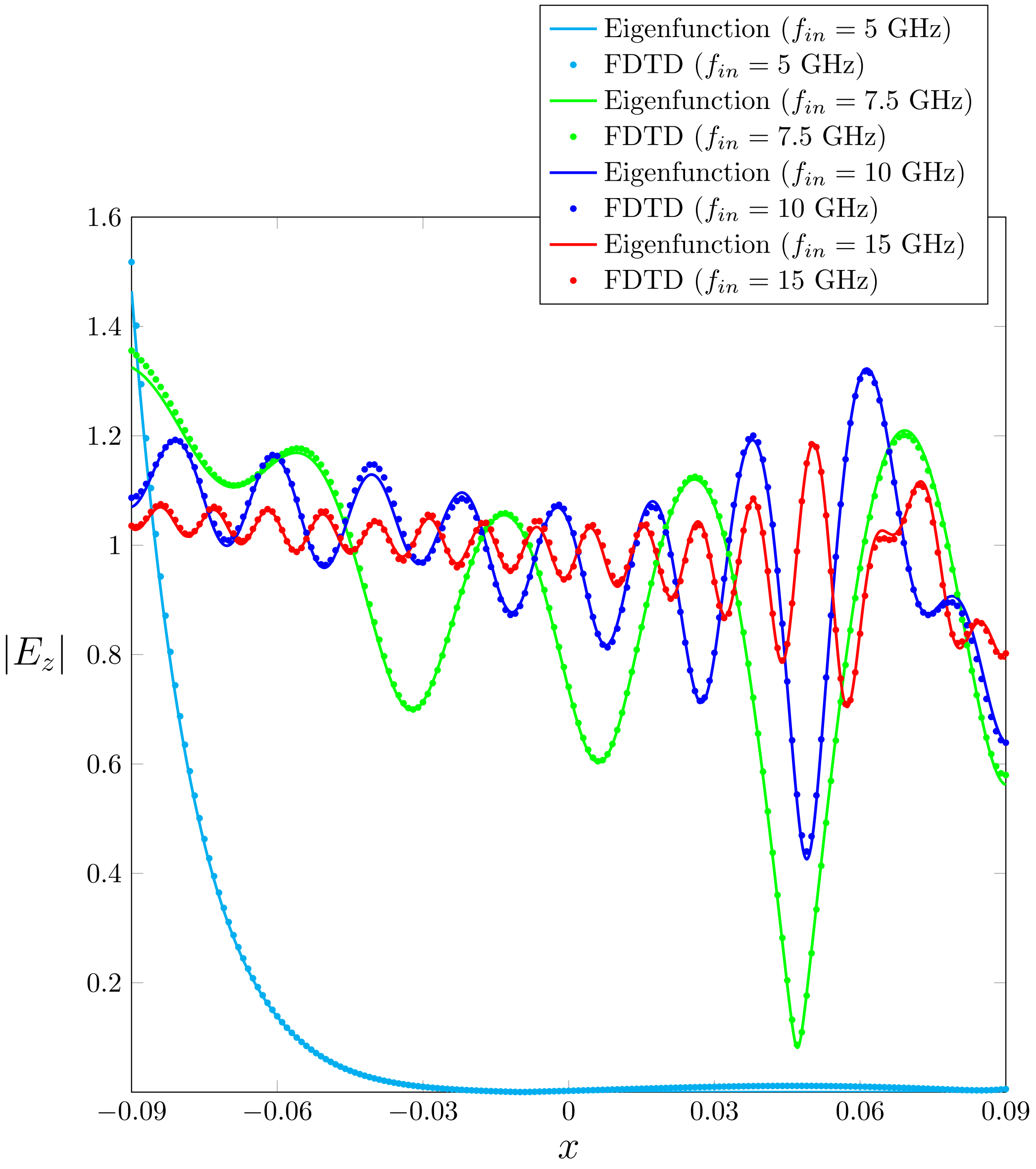

Figure 5.14: Comparison between the absolute electric field, in volts/meter, inside the cylinder for different values of $x$ and for $y = 0$ obtained by the eigenfunction method and the FDTD simulation for different incident frequencies; parameters are otherwise given by table 5.2.

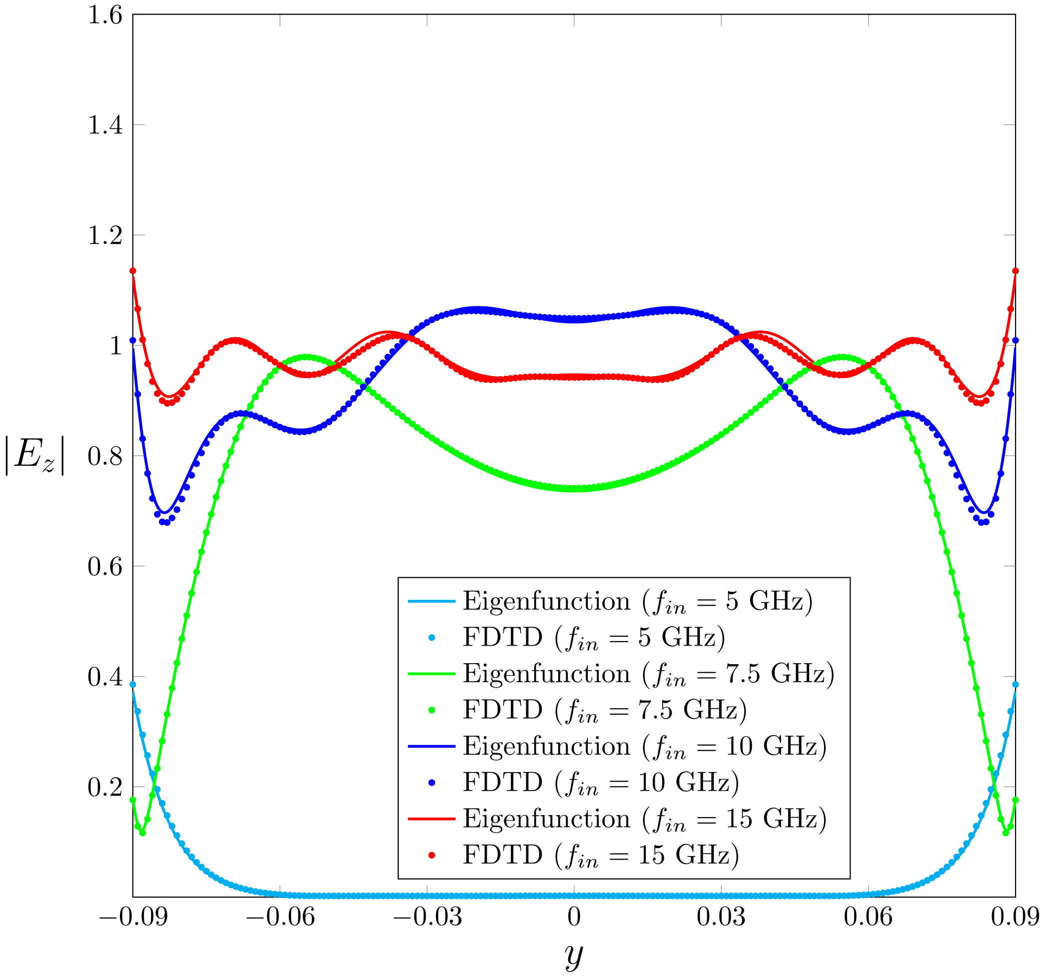

Figure 5.15: Comparison between the absolute electric field, in volts/meter, inside the cylinder for different values of $y$ and for $x = 0$ obtained by the eigenfunction method and the FDTD simulation for different incident frequencies; parameters are otherwise given by table 5.2.

### 5.2.2
### Plasma Density Effects

The influence of the plasma's homogeneous electron density is now investigated. Like before, other parameters are kept equal to those in table 5.2, but plasma density and maximum temporal step are changed.

Figure 5.16 shows a comparison between the scattering amplitudes obtained by the eigenfunction method and the FDTD simulation for different plasma densities. Good agreement between the analytical method and the simulations is found for all densities.

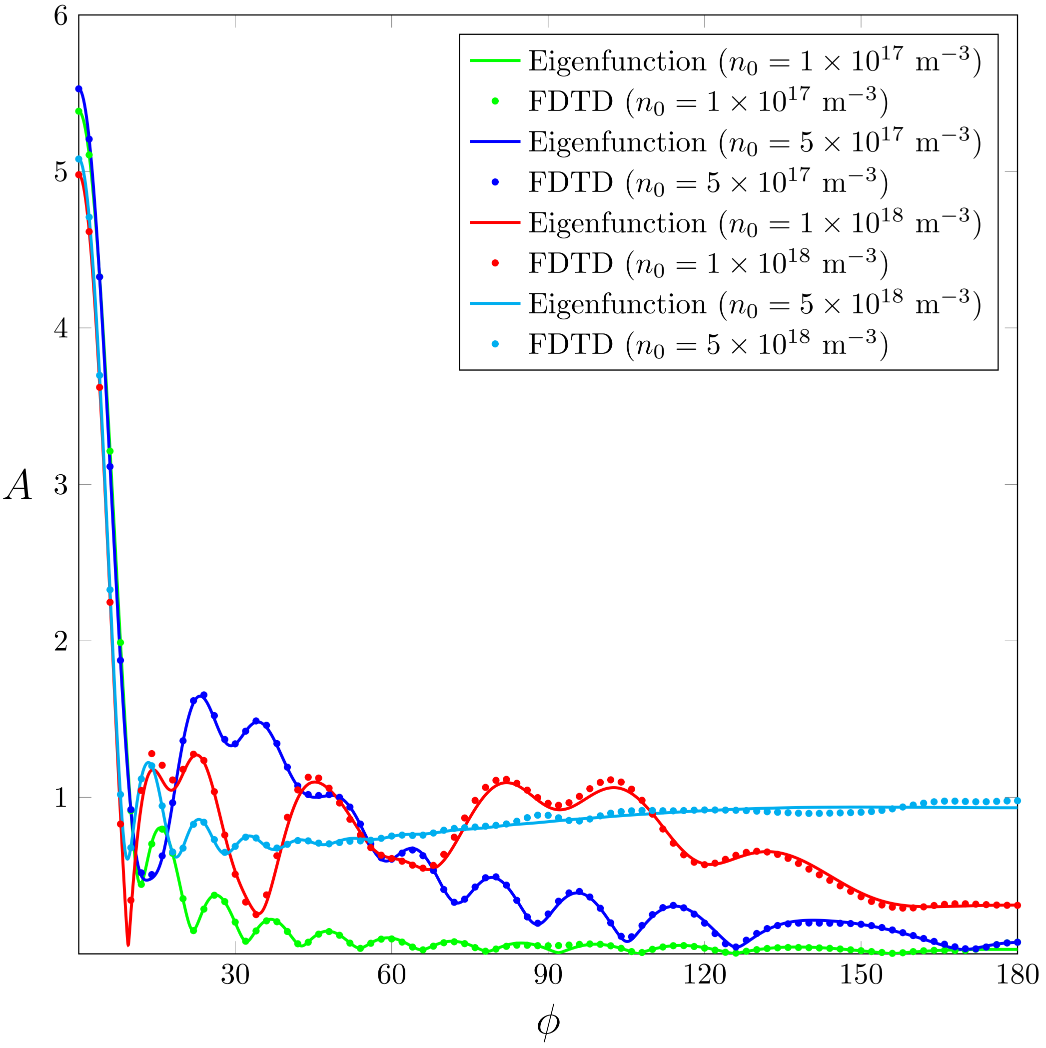

Figure 5.16: Comparison between the scattering amplitudes obtained by the eigenfunction method and the FDTD simulation for different plasma densities; parameters are otherwise given by table 5.2.

Figure 5.17 shows a side-by-side comparison of colour-coded two-dimensional plots for the magnitude of the electric field inside the cylinder for both the eigenfunction method and the FDTD simulations, for plasma densities equal to and higher than the baseline case of $n_0 = 5 \times 10^{17}$.

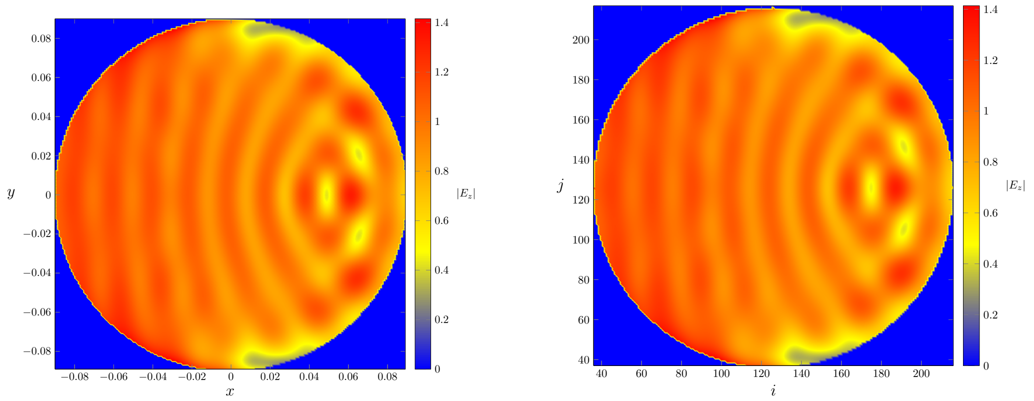

5.17(a): Eigenfunction method, $n_0 = 5 \times 10^{17}$ m$^{-3}$.

5.17(b): FDTD simulation, $n_0 = 5 \times 10^{17}$ m$^{-3}$.

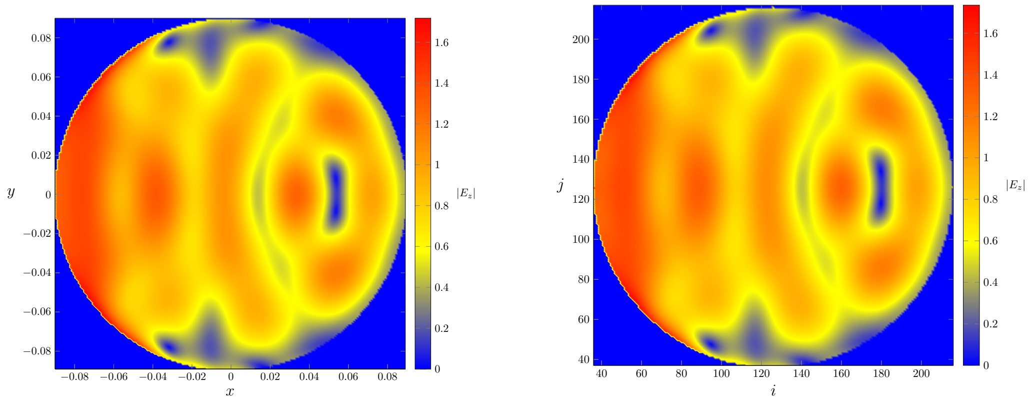

5.17(c): Eigenfunction method, $n_0 = 1 \times 10^{18}$ m$^{-3}$.

5.17(d): FDTD simulation, $n_0 = 1 \times 10^{18}$ m$^{-3}$.

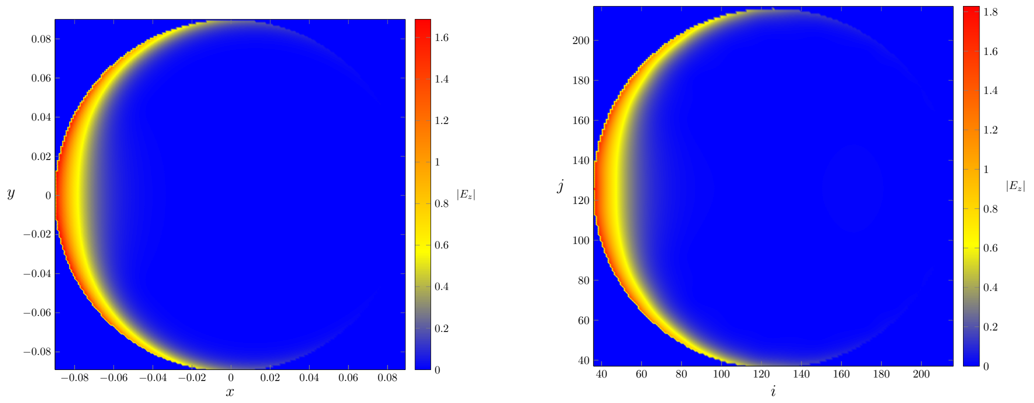

5.17(e): Eigenfunction method, $n_0 = 5 \times 10^{18}$ m$^{-3}$.

5.17(f): FDTD simulation, $n_0 = 5 \times 10^{18}$ m$^{-3}$.

Figure 5.17: Comparison between the magnitude of the electric field, in volts/meter, within the cylinder obtained by the eigenfunction method and the FDTD simulation for different plasma densities; parameters are otherwise given by table 5.2.

Again due to the difficulties of precisely comparing colour-coded two-dimensional plots, figures 5.18 and 5.19 show linear plots of the magnitude of the electric field inside the cylinder for $y = 0$ and $x = 0$ cuts, respectively, for the different plasma densities under consideration. The results for $n_0 = 1 \times 10^{17}$ m$^{-3}$ were not shown on the two-dimensional plots due to them being uninteresting (the plasma is almost completely transparent to the electromagnetic wave at these configurations), but they are shown here for the sake of comparison.

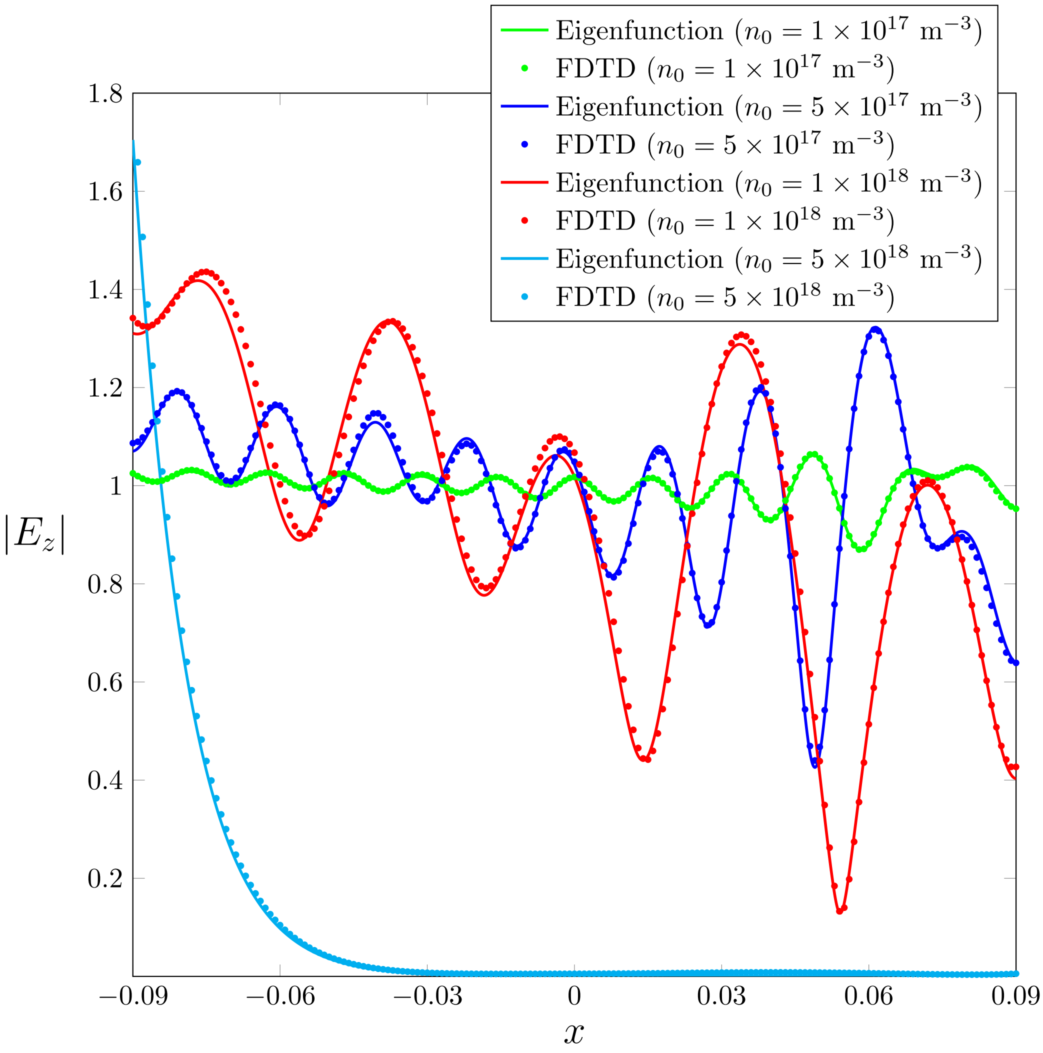

Figure 5.18: Comparison between the absolute electric field, in volts/meter, inside the cylinder for different values of $x$ and for $y = 0$ obtained by the eigenfunction method and the FDTD simulation for different plasma densities; parameters are otherwise given by table 5.2.

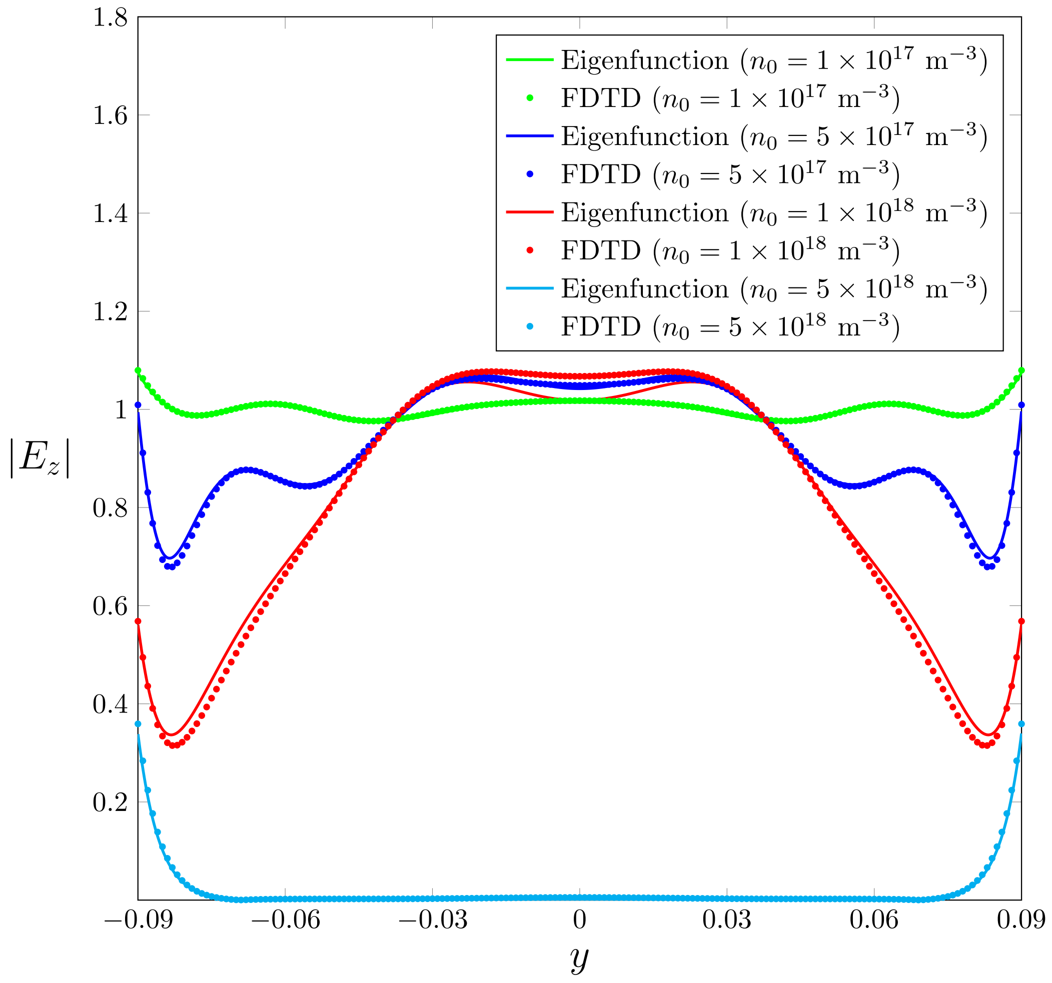

Figure 5.19: Comparison between the absolute electric field, in volts/meter, inside the cylinder for different values of $y$ and for $x = 0$ obtained by the eigenfunction method and the FDTD simulation for different plasma densities; parameters are otherwise given by table 5.2.

### 5.2.3
### Plasma Collision Frequency Effects

The influence of the plasma's collision frequency is now investigated. Like before, other parameters are kept equal to those in table 5.2, but collision frequency and maximum temporal step are changed.

Figure 5.20 shows a comparison between the scattering amplitudes obtained by the eigenfunction method and the FDTD simulation for different collision frequencies. Good agreement between the analytical method and the simulations is found for all frequencies.

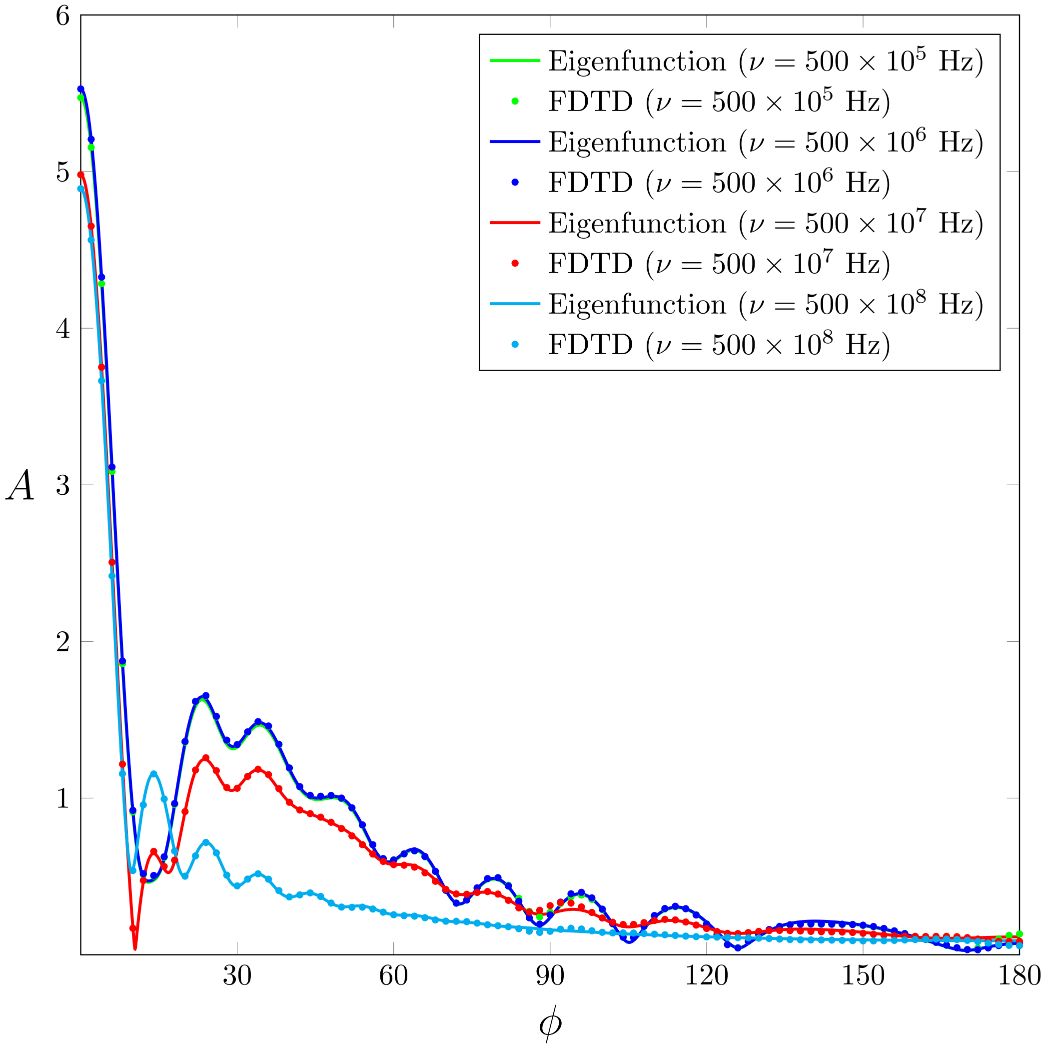

Figure 5.20: Comparison between the scattering amplitudes obtained by the eigenfunction method and the FDTD simulation for different collision frequencies; parameters are otherwise given by table 5.2. For $\nu = 500 \times 10^5$ Hz, in green, the results are almost identical to the baseline case, in blue, so the curves lie on top of each other.

Figure 5.21 shows a side-by-side comparison of colour-coded two-dimensional plots for the magnitude of the electric field inside the cylinder for both the eigenfunction method and the FDTD simulations, for collision frequencies equal to and higher than the baseline case of $\nu = 500 \times 10^6$ Hz.

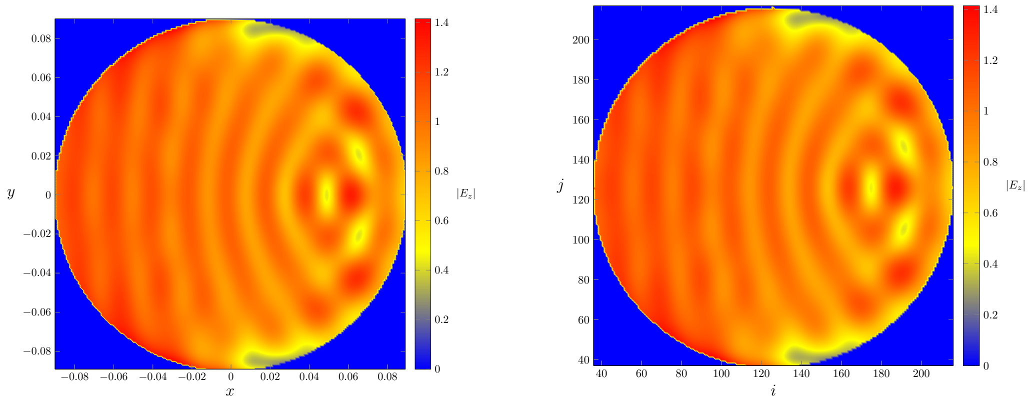

5.21(a): Eigenfunction method, $\nu = 500 \times 10^6$ Hz.

5.21(b): FDTD simulation, $\nu = 500 \times 10^6$ Hz.

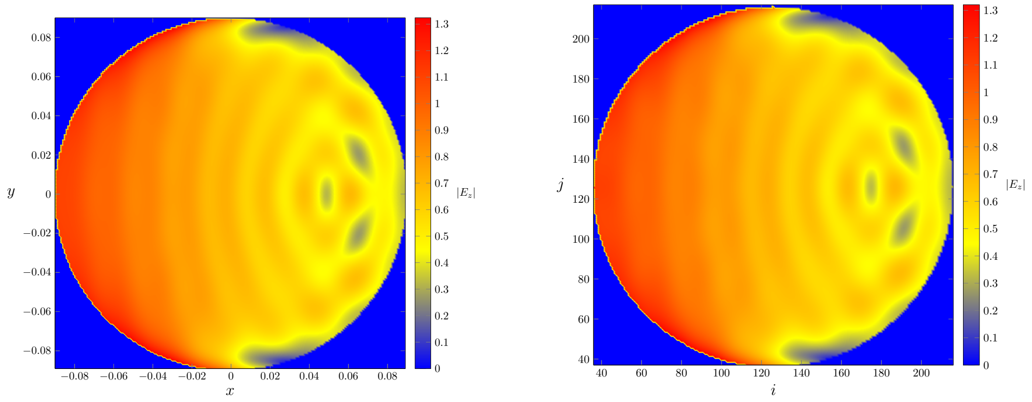

5.21(c): Eigenfunction method, $\nu = 500 \times 10^7$ Hz.

5.21(d): FDTD simulation, $\nu = 500 \times 10^7$ Hz.

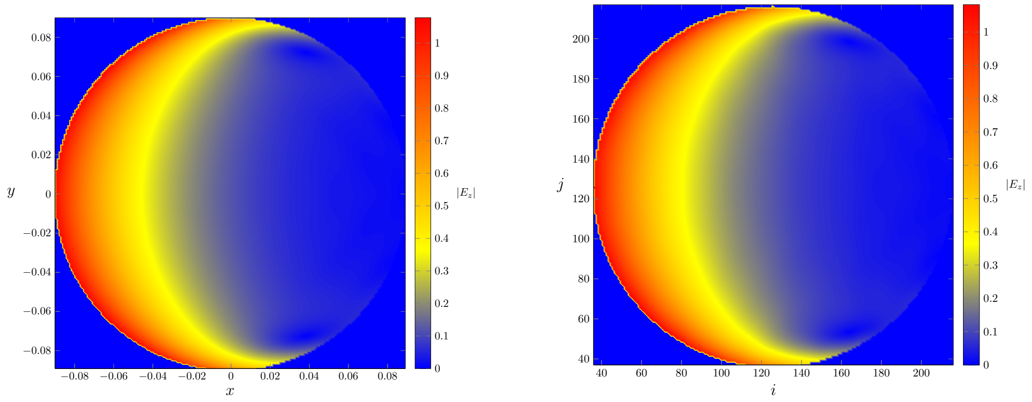

5.21(e): Eigenfunction method, $\nu = 500 \times 10^8$ Hz.

5.21(f): FDTD simulation, $\nu = 500 \times 10^8$ Hz.

Figure 5.21: Comparison between the magnitude of the electric field, in volts/meter, within the cylinder obtained by the eigenfunction method and the FDTD simulation for different collision frequencies; parameters are otherwise given by table 5.2.

Again due to the difficulties of precisely comparing colour-coded two-dimensional plots, figures 5.18 and 5.19 show linear plots of the magnitude of the electric field inside the cylinder for $y = 0$ and $x = 0$ cuts, respectively, for the different collision frequencies under consideration. The results for $\nu = 500 \times 10^5$ Hz were not shown on the two-dimensional plots due to them being almost identical to the baseline case, but they are shown here for the sake of comparison.

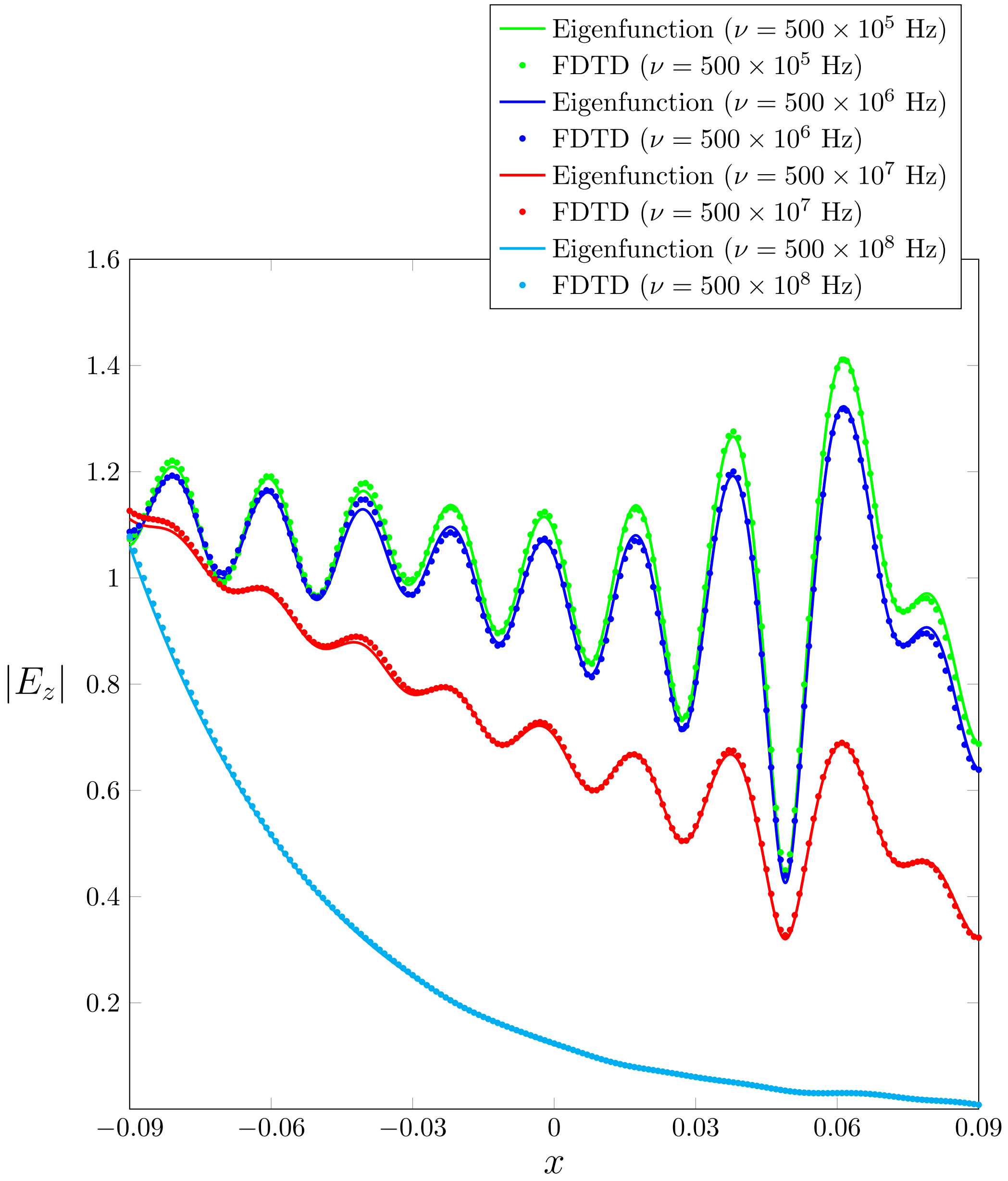

Figure 5.22: Comparison between the absolute electric field, in volts/meter, inside the cylinder for different values of $x$ and for $y = 0$ obtained by the eigenfunction method and the FDTD simulation for different collision frequencies; parameters are otherwise given by table 5.2.

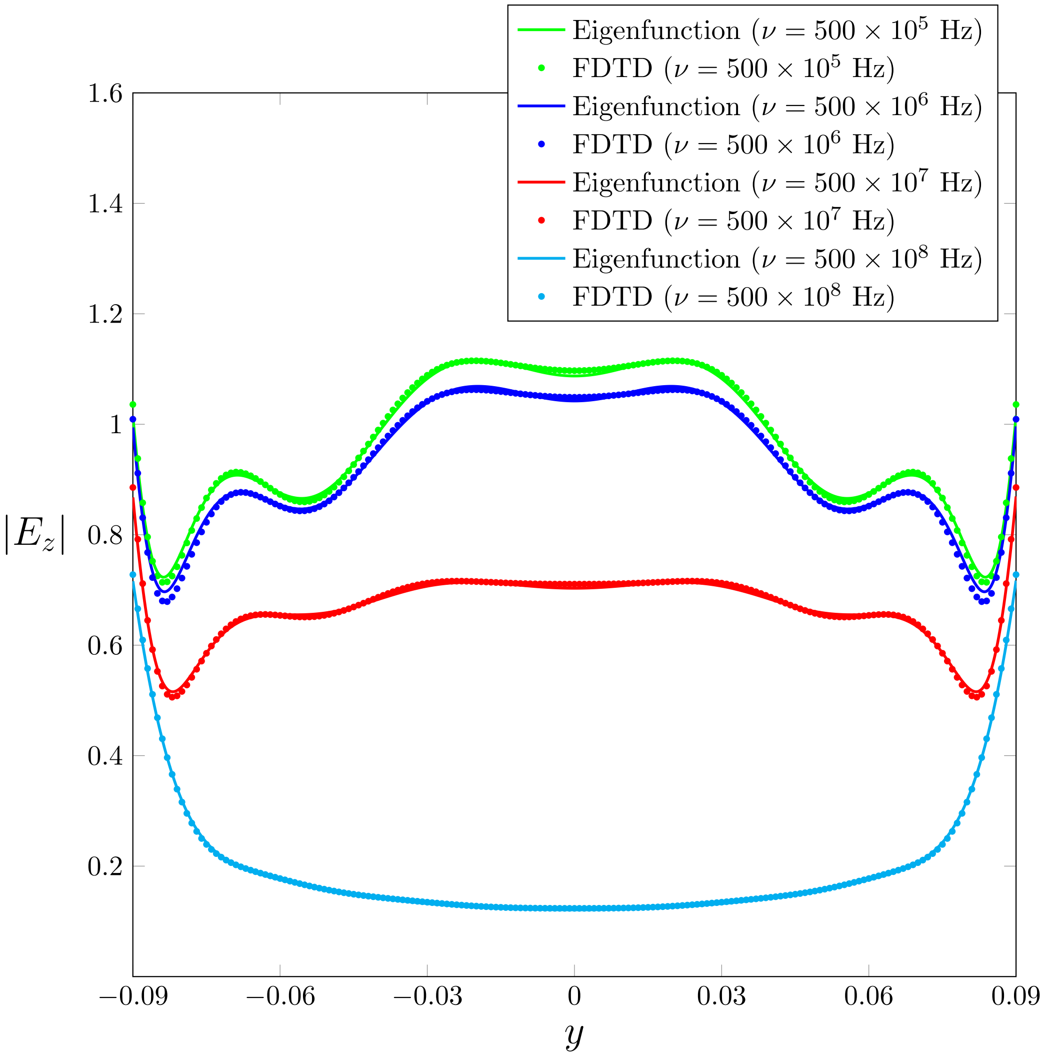

Figure 5.23: Comparison between the absolute electric field, in volts/meter, inside the cylinder for different values of $y$ and for $x = 0$ obtained by the eigenfunction method and the FDTD simulation for different collision frequencies; parameters are otherwise given by table 5.2.

## 5.3
## Inhomogeneous Plasma Cylinder

Now, an inhomogeneous plasma cylinder is investigated. The plasma density parameter is characterized by a central density $n_0$, and the profile follows the quadratic function

$$n(\rho) = n_0 \left(1 - \left(\frac{\rho}{r}\right)^2\right), \tag{5-2}$$

where $r$ is the plasma cylinder radius, shown in figure 5.24. This density profile is more realistic for confined plasmas arising from gas discharges [40].

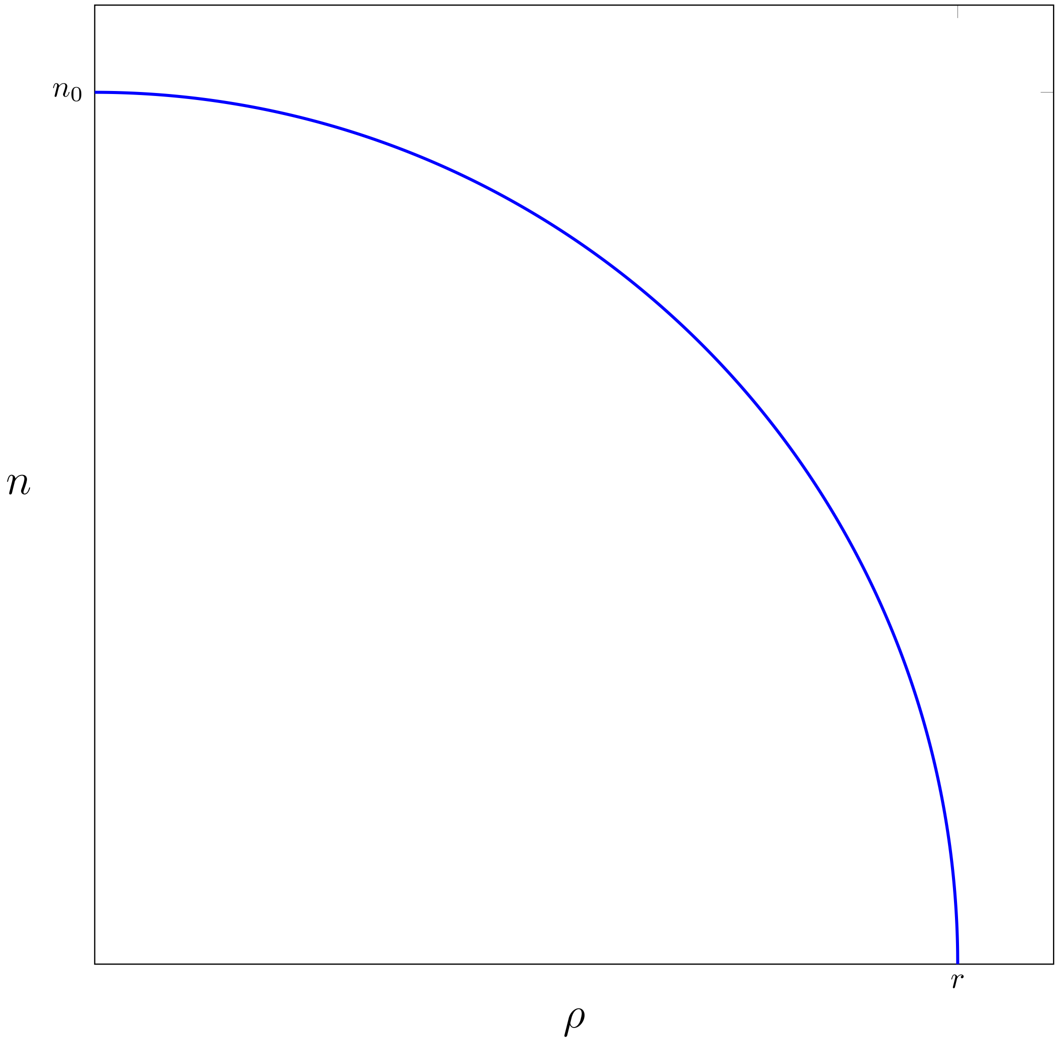

Figure 5.24: Quadradic inhomogeneous density profile under consideration.

The case described by table 5.2 is again used as a baseline case, but with the inhomogeneous profile shown in figure 5.24 instead of an homogeneous density.

The method described in chapter 3 is used to divide the inhomogeneous cylinder into $p$ different concentric shells. Figure 5.25 shows a comparison between the results for the scattering amplitude obtained by the analytical method for different values of $p$. As expected, as $p$ increases the results of the multi-layer approximation converge to a function which can be assumed to be the exact inhomogeneous solution.

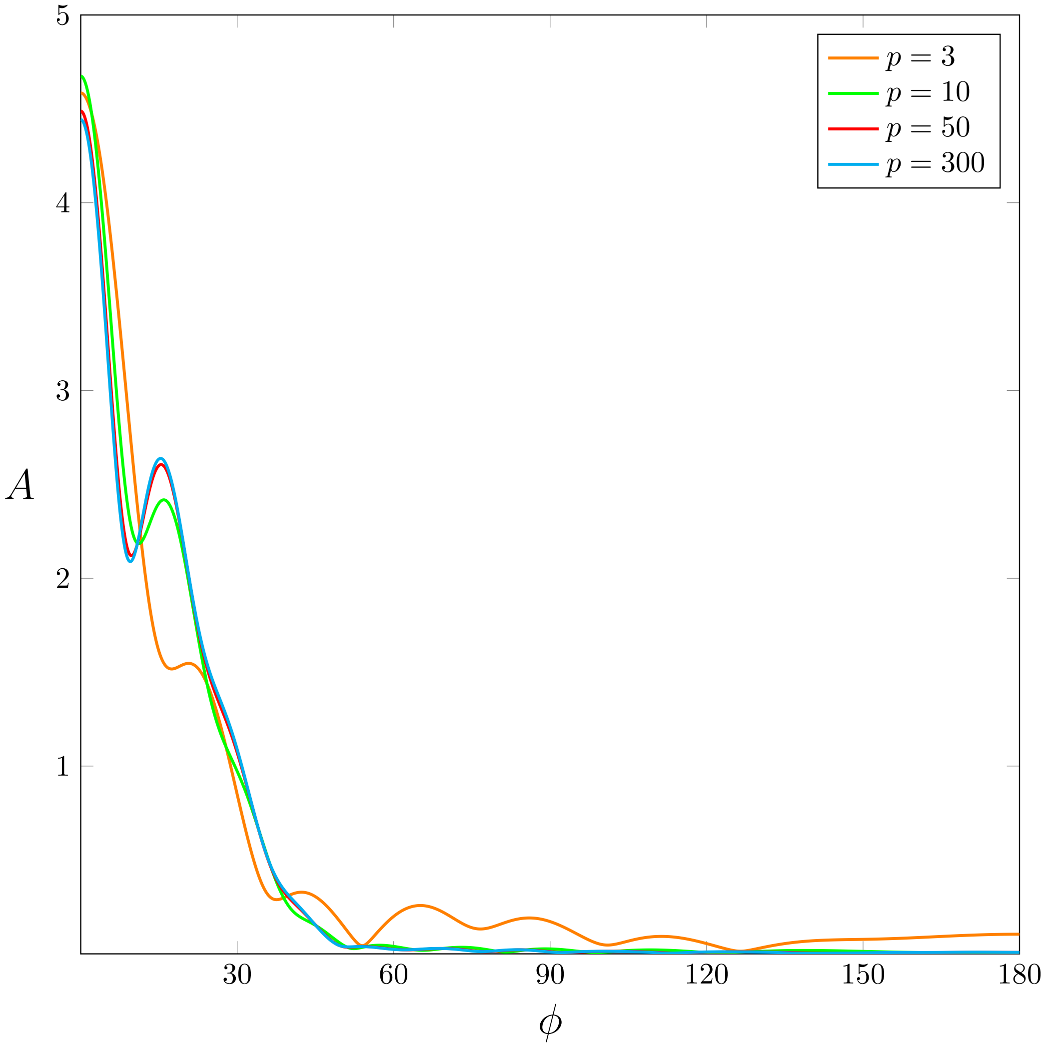

Figure 5.25: Comparison between the results for the scattering amplitude obtained by the analytical eigenfunction method, with different values of the number of concentric shells $p$ used in the algorithm, for the baseline inhomogeneous plasma cylinder problem.

Figure 5.26 shows a comparison between the magnitude of the electric field within the inhomogeneous plasma cylinder under investigation obtained by the analytical method for different values of the number of layers $p$. It can also be seen that as the number of concentric shells used in the algorithm increases, the result converges to a pattern that can be assumed to be the exact inhomogeneous solution. However, the computational cost of running the full algorithm for the internal fields is too prohibitive at such high values of $p$; values as low as 10 already lead to several hours being required for the entire process to finish.

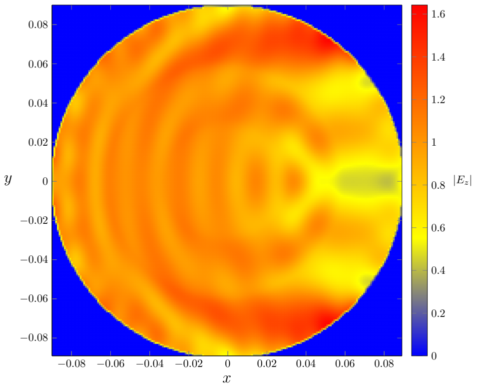

5.26(a): $p = 3$.

5.26(b): $p = 5$.

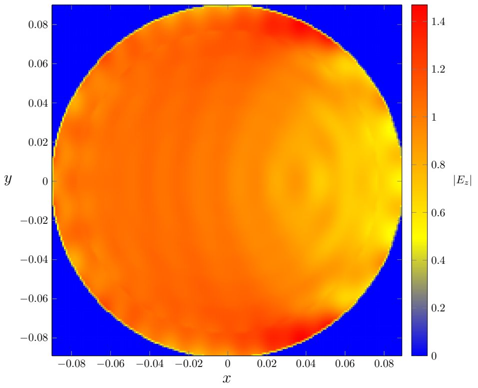

5.26(c): $p = 7$.

5.26(d): $p = 10$.

Figure 5.26: Comparison between the magnitude of the electric field, in volts/meter, within the inhomogeneous plasma cylinder obtained by the analytical method for different values of $p$.

Figure 5.27 shows the time evolution of the electric field within the inhomogeneous plasma cylinder for a few chosen time-steps. Compared to the baseline homogeneous case, there are less internal reflections within the inhomogeneous cylinder, so the simulation does not actually need as many time-steps as before. Conversely, a field-deflecting characteristic of the inhomogeneous cylinder can already be perceived.

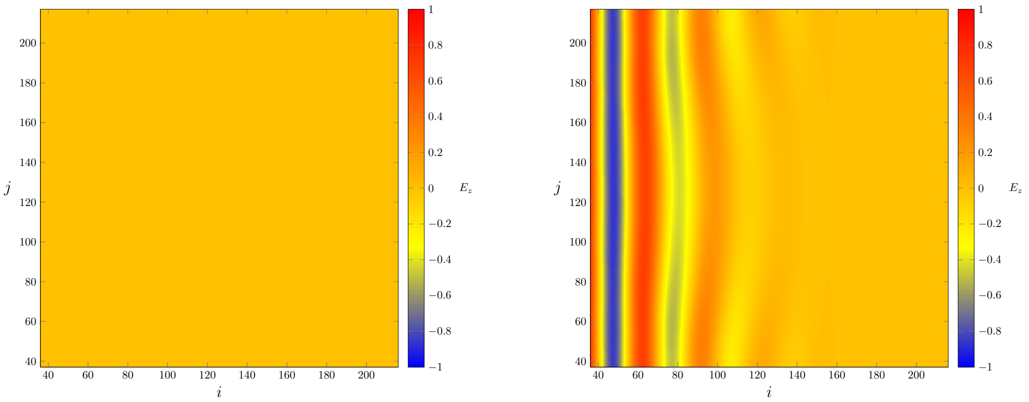

5.27(a): $n = 0$.
5.27(b): $n = 200$.

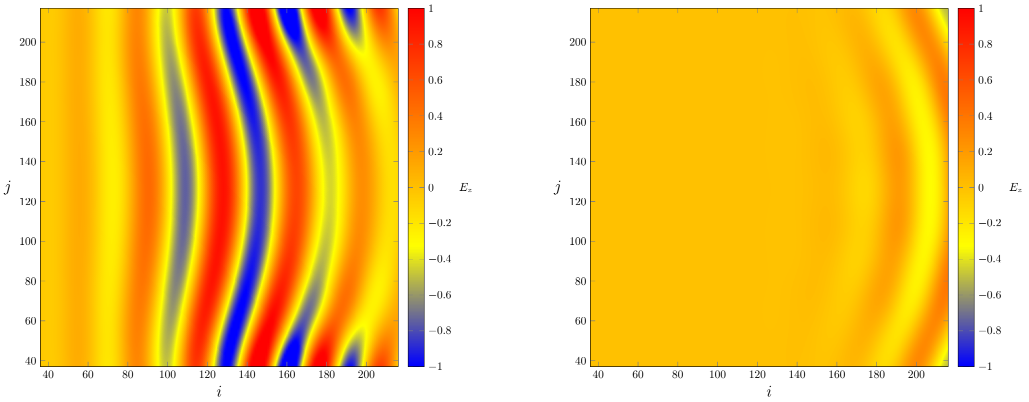

5.27(c): $n = 400$.
5.27(d): $n = 600$.

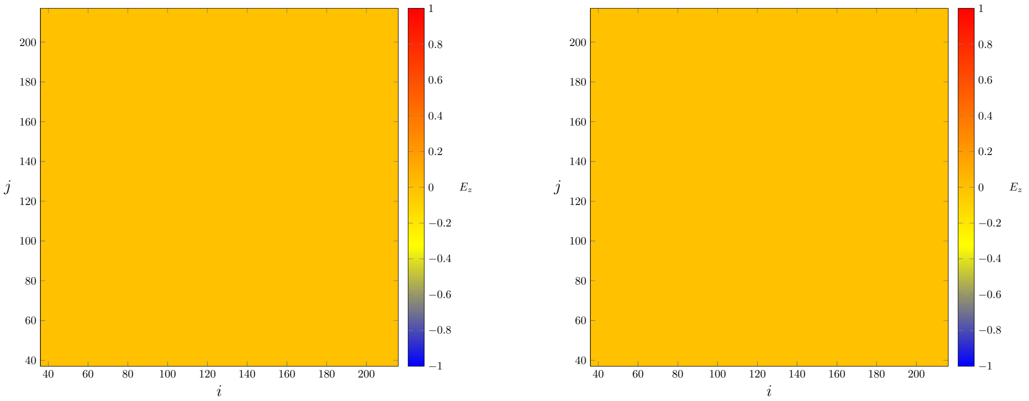

5.27(e): $n = 800$.
5.27(f): $n = 1000$.

Figure 5.27: Time evolution of the numerical solution, in volts/meter, for the baseline inhomogeneous plasma cylinder problem.

The FDTD simulations are now tested against the aforementioned analytical solutions. Whenever not explicitly stated otherwise, following results for the eigenfunction method applied to inhomogeneous plasma cylinders were obtained using $p = 500$. Figure 5.28 shows the comparison between results for the scattering amplitude obtained by the eigenfunction method and the FDTD simulation for the baseline inhomogeneous plasma cylinder problem; excellent agreement is found.

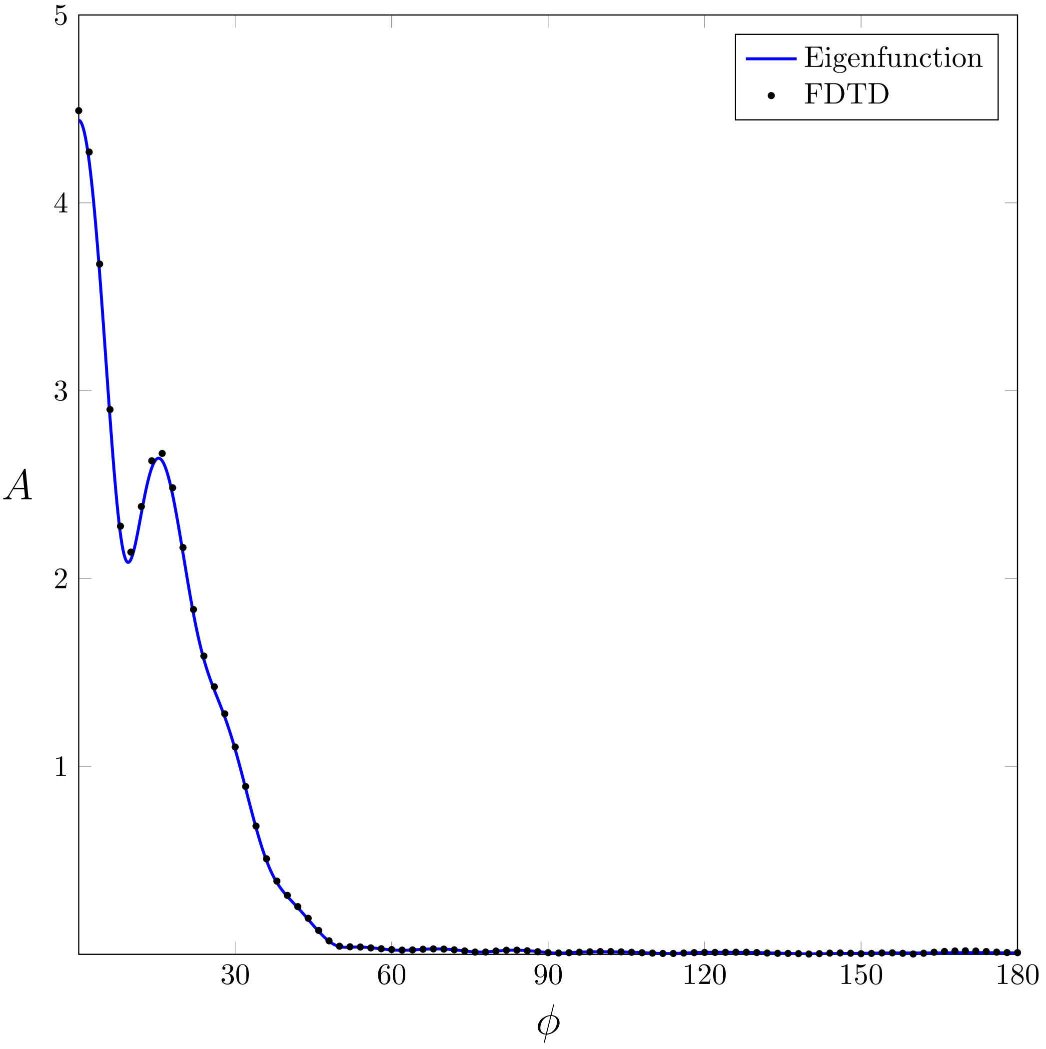

Figure 5.28: Comparison between the results for the scattering amplitude obtained by the eigenfunction method and the FDTD simulation for the baseline inhomogeneous plasma cylinder problem.

Figure 5.29 shows a comparison between the magnitude of the electric field within the inhomogeneous plasma cylinder obtained by the eigenfunction method, with $p = 10$, and the FDTD simulation. Due to the previously-mentioned computational cost of running the full algorithm, the analytical solution for the internal fields is of limited usefulness in the inhomogeneous case, but nevertheless it can be observed that the behaviour of the two solutions is similar, thus validating the numerical method.

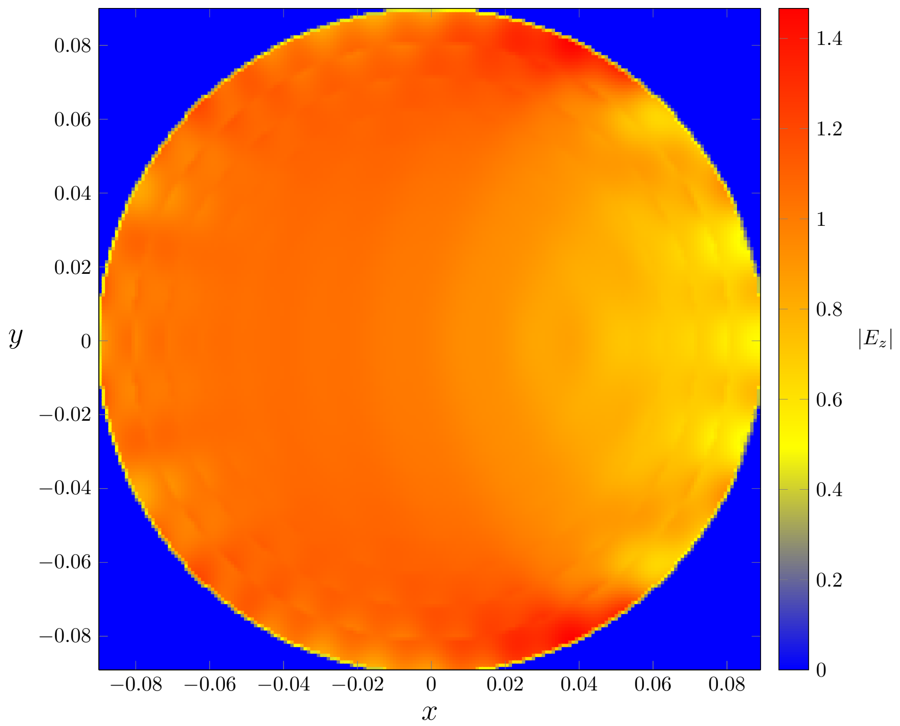

5.29(a): Eigenfunction method, $p = 10$.

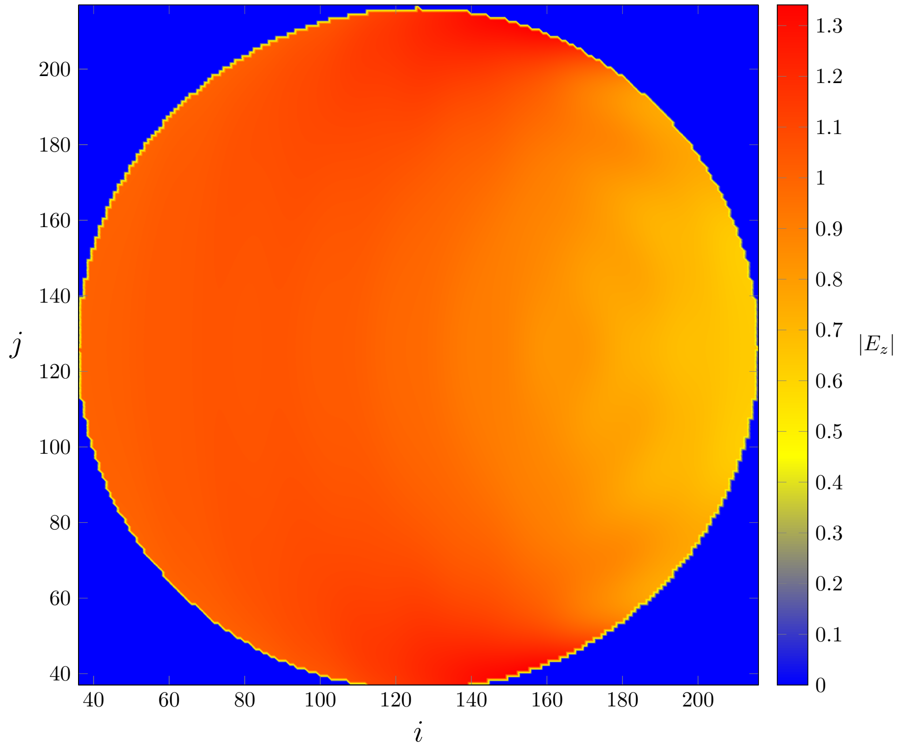

5.29(b): FDTD simulation.

Figure 5.29: Comparison between the magnitude of the electric field, in volts/meter, within the inhomogeneous plasma cylinder obtained by the eigenfunction method and the FDTD simulation for the baseline problem under consideration.

### 5.3.1
### Incident Wave Frequency Effects

The influence of the incident wave frequency is now investigated. Again, the incident wave function retains its form, but the parameter $\tau$ is adjusted so that at least one full period of the sine wave is completed within the Gaussian window to avoid numerical errors in the Fourier Transforms employed in the algorithm.

Figure 5.30 shows a comparison between the scattering amplitudes obtained by the eigenfunction method and the FDTD simulation for different incident frequencies for the inhomogeneous plasma cylinder. Excellent agreement between the analytical method and the simulations is found for all frequencies.

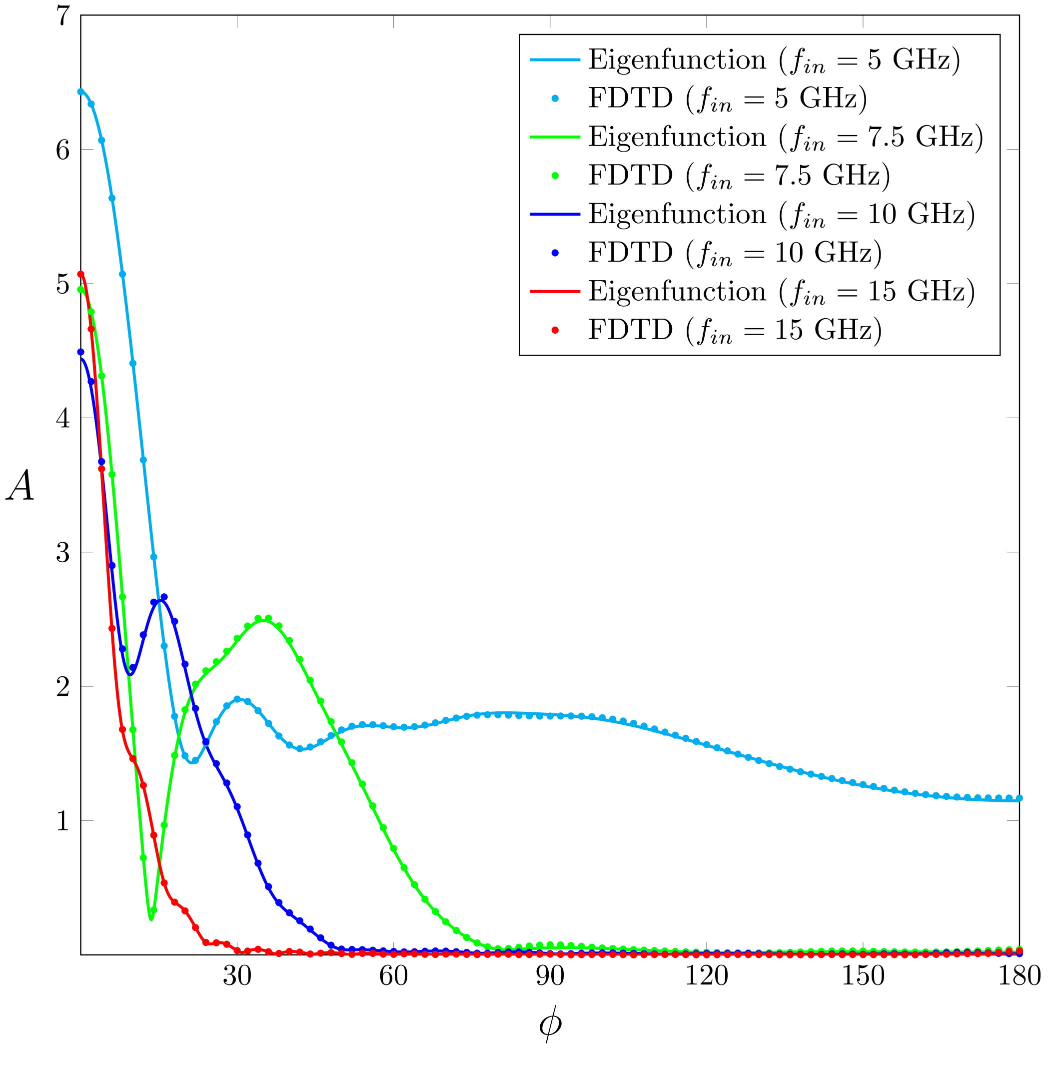

Figure 5.30: Comparison between the scattering amplitudes obtained by the eigenfunction method and the FDTD simulation for different incident frequencies for the inhomogeneous plasma problem.

Figure 5.31 shows a side-by-side comparison of colour-coded two-dimensional plots for the magnitude of the electric field inside the cylinder obtained by FDTD simulations for different values of incident frequencies. It can be observed that for an incident frequency of 15 GHz, the inhomogeneous plasma cylinder is virtually transparent to the electromagnetic wave, even more so than in the homogeneous case.

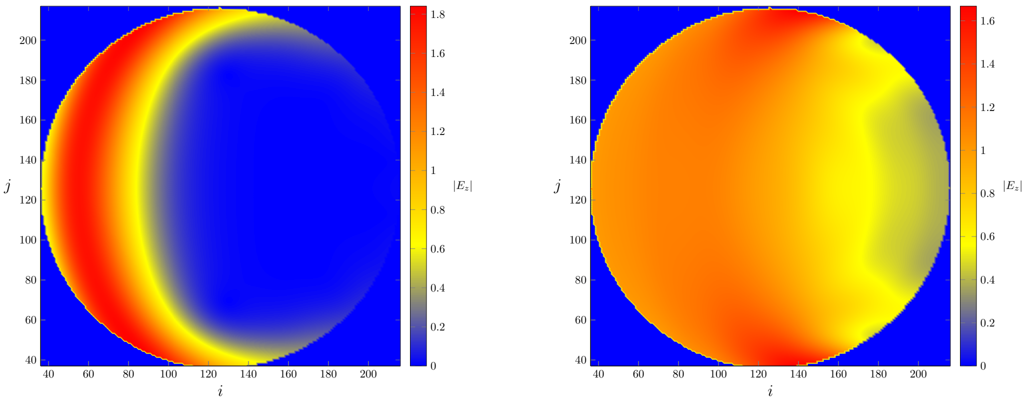

5.31(a): $f_{in} = 5$ GHz. 5.31(b): $f_{in} = 7.5$ GHz.

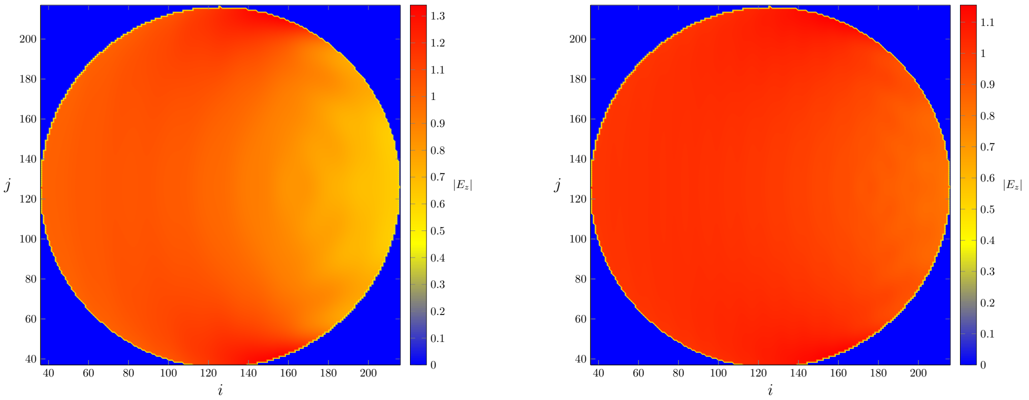

5.31(c): $f_{in} = 10$ GHz. 5.31(d): $f_{in} = 15$ GHz.

Figure 5.31: Comparison between the magnitude of the electric field, in volts/meter, within the inhomogeneous plasma cylinder obtained by the FDTD simulation for different incident frequencies.

To analyse in more detail the behaviour within the inhomogeneous cylinder, figures 5.32 and 5.33 show linear plots of the magnitude of the electric field inside the cylinder for $y = 0$ and $x = 0$ cuts, respectively, for the different incident wave frequencies under consideration. Analytical results from the eigenfunction method are not shown due to the previously-mentioned computational cost difficulties in running the full algorithm and obtaining a result that has converged to the exact solution.

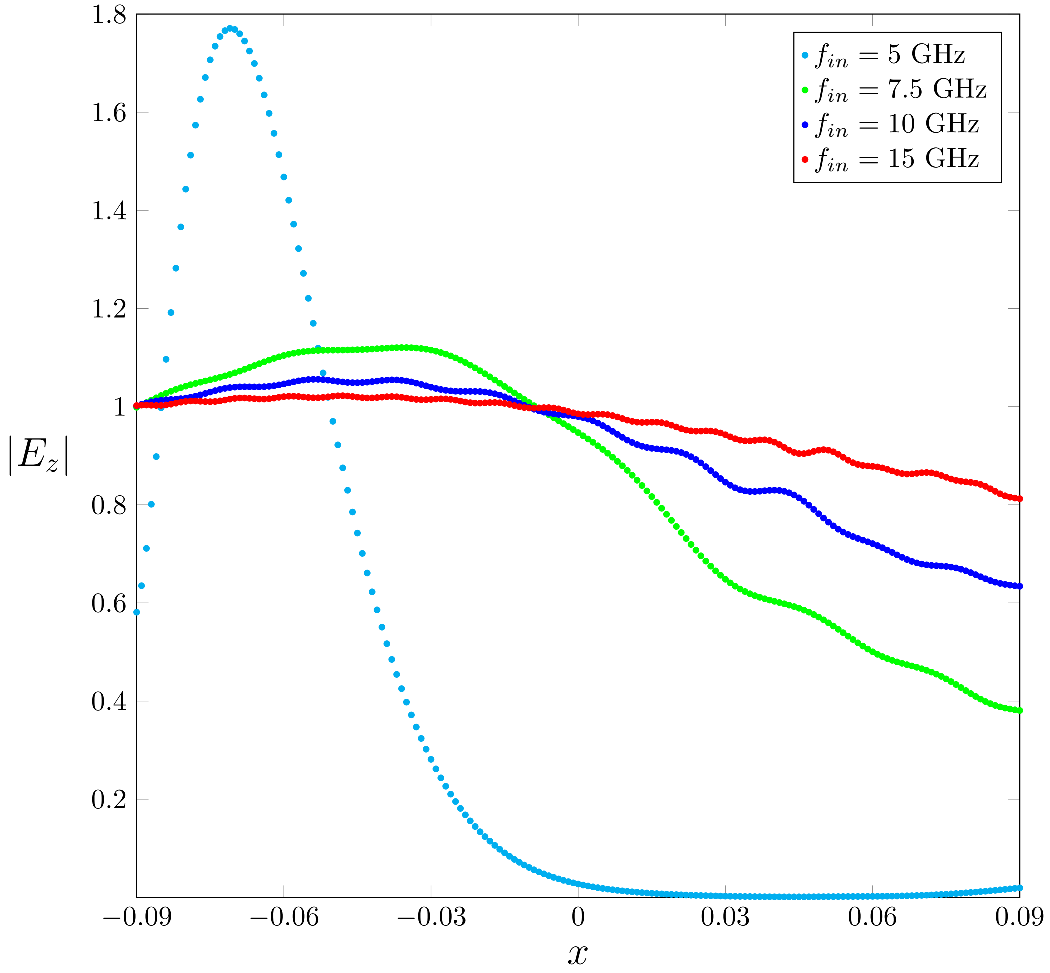

Figure 5.32: Comparison between the absolute electric field, in volts/meter, inside the cylinder for different values of $x$ and for $y = 0$ obtained by FDTD simulation for different collision frequencies.

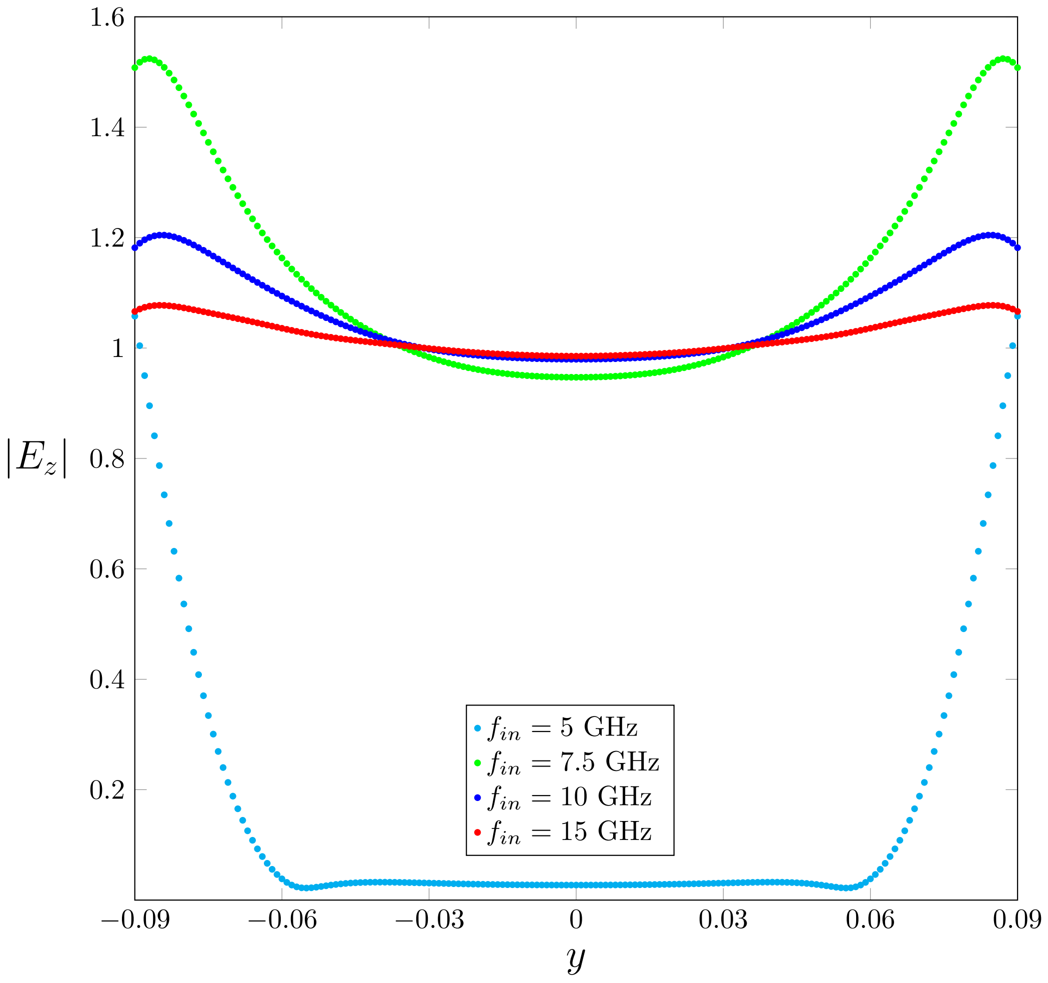

Figure 5.33: Comparison between the absolute electric field, in volts/meter, inside the cylinder for different values of $y$ and for $x = 0$ obtained by FDTD simulation for different collision frequencies.

### 5.3.2
### Central Plasma Density Effects

The influence of the central value for the plasma's inhomogeneous electron density is now investigated. Like before, other parameters are kept equal to those in table 5.2, but the central plasma density and maximum temporal step are changed.

Figure 5.34 shows a comparison between the scattering amplitudes obtained by the eigenfunction method and the FDTD simulation for different central plasma densities. Excelent agreement between the analytical method and the simulations is found for all central densities.

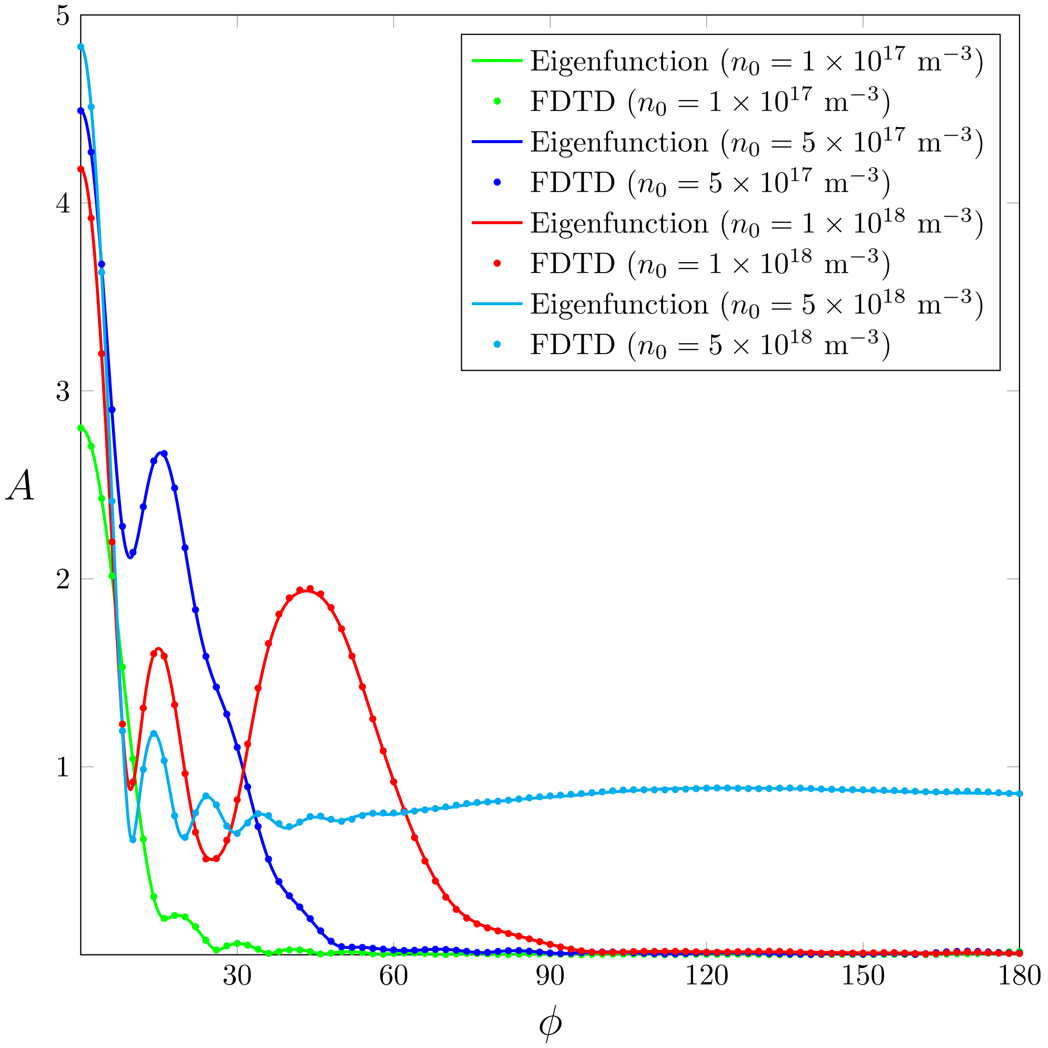

Figure 5.34: Comparison between the scattering amplitudes obtained by the eigenfunction method and the FDTD simulation for different central inhomogeneous plasma densities.

Figure 5.35 shows a side-by-side comparison of colour-coded two-dimensional plots for the magnitude of the electric field inside the cylinder obtained by FDTD simulations for different values of the central plasma density. It can be observed that, for the central density of $1 \times 10^{17}$ m$^{-3}$, the inhomogeneous plasma cylinder is virtually transparent to the electromagnetic wave, and for $n_0 = 5 \times 10^{18}$ m$^{-3}$, the electromagnetic wave has difficulties penetrating the cylinder.

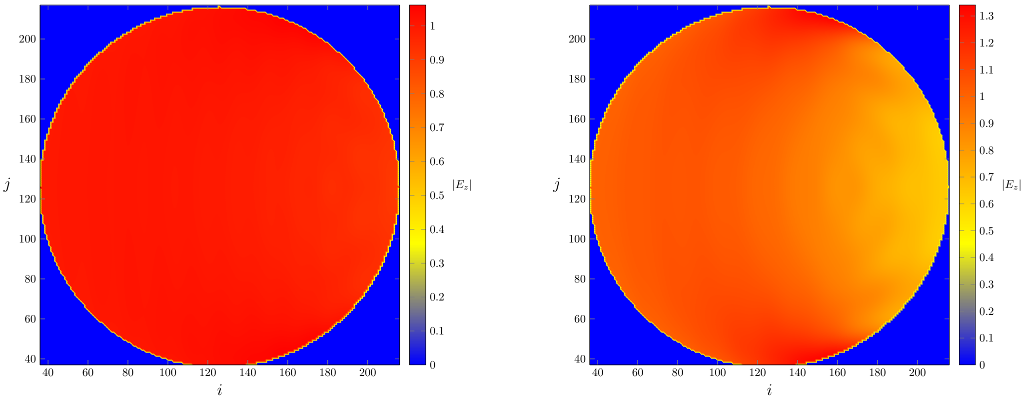

5.35(a): $n_0 = 1 \times 10^{17}$ m$^{-3}$.

5.35(b): $n_0 = 5 \times 10^{17}$ m$^{-3}$.

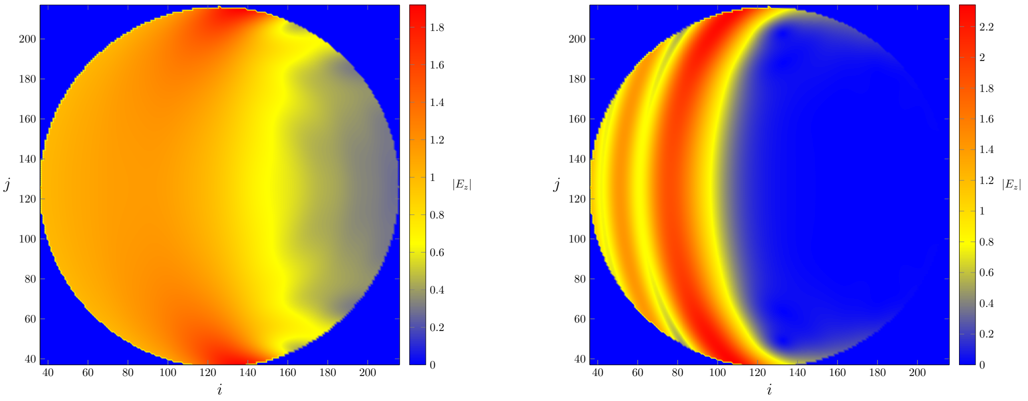

5.35(c): $n_0 = 1 \times 10^{18}$ m$^{-3}$.

5.35(d): $n_0 = 1.5 \times 10^{18}$ m$^{-3}$.

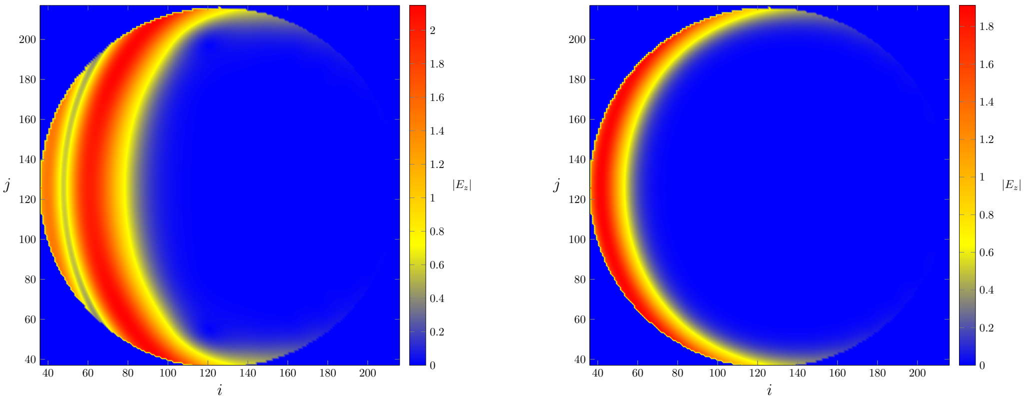

5.35(e): $n_0 = 2 \times 10^{18}$ m$^{-3}$.

5.35(f): $n_0 = 5 \times 10^{18}$ m$^{-3}$.

Figure 5.35: Comparison between the magnitude of the electric field, in volts/meter, within the inhomogeneous plasma cylinder obtained by the FDTD simulation for different central plasma densities.

To analyse in more detail the behaviour within the inhomogeneous cylinder, figures 5.36 and 5.37 show linear plots of the magnitude of the electric field inside the cylinder for $y = 0$ and $x = 0$ cuts, respectively, for the different central densities under consideration. As before, analytical results from the eigenfunction method are not shown due to the previously-mentioned computational cost difficulties in running the full algorithm and obtaining a result that has converged to the exact solution. The results for the $n_0 = 5\times10^{18}$ $\mathrm{m}^{-3}$ case are not shown to avoid cluttering the graphs.

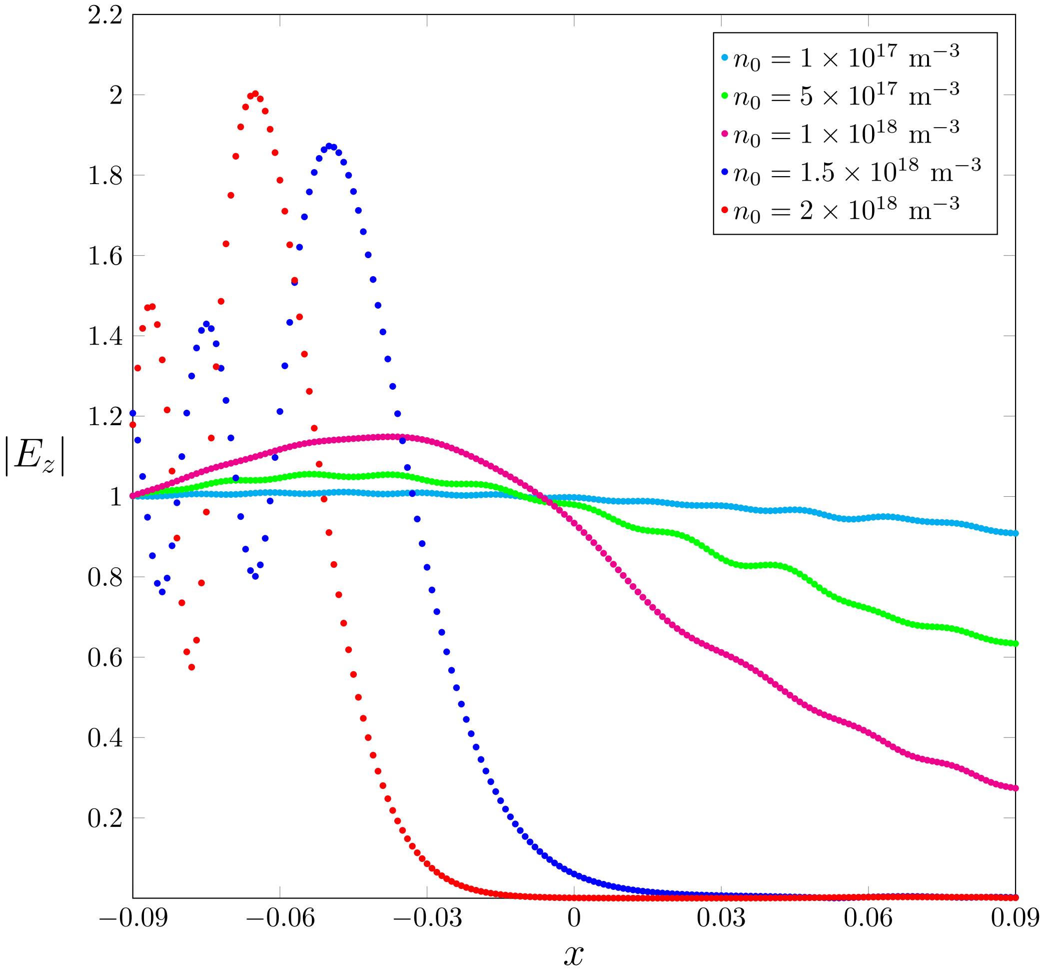

Figure 5.36: Comparison between the absolute electric field, in volts/meter, inside the cylinder for different values of $x$ and for $y = 0$ obtained by FDTD simulation for different central plasma densities.

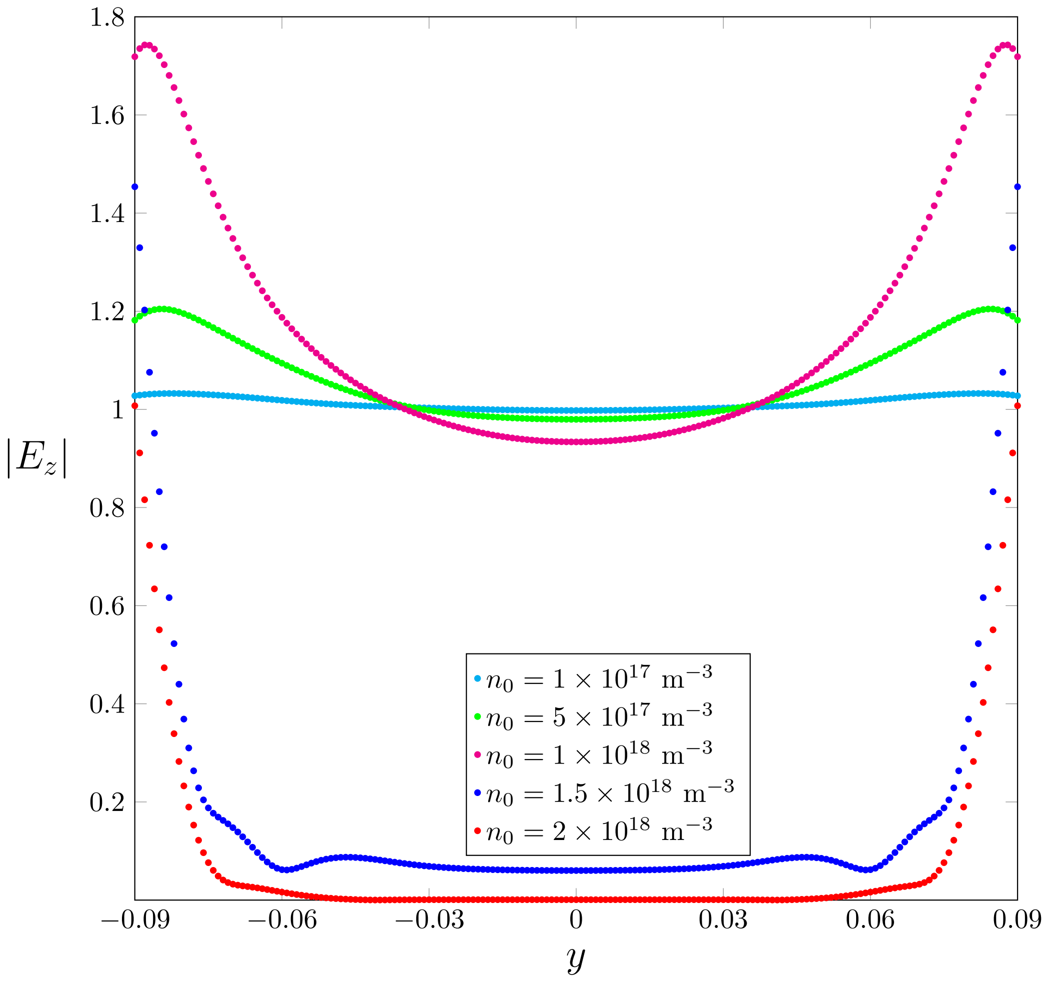

Figure 5.37: Comparison between the absolute electric field, in volts/meter, inside the cylinder for different values of $y$ and for $x = 0$ obtained by FDTD simulation for different central plasma densities.

### 5.3.3
### Plasma Collision Frequency Effects

The influence of the plasma's collision frequency is now investigated. Like before, other parameters are kept equal to those in table 5.2, but collision frequency and maximum temporal step are changed.

Figure 5.38 shows a comparison between the scattering amplitudes obtained by the eigenfunction method and the FDTD simulation for different collision frequencies. Good agreement between the analytical method and the simulations is found for all collision frequencies.

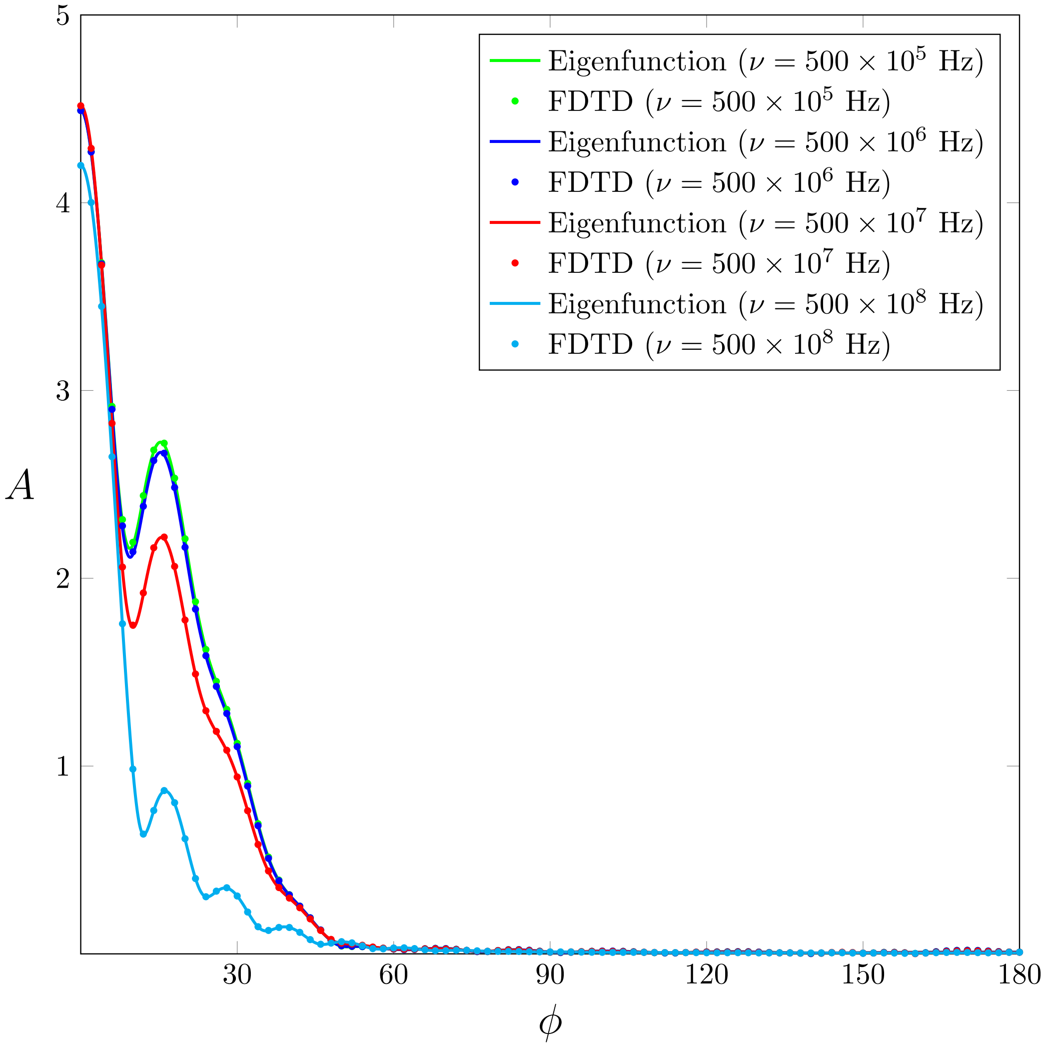

Figure 5.38: Comparison between the scattering amplitudes obtained by the eigenfunction method and the FDTD simulation for different collision frequencies. For $\nu = 500 \times 10^5$ Hz, in green, the results are almost identical to the baseline case, in blue, so the curves lie on top of each other.

Figure 5.39 shows a side-by-side comparison of colour-coded two-dimensional plots for the magnitude of the electric field inside the cylinder obtained by FDTD simulations for different values of the electron collision frequency. It can be observed that for the collision frequency of $500 \times 10^5$ Hz the results are virtually identical to the baseline case.

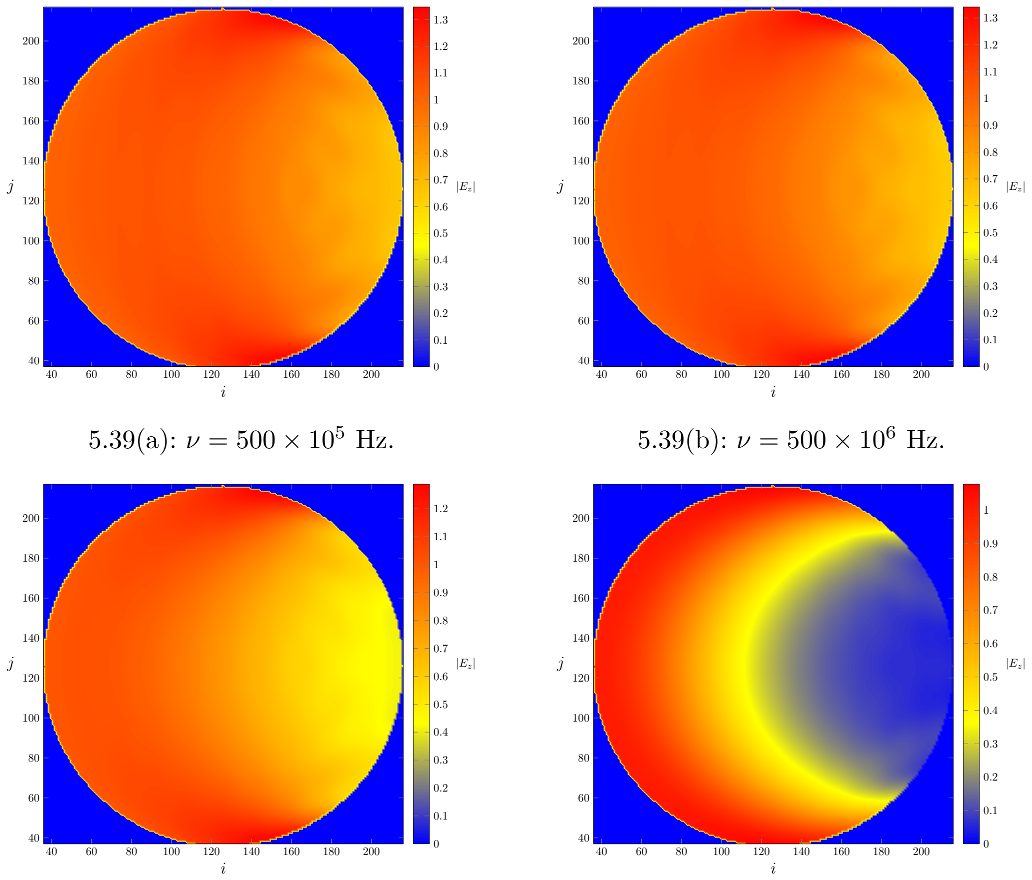

5.39(a): $\nu = 500 \times 10^5$ Hz.

5.39(b): $\nu = 500 \times 10^6$ Hz.

5.39(c): $\nu = 500 \times 10^7$ Hz.

5.39(d): $\nu = 500 \times 10^8$ Hz.

Figure 5.39: Comparison between the magnitude of the electric field, in volts/meter, within the inhomogeneous plasma cylinder obtained by the FDTD simulation for different electron collision frequencies.

To analyse in more detail the behaviour within the inhomogeneous cylinder, figures 5.40 and 5.41 show linear plots of the magnitude of the electric field inside the cylinder for $y = 0$ and $x = 0$ cuts, respectively, for the different collision frequencies under consideration. As before, analytical results from the eigenfunction method are not shown due to the previously-mentioned computational cost difficulties in running the full algorithm and obtaining a result that has converged to the exact solution.

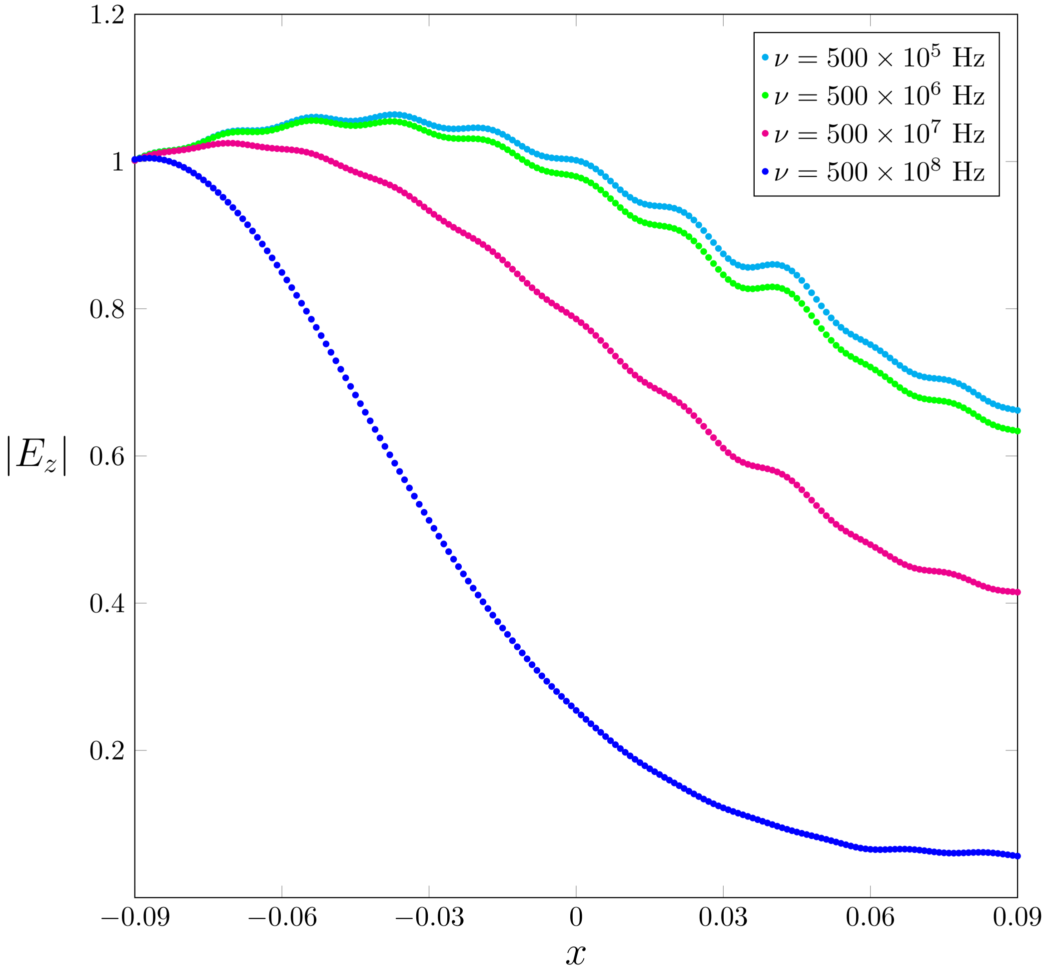

Figure 5.40: Comparison between the absolute electric field, in volts/meter, inside the cylinder for different values of $x$ and for $y = 0$ obtained by FDTD simulation for different electron collision frequencies.

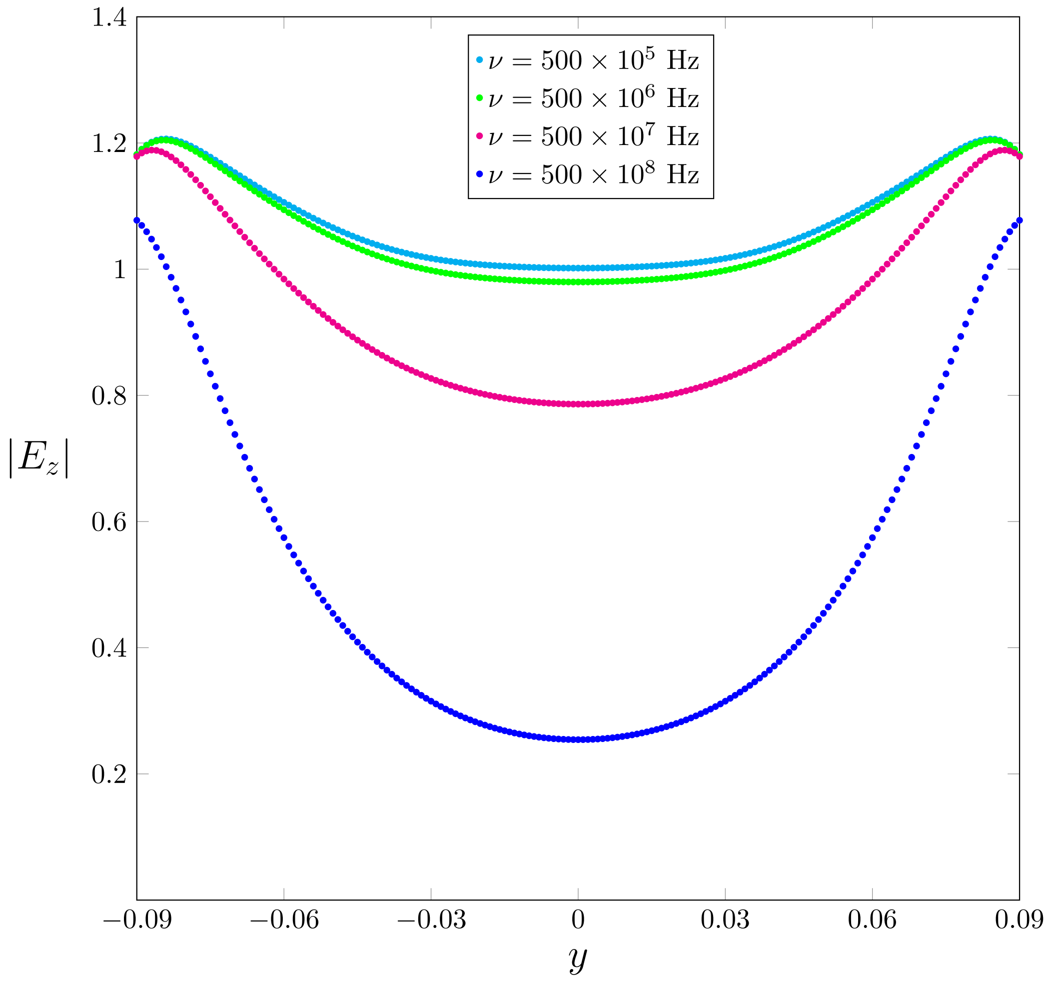

Figure 5.41: Comparison between the absolute electric field, in volts/meter, inside the cylinder for different values of $y$ and for $x = 0$ obtained by FDTD simulation for different electron collision frequencies.

## 5.4
## Discussion

The results shown in the previous sections can be analysed according to the expression of the dielectric permittivity for the plasma given by eq. (2-41), repeated here for convenience,

$$\epsilon_r = 1 - \frac{\omega_p^2}{\omega^2 - i\omega\nu}. \tag{2-41}$$

For the homogeneous results, or locally for the inhomogeneous case, one qualitative analysis is straightforward: as expected from inspecting eq. (2-41), variations in the plasma frequency $\omega_p$ (which depends on the plasma density) change the behaviour of electromagnetic propagation inversely to variations in both wave frequency $\omega$ and electron collision frequency $\nu$. This effect can be seen e.g. by comparing the homogeneous results for $f_{in} = 5$ GHz, figures 5.12(a) and 5.12(b), with the homogeneous results for $n_0 = 5 \times 10^{18}$ m$^{-3}$, figures 5.17(e) and 5.17(f).

Additionally, for the inhomogeneous cases only, another qualitative analysis of the results shows a phenomenon of wave path deflection that was not present in the homogeneous case. This is due to the spatial variation in the electron density, which in turn causes a spatial variation in the refraction index of the plasma medium. Continuous spatial variations in refraction indexes, in turn, are well-known to cause ray deflection.

In broad terms, two different behaviours can be observed from the presented results: 1) electromagnetic waves penetrating the plasma and propagating while being conditioned by the plasma, i.e., suffering dispersion, attenuation and deflection, when appropriate to each situation's characteristics, and 2) electromagnetic waves being reflected from the plasma and exhibiting very low penetration (or, for the inhomogeneous cases, very low penetration after a certain point in the inhomogeneous cylinder).

These two different types of behaviour are related to the real part of the plasma's dielectric permittivity, with penetration possible for $\text{Re}(\epsilon_r) > 0$ and reflection occurring for $\text{Re}(\epsilon_r) < 0$. The same kind of behaviour is exhibited by e.g. noble metals, which are reflective at infra-red and optical frequencies but transparent to higher-frequency waves [22]. This effect can be seen e.g. by comparing the inhomogeneous solutions for different central plasma densities, figure 5.35; visually, there seems to be a shift in behaviour between $n_0 = 1 \times 10^{18}$ m$^{-3}$ and $n_0 = 1.5 \times 10^{18}$ m$^{-3}$. Figure 5.42 shows the real part of the dielectric permittivity as a function of the local electron density $n$ for this range of densities, and the turning point from positive to negative permittivity can be clearly seen. Equating the permittivity to zero, the approximate value for the density in which the turning point happens is given by $n_{turn} \approx 1.24254 \times 10^{18}$ m$^{-3}$.

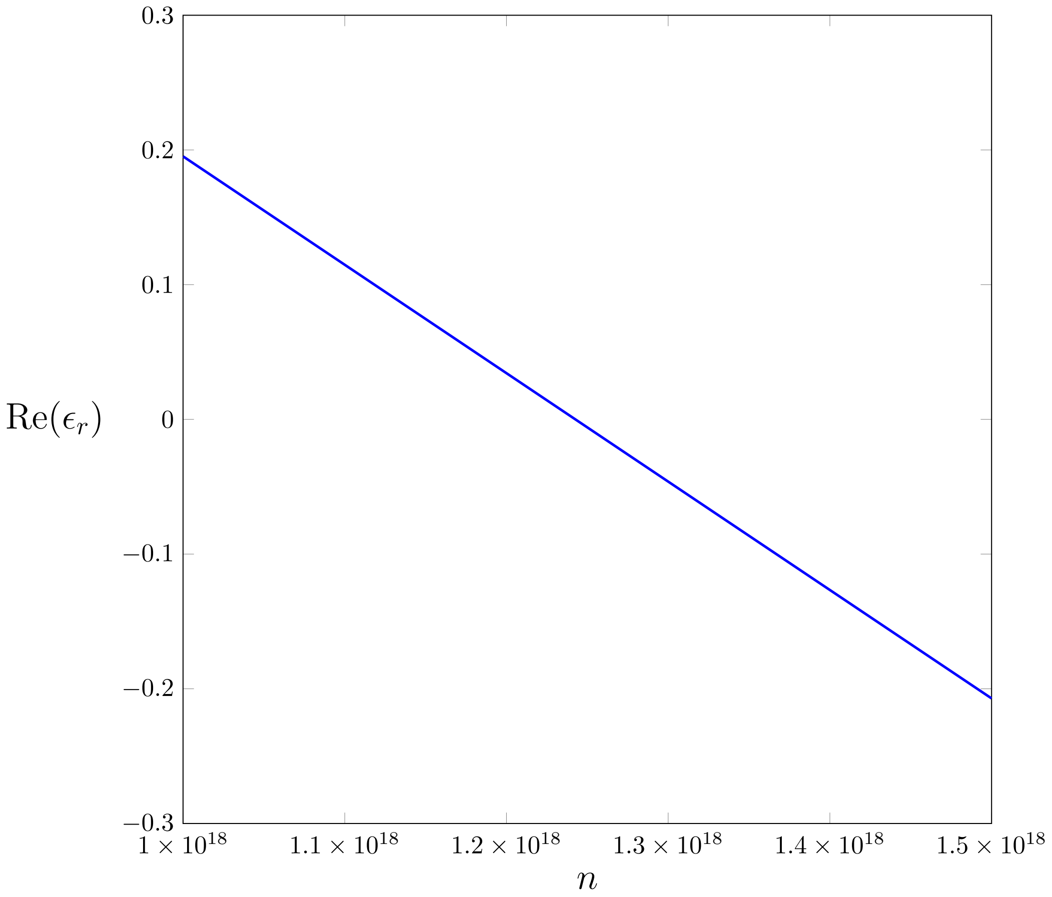

Figure 5.42: Real part of the plasma dielectric permittivity $\epsilon_r$ as a function of the local electron density $n$, for the parameters studied in the FDTD results.

It is worth noting, however, that for the cases where the variation of the electron collision frequency $\nu$ was investigated, the values of the other parameters created the restriction $\mathrm{Re}(\epsilon_r) > 0 \ \forall \ \nu > 0$, so the field extinction was solely a result of the dissipative term introduced by the collision frequency $\nu$. The real part of the plasma dielectric permittivity as a function of the electron collision frequency, for the parameters used in the numerical results, is shown in figure 5.43.

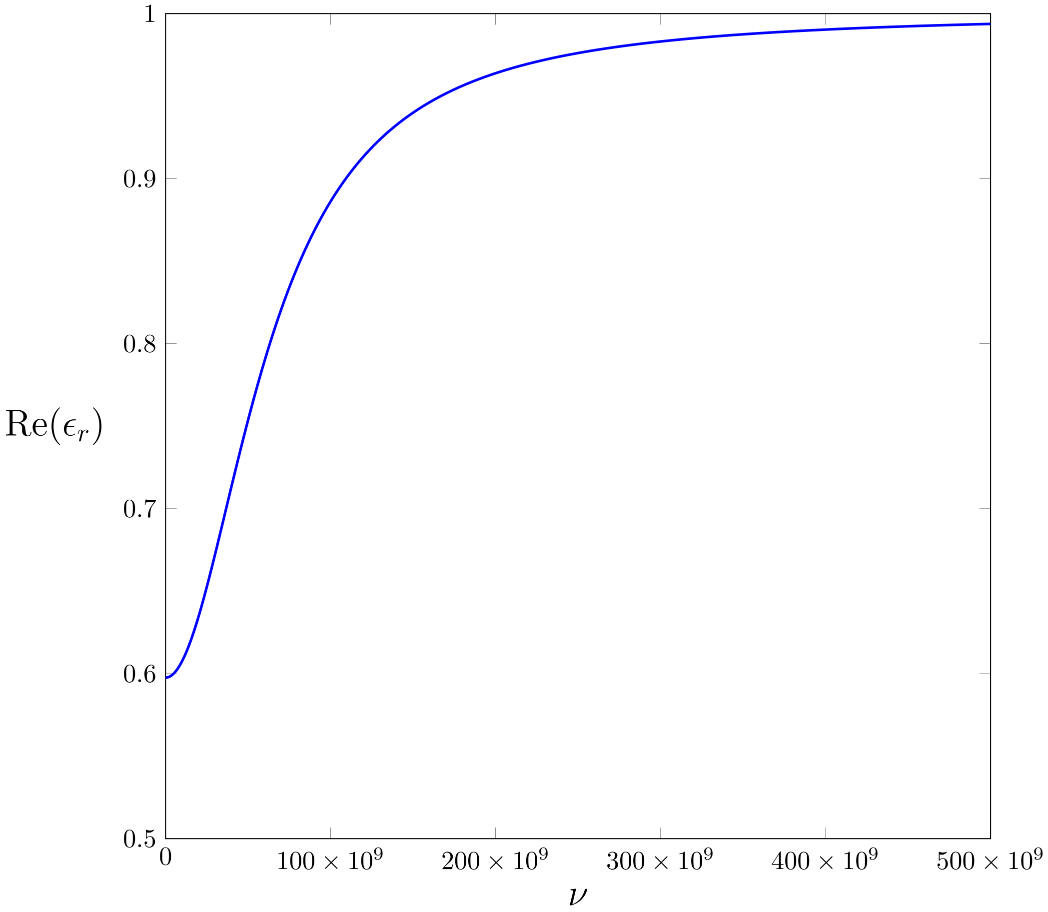

Figure 5.43: Real part of the plasma dielectric permittivity $\epsilon_r$ as a function of the electron collision frequency $\nu$, for the parameters studied in the FDTD results.

To better visualize the behaviour shift in the plasma dielectric permittivity as a function of the variations in the parameters, figures 5.44, 5.45 and 5.46 provide two-dimensional colour plots in which red regions represent values of $\mathrm{Re}(\epsilon_r) > 0$ and blue regions represent values of $\mathrm{Re}(\epsilon_r) < 0$.

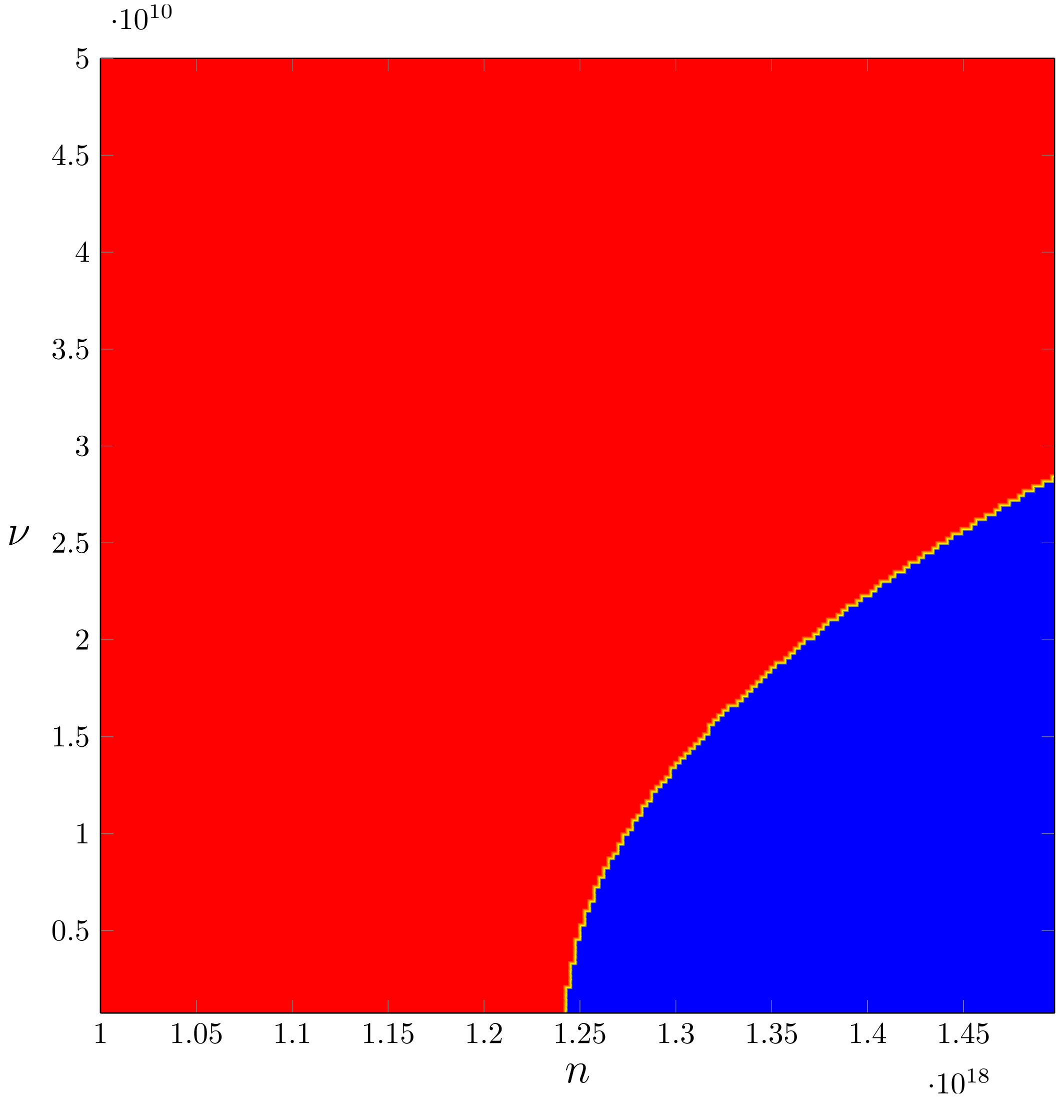

Figure 5.44: Behaviour shift for the plasma dielectric permittivity as a function of the local electron density $n$ and the electron collision frequency $\nu$. Red region represents $\mathrm{Re}(\epsilon_r) > 0$ and blue region represents $\mathrm{Re}(\epsilon_r) < 0$.

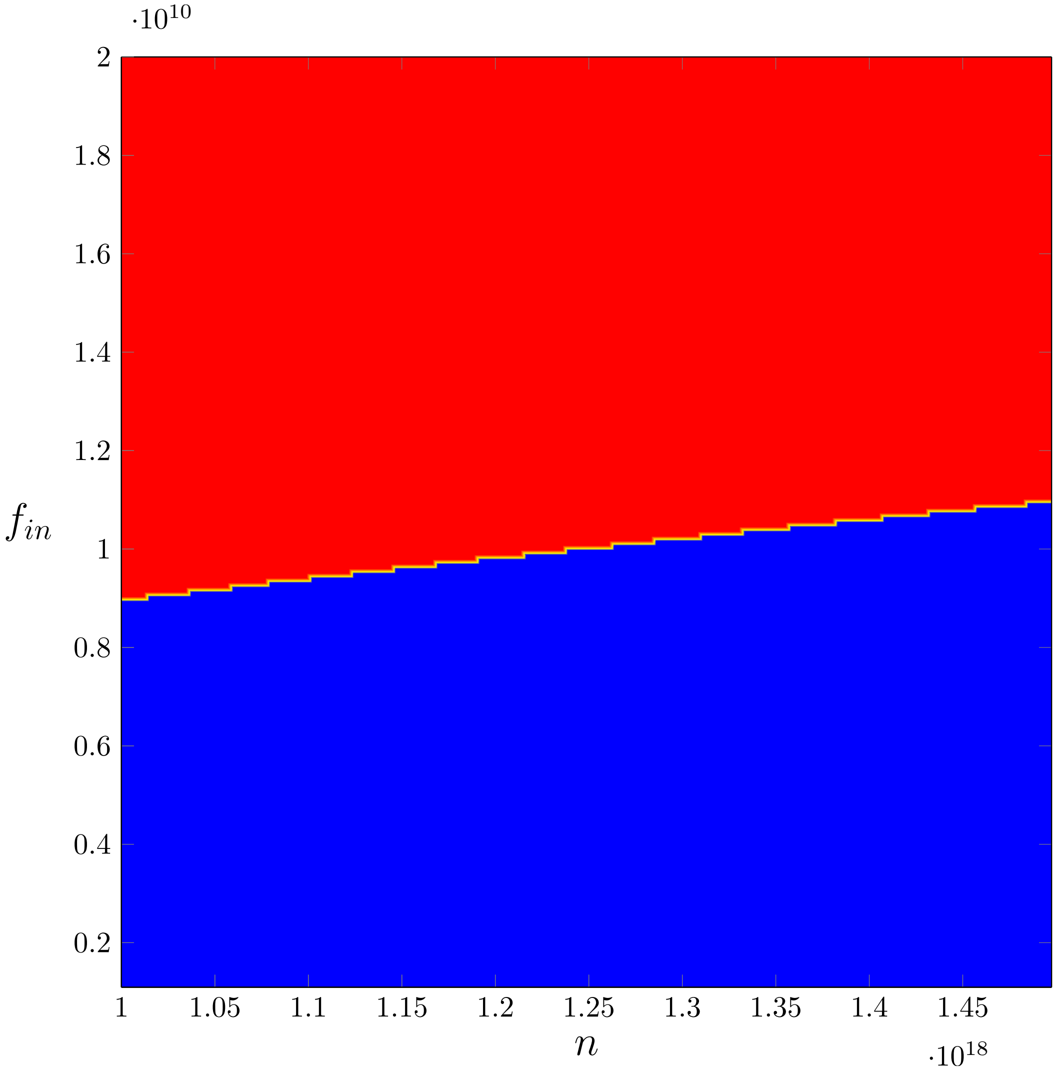

Figure 5.45: Behaviour shift for the plasma dielectric permittivity as a function of the local electron density $n$ and the incident wave frequency $f_{in}$. Red region represents $\mathrm{Re}(\epsilon_r) > 0$ and blue region represents $\mathrm{Re}(\epsilon_r) < 0$.

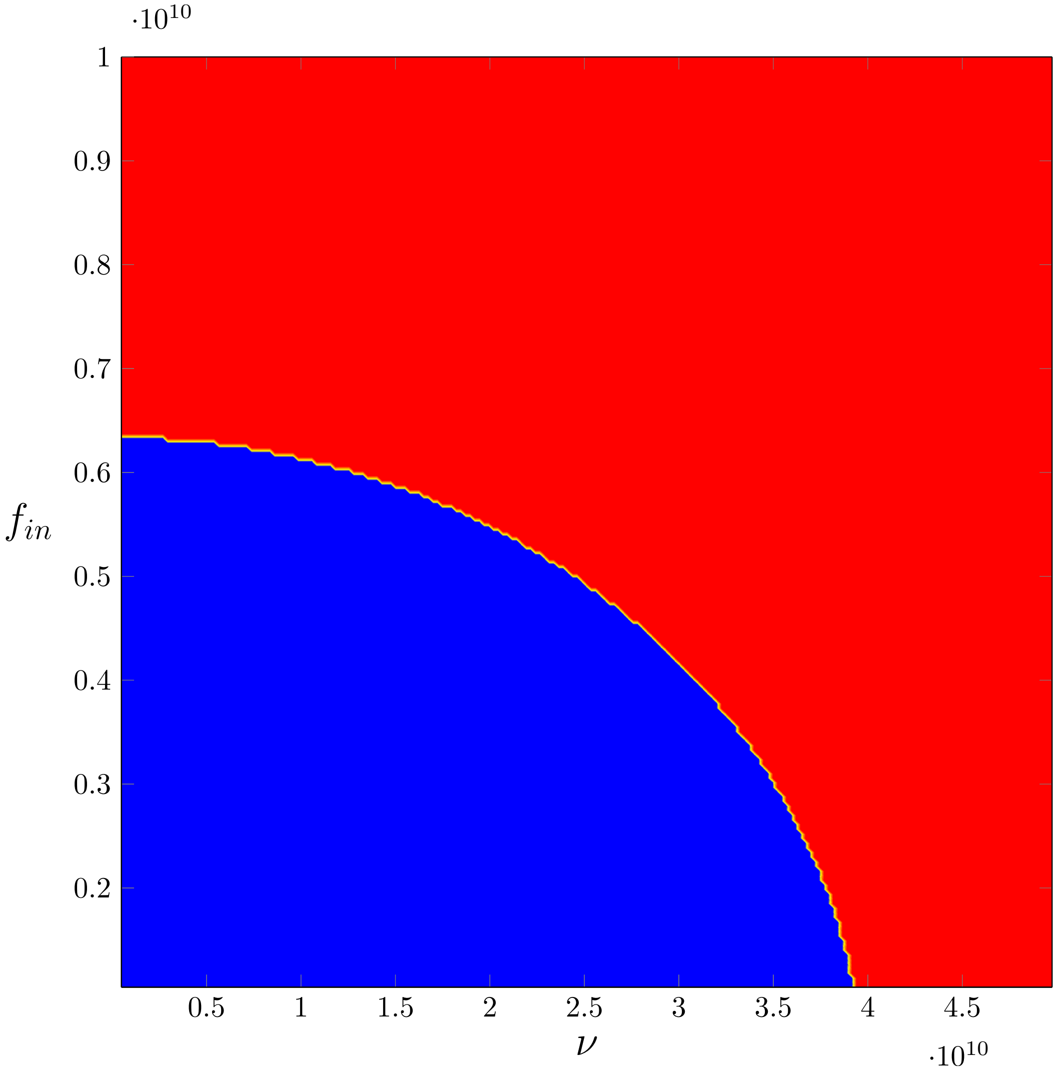

Figure 5.46: Behaviour shift for the plasma dielectric permittivity as a function of the electron collision frequency $\nu$ and the incident wave frequency $f_{in}$. Red region represents $\mathrm{Re}(\epsilon_r) > 0$ and blue region represents $\mathrm{Re}(\epsilon_r) < 0$.

# 6
# Conclusions

A study on the fundamentals of plasma theory was made; the most commonly used results and models were presented along with their derivations as a basis for further study into plasma phenomena related to electromagnetic propagation in radio frequencies and to application for antenna design.

For the study of electromagnetic wave propagation within plasma structures, both analytical and FDTD-based methods were presented. The analytical method consists of a simple expansion of fields into eigenfunctions appropriate to the structure of interest whose coefficients are subsequently found by matching modes across boundaries within the structure. The FDTD-based method expands Yee's seminal algorithm for computational electromagnetics to also account for propagation within the plasma, but otherwise inherits characteristics and methods of usual FDTD simulations.

Validating results were provided for the analytical method via comparison with known results from the literature, ensuring theoretical validity and its correct implementation, thus allowing for the method to be used as a validation tool for the FDTD simulations.

Baseline cases for homogeneous and inhomogeneous plasmas were presented, as well as a number of case studies exploring variations in the parameters of the plasma structure. Excellent agreement was found between the analytical and FDTD methods.

The FDTD simulations were of great value in identifying different behaviours within the plasma structure and exploring the effects of the plasma parameters on the electromagnetic propagation. In particular, for inhomogeneous cases, or any case with other kinds of spatial complexity (e.g. complicated geometries for the structure) the computational cost of running the analytical method was prohibitively high. For simplistic cases, application of either method was equivalent in terms of computational costs, but for complex spatial conditions (e.g. inhomogeneities), the FDTD method showed to be superior in the processing time it took for the solution to be obtained.

Future perspectives for this work include extending the numerical algorithm for a TEz-polarized incident wave. Due to the nature of TMz-polarized waves, the electric field was restricted to having only a $z$-component, which caused the electron flux in the plasma to be solely in the non-simulated axis and therefore ignored. Extending the algorithm to TEz-polarized waves creates the additional complexity of modelling the electron density variation caused by electron fluxes within the computational domain, as well as enforcing boundary conditions for the plasma currents excited within the structure.

Another perspective is including ionization processes in the algorithm, which would allow the simulation of start-up and turn-off of a device; so far, the plasma has been considered to be in a steady state of ionization, i.e. the source responsible for ionization is considered to be active for a long time and recombination processes are ignored.

With these extensions the algorithm would be able to simulate fully self-consistent plasma systems in three spatial dimensions, thus allowing for the full simulation of an entire device like a plasma antenna, or even the interaction between multiple devices operating simultaneously.

# A
# Helmholtz Equation in Cylindrical Coordinates

Starting from the wave equation

$$\left(\frac{\partial^2}{\partial t^2} - c^2\nabla^2\right)\psi(\vec{x},t) = 0, \tag{A-1}$$

separation of variables is assumed so that the wave function can be separated into spatial and temporal functions,

$$\psi(\vec{x},t) = S(\vec{x})T(t), \tag{A-2}$$

which allows equation (A-1) to be rearranged as

$$\frac{\nabla^2 S(\vec{x})}{S(\vec{x})} = \frac{1}{T(t)c^2}\frac{\partial^2}{\partial t^2}T(t). \tag{A-3}$$

Equation (A-3) only has non-trivial solutions in the general case if and only if both sides are equal to a constant value, chosen without loss of generality to be $-k^2$ so that

$$\left(\nabla^2 + k^2\right)S(\vec{x}) = 0, \tag{A-4a}$$

$$\left(\frac{\partial^2}{\partial t^2} + (kc)^2\right)T(t) = 0. \tag{A-4b}$$

By defining $\omega = kc$, equation (A-4b) has the solution

$$T(t) = Ae^{i\omega t} + Be^{-i\omega t}, \tag{A-5}$$

where $A$ and $B$ are real constants to be determined by application of boundary conditions.

Equation (A-4a) is the Helmholtz equation, and requires a bit more care. By dropping the explicit spatial dependence and using subscripts to denote derivatives, it can be written in cylindrical coordinates as

$$S_{\rho\rho} + \frac{1}{\rho}S_\rho + \frac{1}{\rho^2}S_{\phi\phi} + S_{zz} + k^2 S = 0. \tag{A-6}$$

The problem is restricted to two dimension by allowing no variations in the $z$-axis, that is, by making $\frac{\partial}{\partial z} f = 0$ for all functions $f$. The Helmholtz equation is then simplified to

$$S_{\rho\rho} + \frac{1}{\rho} S_\rho + \frac{1}{\rho^2} S_{\phi\phi} + k^2 S = 0. \tag{A-7}$$

Separation of variables is once again used to separate the spatial function $S(\rho, \phi)$ into functions depending on radial and angular coordinates separately, viz.

$$S(\rho, \phi) = R(\rho)\Theta(\phi), \tag{A-8}$$

which allows equation (A-7) to be rearranged as

$$\frac{\rho^2}{R} R_{\rho\rho} + \frac{\rho}{R} R_\rho + k^2 \rho^2 = -\frac{1}{\Theta} \Theta_{\phi\phi}. \tag{A-9}$$

By the same argument as before, non-trivial solutions for the general case exist if and only if both sides are equal to a constant value, chosen without loss of generality to be $n^2$ so that

$$\rho^2 R_{\rho\rho} + \rho R_\rho + k^2 \rho^2 R = n^2, \tag{A-10a}$$

$$\Theta_{\phi\phi} = -n^2 \Theta. \tag{A-10b}$$

The periodicity condition for the angular function $\Theta$ creates the restriction that $n \in \mathbb{Z}$. The solution of equation (A-10b) is given by

$$\Theta(\phi) = C_n \cos(n\phi) + D_n \sin(n\phi), \tag{A-11}$$

where $C_n$ and $D_n$ are real constants to be determined by application of boundary conditions. Alternatively, the angular function can be written

$$\Theta(\phi) = E_n e^{in\phi}, \tag{A-12}$$

where $E_n = C_n - iD_n$ is a complex-valued constant.

Equation (A-10a) is a rescaled form of Bessel's differential equation for the variable $r = k\rho$, which has the solution

$$R(\rho) = F_n J_n(k\rho) + G_n Y_n(k\rho), \tag{A-13}$$

where $F_n$ and $G_n$ are constants to be determined by application of boundary conditions.

The solution of the Helmholtz equation in cylindrical coordinates, for no variations along the $z$-axis, is then given by

$$S(\rho, \phi) = \Big(A_n J_n(k\rho) + B_n Y_n(k\rho)\Big) e^{in\phi}, \tag{A-14}$$

where the new complex constants $A_n$ and $B_n$ are determined by boundary conditions.

By using the definition for the Hankel function of the second kind,

$$H_n^{(2)}(x) = J_n(x) - iY_n(x), \tag{A-15}$$

the Bessel function of the second kind $Y_n(k\rho)$ can be substituted as

$$Y_n(k\rho) = \frac{J_n(k\rho) - H_n^{(2)}(k\rho)}{i}, \tag{A-16}$$

so the solution for the Helmholtz equation can be rewritten

$$S(\rho, \phi) = \Big(a_n J_n(k\rho) + b_n H_n^{(2)}(k\rho)\Big) e^{in\phi}, \tag{A-17}$$

where $a_n$ and $b_n$ are new constants, $n \in \mathbb{Z}$ and no restrictions have been made on the values of $k$.

# B
# Green's Function for the 2D Helmholtz Equation

Consider the inhomogeneous Helmholtz equation in an unbounded two-dimensional domain,

$$(\nabla^2 + k^2)\psi = -f. \tag{B-1}$$

subjected to the Sommerfeld radiation condition

$$\lim_{|\rho|\to\infty} \sqrt{|\rho|}\left(\frac{\partial}{\partial|\rho|} - ik\right)\psi(\rho) = 0, \tag{B-2}$$

where $\rho = \sqrt{x^2 + y^2}$ is the radial polar coordinate.

The Green's function $G(\vec{x}|\vec{x}_0)$ is defined as the solution for a given equation when the source term is given by the impulsive term $f(\vec{x}) = \delta(\vec{x} - \vec{x}_0)$ [41], where $\delta(\vec{x} - \vec{x}_0)$ is the Dirac delta function denoting a unit point source at point $\vec{x}_0$. In the context of systems theory, it can be viewed as the spatial impulse response $h(\vec{x})$ for the system described by the inhomogeneous Helmholtz equation (see Appendix D).

The Green's function for the present problem can thus be found by solving

$$(\nabla^2 + k_0^2)G(\vec{x}|\vec{x}_0) = -\delta(\vec{x} - \vec{x}_0), \tag{B-3}$$

where $k_0$ was used instead of $k$ to represent the fixed wave-number for reasons that will become apparent shortly.

Taking the spatial two-dimensional Fourier transform of eq. (B-3),

$$-k^2\tilde{G}(\vec{k}|\vec{x}_0) + k_0^2\tilde{G}(\vec{x}|\vec{x}_0) = -e^{i\vec{k}\cdot\vec{x}_0}, \tag{B-4}$$

where $\vec{k} = k_x\hat{k_x} + k_y\hat{k_y}$ and $k_x$ is the Fourier variable related to the $x$ spatial coordinate and $k_y$ is the Fourier variable related to the $y$ spatial coordinate.

The Green's function in the spatial Fourier domain is therefore given by

$$\tilde{G}(\vec{k}|\vec{x}_0) = \frac{e^{i\vec{k}\cdot\vec{x}_0}}{k^2 - k_0^2}, \tag{B-5}$$

and the Green's function in the spatial domain is obtained by taking the inverse Fourier transform,

$$G(\vec{x}|\vec{x}_0) = \frac{1}{(2\pi)^2} \int \frac{e^{-i\vec{k}\cdot(\vec{x}-\vec{x}_0)}}{k^2 - k_0^2} \mathrm{d}k_x \mathrm{d}k_y. \tag{B-6}$$

Let $\vec{r} = \vec{x} - \vec{x}_0$ to simplify notation in the calculation that follows. Further, let the $k_x$ and $k_y$ axes be defined such that the position vector $\vec{r}$ lies along the negative $k_x$ axis as in figure B.1.

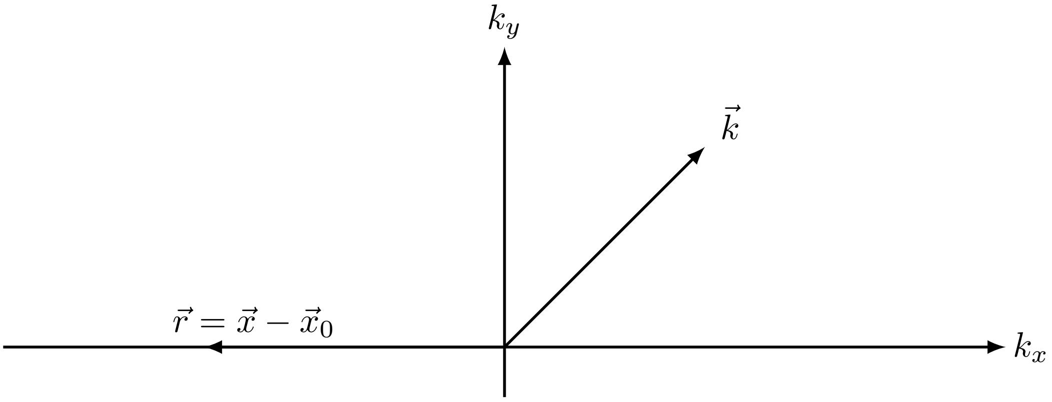

Figure B.1: Cartesian axes in the Fourier-transformed $k$-space.

Defining

$$I(k_x) = \int \frac{1}{k_x^2 + k_y^2 - k_0^2} \mathrm{d}k_y, \tag{B-7}$$

the function being sought is given by

$$G(\vec{r}) = \frac{1}{(2\pi)^2} \int e^{ik_x r} I(k_x) \mathrm{d}k_x. \tag{B-8}$$

To calculate $I(k_x)$, the denominator can be expanded

$$I(k_x) = \int \frac{1}{(k_y + i\sqrt{k_x^2 - k_0^2})(k_y - i\sqrt{k_x^2 - k_0^2})} \mathrm{d}k_y, \tag{B-9}$$

at which point the integral can be carried out in the complex $k_y$ plane. Two situations must be taken into account: the cases where 1) $|k_x| > k_0$ and 2) $|k_x| < k_0$.

For the first case, $|k_x| > k_0$, the integration contour can be closed in the upper or lower half-plane, as shown in figure B.2.

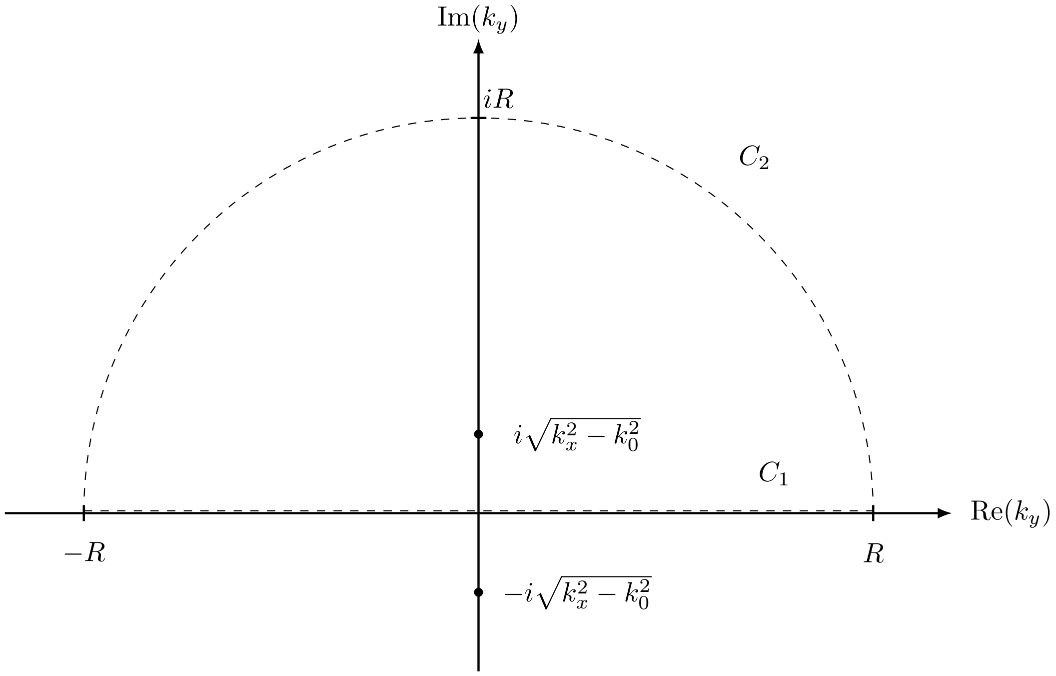

B.2(a): Closing at the upper half-plane.

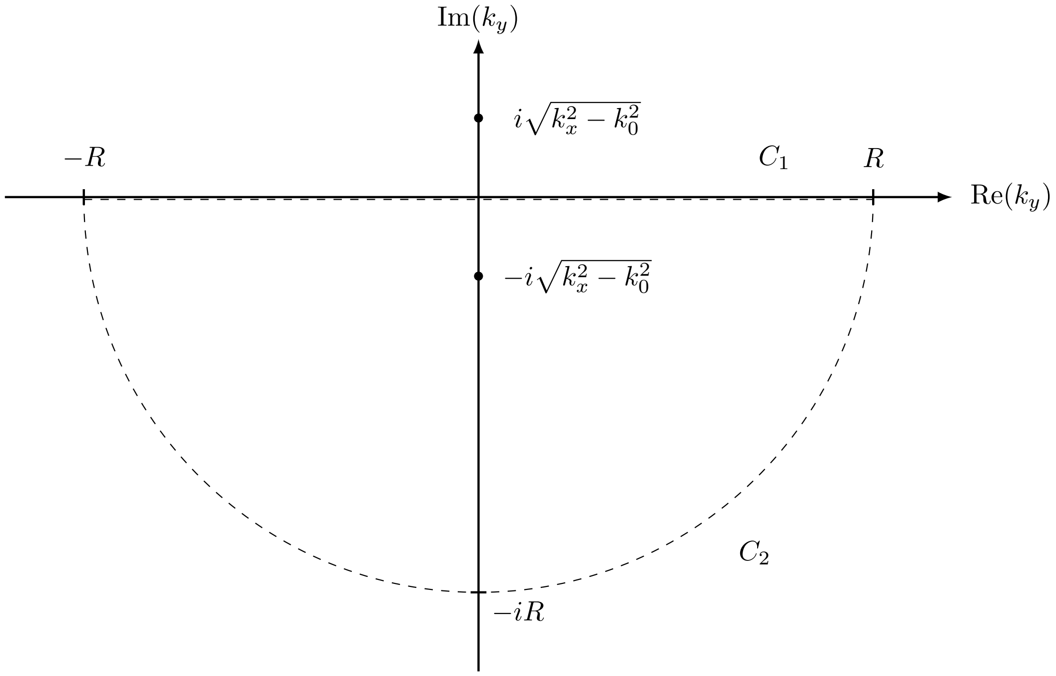

B.2(b): Closing at the lower half-plane.

Figure B.2: Possible closed contours used for the evaluation of $I(k_x)$ when $|k_x| > k_0$.

The residue theorem allows a function $f(z)$ to be evaluated on either of these integration contours as

$$\oint f(z)\mathrm{d}z = \lim_{R\to\infty}\left(\int_{C_1} f(z)\mathrm{d}z + \int_{C_2} f(z)\mathrm{d}z\right) = 2\pi i \sum_p \mathrm{Res}(p), \qquad \text{(B-10)}$$

where the closed path integration is evaluated in the anti-clockwise direction, the summation on the right-hand side is done over all the poles of $f$ and $\mathrm{Res}(p)$ denotes the residue of $f(z)$ at the pole $p$.

For the present case,

$$\lim_{R\to\infty}\int_{C_1} f(z)\mathrm{d}z = \int \frac{1}{(k_y + i\sqrt{k_x^2 - k_0^2})(k_y - i\sqrt{k_x^2 - k_0^2})}\mathrm{d}k_y \tag{B-11}$$

is the integral being sought. Furthermore, due to the appearance of a $k_y^2$ term at the denominator of the integrand, the second integral vanishes when $R \to \infty$ regardless of choice of contour.

If the contour is closed at the upper half-plane, the integral evaluates to the residue at the pole $k_y = i\sqrt{k_x^2 - k_0^2}$,

$$I(k_x) = 2\pi i\,\mathrm{Res}(i\sqrt{k_x^2 - k_0^2}) = \frac{\pi}{\sqrt{k_x^2 - k_0^2}}, \qquad \text{for} \qquad |k_x| > k_0. \tag{B-12}$$

If the contour is closed at the lower half-plane, the integral evaluates to the negative value of the residue at the pole $k_y = -i\sqrt{k_x^2 - k_0^2}$,[1]

$$I(k_x) = -2\pi i\,\mathrm{Res}(-i\sqrt{k_x^2 - k_0^2}) = \frac{\pi}{\sqrt{k_x^2 - k_0^2}}, \qquad \text{for} \qquad |k_x| > k_0, \tag{B-13}$$

which yields the same answer.

For the second case, $|k_x| < k_0$, the denominator can be rewritten again so that

$$I(k_x) = \int \frac{1}{(k_y + \sqrt{k_0^2 - k_x^2})(k_y - \sqrt{k_0^2 - k_x^2})}\mathrm{d}k_y, \tag{B-14}$$

so that there are now two real poles to be dealt with. There are several possibilities for the integration contour to be utilized when evaluating the integral: each pole can be bypassed with an arc extending into the upper or lower half-plane, and the contour can be closed at infinity at the upper or lower half-plane, for a total of 8 possibilities.

The first of those possibilities is shown in figure B.3, in which the residue theorem can be written as

$$\lim_{R\to\infty}\lim_{\epsilon\to 0}\left(\int_{C_1} + \int_{C_2} + \int_{C_3} + \int_{C_4} + \int_{C_5} + \int_{C_6}\right) f(z)\mathrm{d}z = 0, \tag{B-15}$$

since there are no poles within the integration contour.

---

[1] The residue theorem requires the contour to be traversed anti-clock-wise, so closing it on the lower half-plane implies a negative sign to compensate for direction in the $C_1$ path.

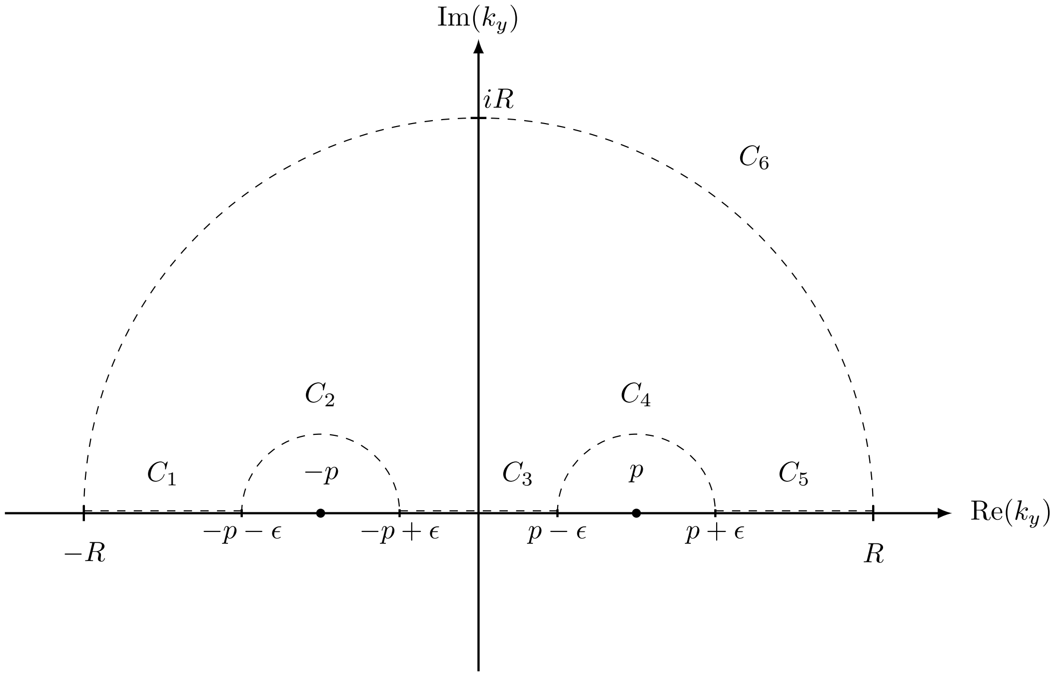

Figure B.3: First possibility for the integration contour used for the evaluation of $I(k_x)$ when $|k_x| < k_0$. The poles are given by $p = \sqrt{k_0^2 - k_x^2}$, omitted from the figure to avoid cluttering.

The integral over path $C_6$ vanishes in the limit $R \to \infty$ because of the $k_y^2$ factor in the denominator. The integral being sought is given by

$$I_1(k_x) = \lim_{R\to\infty} \lim_{\epsilon\to 0} \left( \int_{C_1} + \int_{C_3} + \int_{C_5} \right) f(z)\mathrm{d}z, \tag{B-16}$$

where the subscript denotes the integration path being taken into account. It remains to calculate the integrals over paths $C_2$ and $C_4$. Performing the change of variables $k_y = \epsilon e^{i\theta}$, $\mathrm{d}k_y = i\epsilon e^{i\theta}\mathrm{d}\theta$ allows the integral over $C_2$ to be written as

$$\lim_{\epsilon\to 0} \int_{C_2} f(z)\mathrm{d}z = \lim_{\epsilon\to 0} \int_{-\pi}^{0} \frac{i\epsilon}{(-p+\epsilon e^{i\theta})^2 - p^2}\mathrm{d}\theta = 0, \tag{B-17}$$

where the last step follows from taking the limit before integrating. Likewise, for the $C_4$ path,

$$\lim_{\epsilon\to 0} \int_{C_4} f(z)\mathrm{d}z = \lim_{\epsilon\to 0} \int_{-\pi}^{0} \frac{i\epsilon}{(p+\epsilon e^{i\theta})^2 - p^2}\mathrm{d}\theta = 0, \tag{B-18}$$

so that for this integration contour the integral is given to be

$$I_1(k_x) = 0, \qquad \text{for} \qquad |k_x| < k_0. \tag{B-19}$$

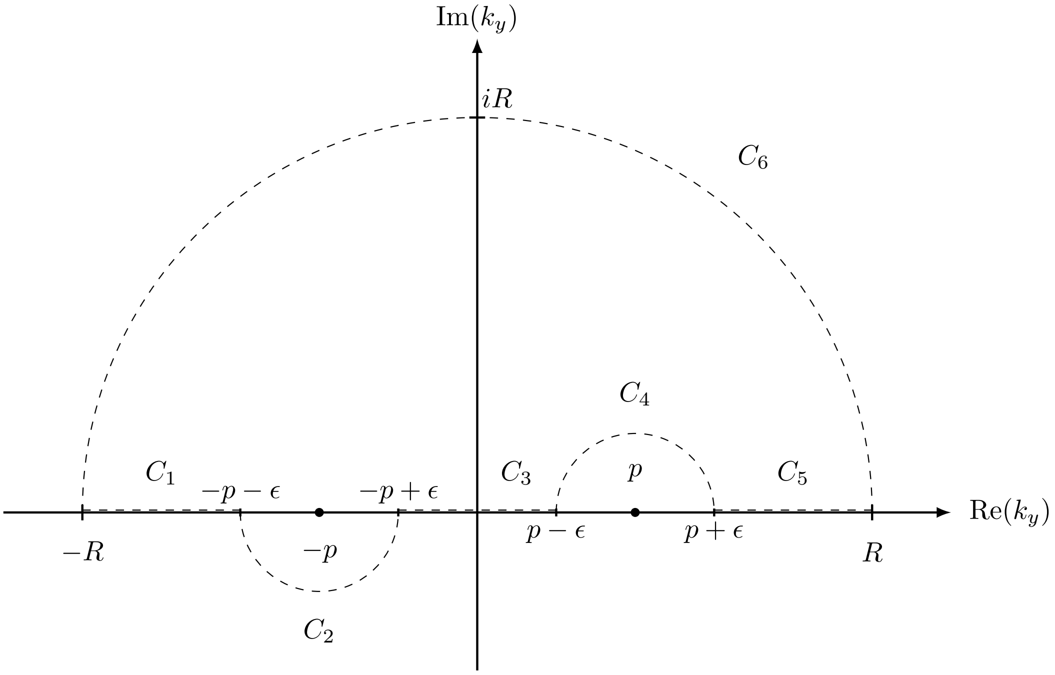

Figure B.4: Second possibility for the integration contour used for the evaluation of $I(k_x)$ when $|k_x| < k_0$. The poles are given by $p = \sqrt{k_0^2 - k_x^2}$, omitted from the figure to avoid cluttering.

For the second possibility, shown in figure B.4, the integration over paths $C_2$, $C_4$ and $C_6$ vanish for the same reasons as in the first possibility. The integral being sought is then straightforwardly calculated

$$I_2(k_x) = \lim_{R\to\infty} \lim_{\epsilon\to 0} \left( \int_{C_1} + \int_{C_3} + \int_{C_5} \right) f(z)\mathrm{d}z = 2\pi i \,\mathrm{Res}(-p), \tag{B-20}$$

so that

$$I_2(k_x) = \frac{\pi i}{2\sqrt{k_0^2 - k_x^2}}, \qquad \text{for} \qquad |k_x| < k_0. \tag{B-21}$$

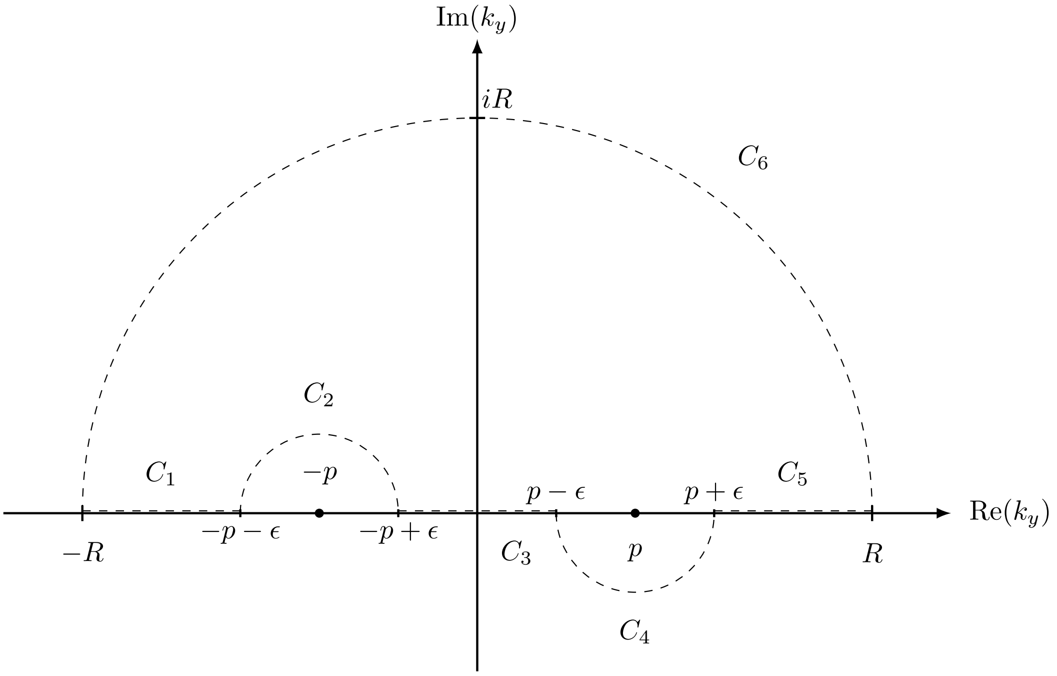

Figure B.5: Third possibility for the integration contour used for the evaluation of $I(k_x)$ when $|k_x| < k_0$. The poles are given by $p = \sqrt{k_0^2 - k_x^2}$, omitted from the figure to avoid cluttering.

The third possibility, shown in figure B.5, is the same case as possibility two except that now

$$I_3(k_x) = \lim_{R\to\infty} \lim_{\epsilon\to 0} \left( \int_{C_1} + \int_{C_3} + \int_{C_5} \right) f(z)\mathrm{d}z = 2\pi i \,\mathrm{Res}(p), \tag{B-22}$$

so that

$$I_3(k_x) = -\frac{\pi i}{2\sqrt{k_0^2 - k_x^2}}, \qquad \text{for} \qquad |k_x| < k_0. \tag{B-23}$$

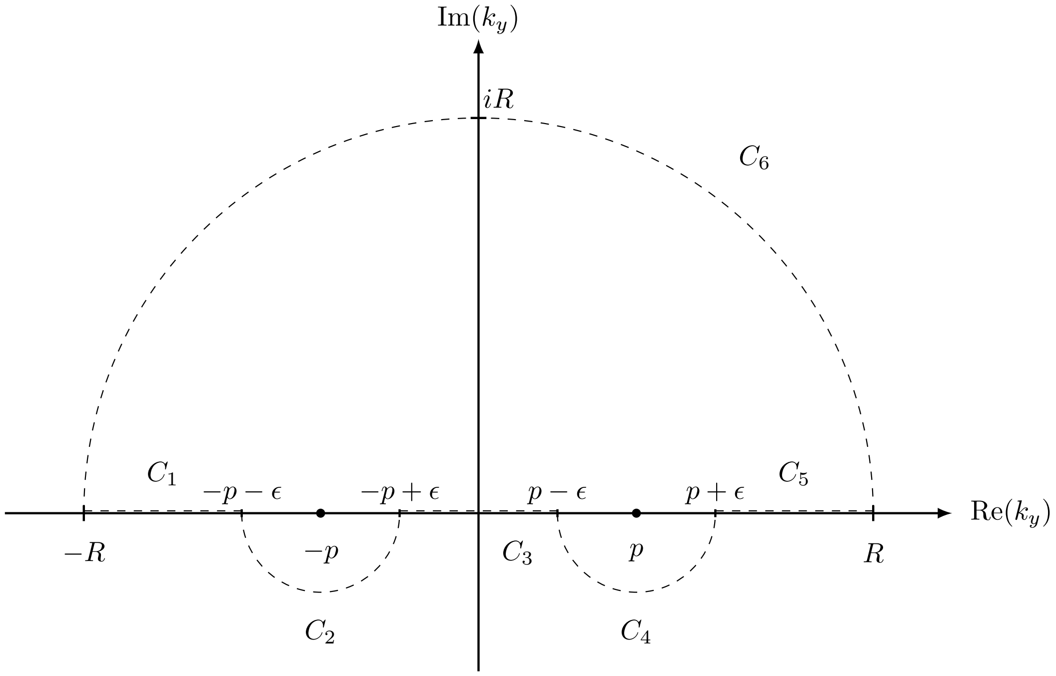

Figure B.6: Fourth possibility for the integration contour used for the evaluation of $I(k_x)$ when $|k_x| < k_0$. The poles are given by $p = \sqrt{k_0^2 - k_x^2}$, omitted from the figure to avoid cluttering.

The fourth possibility, shown in figure B.6, is likewise similar, except that now

$$I_4(k_x) = \lim_{R\to\infty} \lim_{\epsilon\to 0} \left( \int_{C_1} + \int_{C_3} + \int_{C_5} \right) f(z)\mathrm{d}z = 2\pi i \Big( \mathrm{Res}(-p) + \mathrm{Res}(p) \Big), \tag{B-24}$$

so that

$$I_4(k_x) = 0, \qquad \text{for} \qquad |k_x| < k_0. \tag{B-25}$$

The remaining possibilities are given by taking path $C_6$ at the lower half-plane instead of the upper half-plane. This leads to the same results being obtained, but with a change in sign because of the direction the path must be traversed. Therefore there are three possibilities for the integral,

$$I(k_x) = \begin{cases} 0 \\ \frac{\pi i}{2\sqrt{k_0^2 - k_x^2}} \\ -\frac{\pi i}{2\sqrt{k_0^2 - k_x^2}} \end{cases}, \qquad \text{for} \qquad |k_x| < k_0. \tag{B-26}$$

The Green's function for the problem at hand is then given by

$$G(\vec{r}) = \frac{1}{(2\pi)^2} \int\limits_{|k_x|>k_0} \frac{\pi e^{ik_x r}}{\sqrt{k_x^2 - k_0^2}} \mathrm{d}k_x + \frac{1}{(2\pi)^2} \int\limits_{|k_x|<k_0} e^{ik_x r} I(k_x) \mathrm{d}k_x, \tag{B-27}$$

where $I(k_x)$ in the second term can be given by

$$I(k_x) = \begin{cases} 0 \\ \frac{\pi i}{2\sqrt{k_0^2 - k_x^2}} \\ -\frac{\pi i}{2\sqrt{k_0^2 - k_x^2}} \end{cases}, \tag{B-28}$$

and each possibility will be explored. The first possibility, with $I(k_x) = 0$, results in a Green's function given by

$$G_1(\vec{r}) = \frac{1}{(2\pi)^2} \int\limits_{|k_x|>k_0} \frac{\pi e^{ik_x r}}{\sqrt{k_x^2 - k_0^2}} \mathrm{d}k_x. \tag{B-29}$$

By using Euler's formula, it can be written as

$$\begin{aligned} G_1(\vec{r}) &= \frac{1}{(2\pi)^2} \int\limits_{|k_x|>k_0} \frac{\pi \cos(k_x r)}{\sqrt{k_x^2 - k_0^2}} \mathrm{d}k_x + \frac{i}{(2\pi)^2} \int\limits_{|k_x|>k_0} \frac{\pi \sin(k_x r)}{\sqrt{k_x^2 - k_0^2}} \mathrm{d}k_x, \\ &= \frac{1}{(2\pi)^2} \left( \int\limits_{-\infty}^{-k_0} \frac{\pi \cos(k_x r)}{\sqrt{k_x^2 - k_0^2}} \mathrm{d}k_x + \int\limits_{k_0}^{\infty} \frac{\pi \cos(k_x r)}{\sqrt{k_x^2 - k_0^2}} \mathrm{d}k_x + \int\limits_{-\infty}^{-k_0} \frac{i\pi \sin(k_x r)}{\sqrt{k_x^2 - k_0^2}} \mathrm{d}k_x + \int\limits_{k_0}^{\infty} \frac{i\pi \sin(k_x r)}{\sqrt{k_x^2 - k_0^2}} \mathrm{d}k_x \right), \\ &= \frac{1}{(2\pi)^2} \left( 2 \int\limits_{k_0}^{\infty} \frac{\pi \cos(k_x r)}{\sqrt{k_x^2 - k_0^2}} \mathrm{d}k_x \right), \end{aligned} \tag{B-30}$$

where the last step comes from the sine function being an odd function, so that $\sin(k_x r) = -\sin(-k_x r)$ and the integrals cancel each other, and the cosine function being and even function, so that $\cos(k_x r) = \cos(-k_x r)$ and the integrals have the same value.

The change of variables $k_x = k_0 u$, $\mathrm{d}k_x = k_0 \mathrm{d}u$ allows the Green's function to be rewritten as

$$G_1(\vec{r}) = \frac{1}{2\pi} \int\limits_{1}^{\infty} \frac{\cos(k_0 r u)}{\sqrt{u^2 - 1}} \mathrm{d}u. \tag{B-31}$$

By using the integral representation of the Bessel function of the second kind given by

$$Y_\nu(x) = -\frac{2(\frac{1}{2}x)^{-\nu}}{\sqrt{\pi}\Gamma(\frac{1}{2}-\nu)} \int\limits_1^\infty \frac{\cos(xt)}{(t^2-1)^{\nu+\frac{1}{2}}} \mathrm{d}t, \tag{B-32}$$

the Green's function can be written as

$$G_1(\vec{r}) = -\frac{1}{4} Y_0(k_0 r). \tag{B-33}$$

The function $G_1(\vec{r})$ does not vanish at infinity, so it does not fulfil Sommerfeld's radiation condition given by eq. (B-2), and therefore $G_1(\vec{r})$ is not a valid solution for the problem at hand; it can be interpreted, however, as the Green's function for a class of bounded problems.

For the second and third cases, $I(k_x) = \pm\frac{\pi i}{2\sqrt{k_0^2-k_x^2}}$, the Green's function can be written as

$$G_{2,3}(\vec{r}) = -\frac{1}{4} Y_0(k_0 r) \pm \frac{1}{(2\pi)^2} \int\limits_{|k_x|<k_0} \frac{\pi i e^{ik_x r}}{2\sqrt{k_0^2 - k_x^2}} \mathrm{d}k_x. \tag{B-34}$$

By using Euler's formula on the second integral and using the even/odd functions argument, it can be written as

$$\int\limits_{|k_x|<k_0} \frac{\pi i e^{ik_x r}}{2\sqrt{k_0^2-k_x^2}} \mathrm{d}k_x = 2 \int\limits_0^{k_0} \frac{\pi i \cos(k_x r)}{2\sqrt{k_0^2-k_x^2}} \mathrm{d}k_x. \tag{B-35}$$

The change of variables $k_x = k_0 \sin\theta$, $\mathrm{d}k_x = k_0 \cos\theta \mathrm{d}\theta$ allows the integral to be written as

$$\int\limits_0^{k_0} \frac{\cos(k_x r)}{\sqrt{k_0^2-k_x^2}} \mathrm{d}k_x = \int\limits_0^{\frac{\pi}{2}} \frac{\cos(k_0 r \sin\theta)}{\sqrt{k_0^2 - k_0^2 \sin^2\theta}} k_0 \cos\theta \mathrm{d}\theta = \int\limits_0^{\frac{\pi}{2}} \cos(k_0 r \sin\theta) \mathrm{d}\theta. \tag{B-36}$$

By using Bessel's integral

$$J_n(x) = \frac{1}{\pi} \int\limits_0^\pi \cos(x \sin\theta - n\theta) \mathrm{d}\theta, \tag{B-37}$$

the Green's function can be written as

$$G_{2,3}(\vec{r}) = -\frac{1}{4} Y_0(k_0 r) \pm \frac{i}{4} J_0(k_0 r) = \pm\frac{i}{4}\Big(J_0(k_0 r) \pm i Y_0(k_0 r)\Big), \tag{B-38}$$

so that

$$G_2(\vec{r}) = \frac{i}{4}H_0^{(1)}(k_0 r) \qquad \text{and} \qquad G_3(\vec{r}) = -\frac{i}{4}H_0^{(2)}(k_0 r). \tag{B-39}$$

Assuming a time-harmonic dependence of $e^{i\omega t}$, the function $G_2(\vec{r})$ does not fulfil Sommerfeld's radiation condition; it can be interpreted as a wave propagating from infinity and sinking energy at the source point $\vec{x}_0$. Function $G_3(\vec{r})$, however, fulfils the radiation condition, thus it is uniquely the Green's function for a two-dimensional unbounded problem,

$$G(\vec{x}|\vec{x}_0) = -\frac{i}{4}H_0^{(2)}(k|\vec{x}-\vec{x}_0|). \tag{B-40}$$

An important characteristic of this Green's function is its asymptotic behaviour. For observation points far from the source, $k|\vec{x}-\vec{x}_0| \gg 1$, the Hankel function can be expanded so that the far-field Green's function is given by

$$G_f(\vec{x}|\vec{x}_0) \approx -\frac{i}{4}\sqrt{\frac{2}{\pi k|\vec{x}-\vec{x}_0|}}e^{-ik|\vec{x}-\vec{x}_0|}e^{i\frac{\pi}{4}} = C\frac{e^{-ik|\vec{x}-\vec{x}_0|}}{\sqrt{k|\vec{x}-\vec{x}_0|}}, \tag{B-41}$$

which represents a cylindrical wave propagating towards infinity.

# C
# Simpson's Rule

Sympson's rule consists of approximating a function to be integrated by a quadratic polynomial. It provides an improvement in accuracy over linear interpolations used in numerical integration methods (e.g. trapezoidal rule).

Let $f : [a, b] \to \mathbb{R}$ be a function to be integrated over the interval $[a, b]$. Let $m = \frac{a+b}{2}$. The Lagrange form of the interpolating polynomial of degree 2 for $f$ that passes through the nodes $a, b$ and $m$ is given by

$$P(x) = f(a)\frac{(x-m)(x-b)}{(a-m)(a-b)} + f(m)\frac{(x-a)(x-b)}{(m-a)(m-b)} + f(b)\frac{(x-a)(x-m)}{(b-a)(b-m)}. \tag{C-1}$$

The integral being sought can then be approximated as

$$\int_a^b f(x)\mathrm{d}x \approx \int_a^b P(x)\mathrm{d}x. \tag{C-2}$$

The first term of the integral can be calculated as

$$\begin{aligned}
\int_a^b f(a)\frac{(x-m)(x-b)}{(a-m)(a-b)}\mathrm{d}x &= \frac{f(a)}{(a-m)(a-b)}\int_a^b (x-m)(x-b)\mathrm{d}x,\\
&= \frac{f(a)}{(a-m)(a-b)}\int_a^b \Big(x^2 - (m+b)x + mb\Big)\mathrm{d}x,\\
&= \frac{f(a)}{(a-m)(a-b)}\left(\frac{x^3}{3}\bigg|_a^b - (m+b)\frac{x^2}{2}\bigg|_a^b + mbx\bigg|_a^b\right),\\
&= \frac{f(a)}{(a-m)(a-b)}\left(\frac{b^3-a^3}{3} - (m+b)\frac{b^2-a^2}{2} + mb(b-a)\right),\\
&= \frac{f(a)(b-a)}{(a-m)(a-b)}\left(\frac{a^2+ab+b^2}{3} - (m+b)\frac{a+b}{2} + mb\right),\\
&= \frac{-f(a)}{(a-m)}\left(\frac{a^2+ab+b^2}{3} - (m+b)\frac{a+b}{2} + mb\right),\\
&= \frac{-f(a)}{(a-m)}\left(\frac{a^2+ab+b^2}{3} - \frac{a^2+4ab+3b^2}{4} + \frac{ab+b^2}{2}\right),\\
&= \frac{-f(a)}{(a-m)}\left(\frac{1}{12}a^2 + \frac{1}{12}b^2 - \frac{1}{6}ab\right),
\end{aligned}$$

$$
\begin{aligned}
&= \frac{-f(a)}{12(a-m)}\Big(a^2 - 2ab + b^2\Big),\\
&= \frac{-f(a)}{12(a-m)}\Big(a - b\Big)^2,\\
&= \frac{-f(a)}{6(a-b)}\Big(a - b\Big)^2,\\
&= \frac{b-a}{6}f(a). && \text{(C-3)}
\end{aligned}
$$

For the second term,

$$
\begin{aligned}
\int\limits_a^b f(m)\frac{(x-a)(x-b)}{(m-a)(m-b)}\mathrm{d}x &= \frac{f(m)}{(m-a)(m-b)}\int\limits_a^b (x-a)(x-b)\mathrm{d}x,\\
&= \frac{f(m)}{(m-a)(m-b)}\int\limits_a^b \Big(x^2 - (a+b)x + ab\Big)\mathrm{d}x,\\
&= \frac{f(m)}{(m-a)(m-b)}\left(\frac{x^3}{3}\bigg|_a^b - (a+b)\frac{x^2}{2}\bigg|_a^b + abx\bigg|_a^b\right),\\
&= \frac{f(m)}{(m-a)(m-b)}\left(\frac{b^3-a^3}{3} - (a+b)\frac{b^2-a^2}{2} + ab(b-a)\right),\\
&= \frac{f(m)(b-a)}{(m-a)(m-b)}\left(\frac{a^2+ab+b^2}{3} - (a+b)\frac{a+b}{2} + ab\right),\\
&= \frac{f(m)(b-a)}{(m-a)(m-b)}\left(\frac{a^2+ab+b^2}{3} - \frac{a^2+2ab+b^2}{2} + ab\right),\\
&= \frac{f(m)(b-a)}{(m-a)(m-b)}\left(-\frac{1}{6}a^2 + \frac{1}{3}ab - \frac{1}{6}b^2\right),\\
&= \frac{-f(m)(b-a)}{6(m-a)(m-b)}\Big(a^2 - 2ab + b^2\Big),\\
&= \frac{-f(m)(b-a)}{6(m-a)(m-b)}\Big(a - b\Big)^2,\\
&= \frac{-f(m)(b-a)}{6(-\frac{a}{2}+\frac{b}{2})(\frac{a}{2}-\frac{b}{2})}\Big(a - b\Big)^2,\\
&= \frac{-f(m)(b-a)}{-\frac{6}{4}(a-b)^2}\Big(a - b\Big)^2,\\
&= \frac{b-a}{6}4f(m). && \text{(C-4)}
\end{aligned}
$$

For the third term, by recognizing that $(b-m) = -(a-m)$, the integrand has the same form as the first term, and so its contribution is given by

$$
\int\limits_a^b f(b)\frac{(x-a)(x-m)}{(b-a)(b-m)}\mathrm{d}x = \frac{b-a}{6}f(b). \tag{C-5}
$$

Collecting terms,

$$\int_a^b f(x)\mathrm{d}x \approx \frac{b-a}{6}\Big(f(a) + 4f(\frac{a+b}{2}) + f(b)\Big), \tag{C-6}$$

which is Simpson's rule.

The error of the approximation obtained by Simpson's rule is given by

$$E = \int_a^b f(x)\mathrm{d}x - \int_a^b P(x)\mathrm{d}x, \tag{C-7}$$

which can be expanded as

$$\begin{aligned} E &= \int_a^b \Big(f(x) - P(x)\Big)\mathrm{d}x, \\ &= \int_a^b \Big((x-a)(x-m)(x-b)f[a,m,b,x]\Big)\mathrm{d}x, \end{aligned} \tag{C-8}$$

where $f[a,m,b,x]$ is the 3rd order Newton divided difference of $f$. In general, the $n^{\text{th}}$ order Newton divided difference of $f$ can be written as

$$f[x_0, x_1, ..., x_n, x] = \frac{f^{n+1}(\xi)}{(n+1)!}, \qquad \text{for some } \xi \in [x_0, x_n] \tag{C-9}$$

or alternatively as

$$f[x_0, x_1, ..., x_n] = \frac{f[x_1, ..., x_n] - f[x_0, x_1, ..., x_{n-1}]}{x_n - x_0}. \tag{C-10}$$

Before returning to equation (C-8), let $g(x)$ be an auxiliary function defined by

$$g(x) = \int_a^x \Big((y-a)(y-m)(y-b)\Big)\mathrm{d}y, \tag{C-11}$$

so that the error can be written as

$$E = \int_a^b \Big(g'(x)f[a,m,b,x]\Big)\mathrm{d}x. \tag{C-12}$$

Integrating by parts,

$$E = g(x)f[a,m,b,x]\Big|_a^b - \int_a^b \Big(g(x)f'[a,m,b,x]\Big)\mathrm{d}x. \tag{C-13}$$

The first term is zero because $g(a) = g(b) = 0$, from the definition of the auxiliary function $g$. For the second term, the relationship $f'[x_0, ..., x_n, x] = f[x_0, ..., x_n, x, x]$ can be used so that

$$E = -\int_a^b \Big( g(x) f[a, m, b, x, x] \Big) \mathrm{d}x. \tag{C-14}$$

Using definition (C-9), for some $\xi \in [a, b]$,

$$\begin{aligned}
E &= -\frac{f^4(\xi)}{4!} \int_a^b \Big( g(x) \Big) \mathrm{d}x, \\
&= -\frac{f^4(\xi)}{4!} \int_a^b \Bigg( \int_a^x \Big( (y-a)(y-m)(y-b) \Big) \mathrm{d}y \Bigg) \mathrm{d}x, \\
&= -\frac{f^4(\xi)}{24} \int_a^b \Big( -abm + abx + amx - ax^2 + bmx - bx^2 - mx^2 + x^3 \Big) \mathrm{d}x, \\
&= -\frac{f^4(\xi)}{24} \int_a^b \Big( -\frac{a^2b}{2} + \frac{a^2x}{2} - \frac{ab^2}{2} + 2abx - \frac{3ax^2}{2} + \frac{b^2x}{2} - \frac{3bx^2}{2} + x^3 \Big) \mathrm{d}x, \\
&= -\frac{f^4(\xi)}{24} \Big( -\frac{1}{120}(a-b)^5 \Big), \\
&= -\frac{f^4(\xi)}{24} \Bigg( \frac{15}{4} \Big( \frac{b-a}{2} \Big)^5 \Bigg), \\
&= -\frac{f^4(\xi)}{90} \Big( \frac{b-a}{2} \Big)^5,
\end{aligned} \tag{C-15}$$

which confirms the superior accuracy of Simpson's rule.

# D
# Linear Time-Invariant Systems

The Dirac delta function can be defined e.g. as the limit

$$\delta(t) = \lim_{\Delta \to 0} \delta_\Delta(t), \tag{D-1}$$

where $\delta_\Delta(t)$ is the scaled normal distribution given by

$$\delta_\Delta(t) = \frac{1}{\Delta\sqrt{\pi}} e^{-\frac{t^2}{\Delta^2}}. \tag{D-2}$$

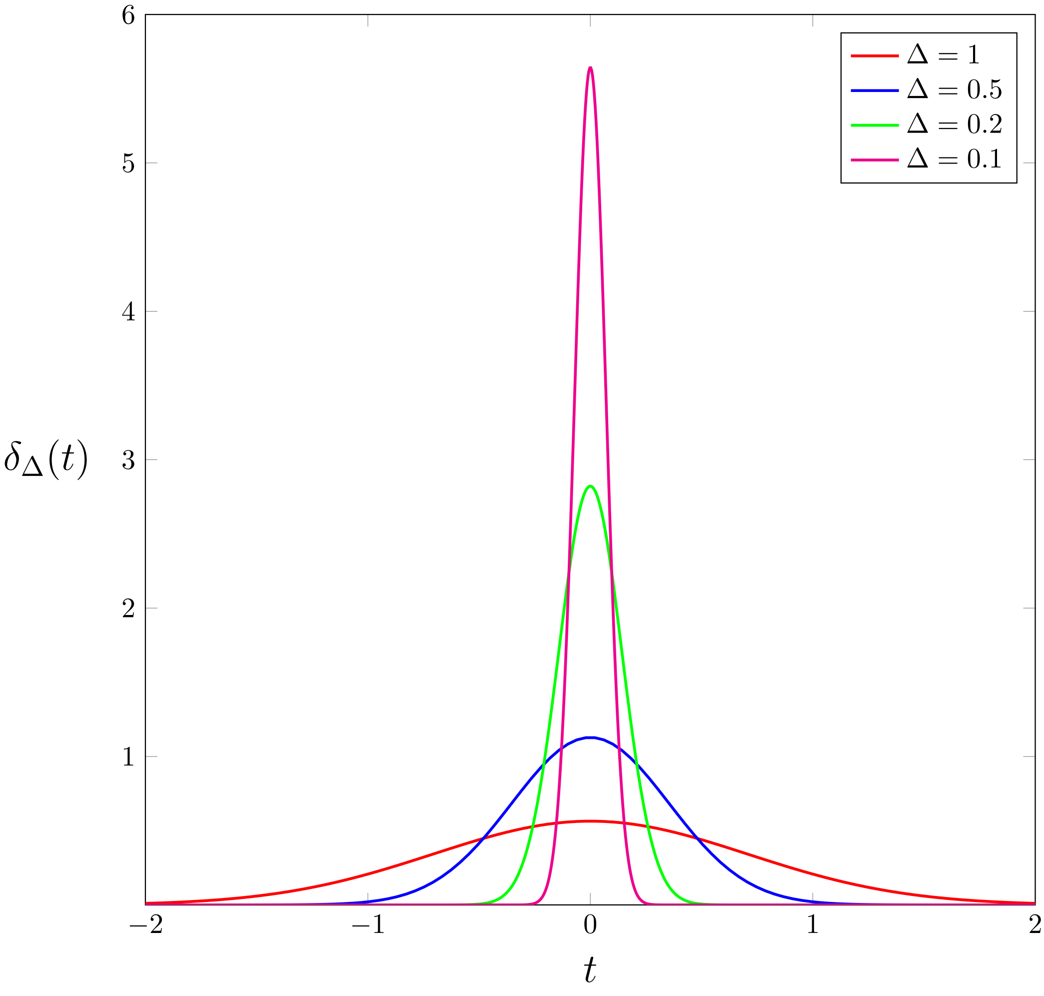

Figure D.1: Possible construction of the Dirac delta function.

Without getting into too many mathematical details, an important property of the Dirac delta function is that it forms an orthonormal basis in an appropriate space of functions, that is, a function $f$ can be written as

$$f(t) = \int f(\tau)\delta(\tau - t)\mathrm{d}\tau. \tag{D-3}$$

This property allows for the study of linear time-invariant (LTI) systems, depicted in figure D.2, in a simple way: by knowing the response of a system to the Dirac delta function $\delta(t)$, denoted by $h(t)$ and called the *impulse response*, the response of an LTI system to an arbitrary input $x(t)$ can be constructed as a superposition of impulse responses, viz.

$$y(t) = \int h(t)x(\tau)\mathrm{d}\tau. \tag{D-4}$$

By using property (D-3) to expand the input, the response can be written

$$y(t) = \int h(\tau)x(t - \tau)\mathrm{d}\tau = h(t) * x(t), \tag{D-5}$$

which is the convolution representation for an arbitrary output of an LTI system.

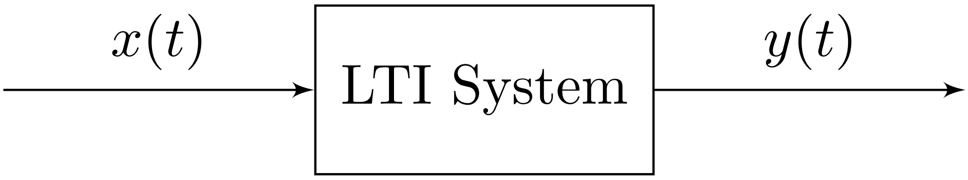

Figure D.2: Block diagram showing a Linear Time-Invariant (LTI) system.

Further analysis of LTI system can be made by employing the Fourier transform defined by

$$\tilde{f}(\omega) = \mathcal{F}f(t) = \int f(t)e^{-i\omega t}\mathrm{d}t \tag{D-6}$$

An LTI system described in the time domain can be characterized by its impulse response $h(t)$; likewise, for analysis in the frequency domain, the system can be characterized by $H(\omega) = \mathcal{F}h(t)$, called the *transfer function* of the system. By applying the Fourier transform to equation (D-5), and exploiting the convolution property of the Fourier transform,

$$Y(\omega) = H(\omega)X(\omega). \tag{D-7}$$

Now let the input to a given LTI system be given by the harmonic function $x(t) = e^{i\omega_0 t}$, where $\omega_0$ is some fixed frequency. The output will be given by application of the convolution integral,

$$\begin{aligned} y(t) &= \int h(\tau)x(t-\tau)\mathrm{d}\tau, \\ &= \int h(\tau)e^{i\omega_0(t-\tau)}\mathrm{d}\tau, \\ &= e^{i\omega_0 t}\int h(\tau)e^{-i\omega_0\tau}\mathrm{d}\tau. \end{aligned} \tag{D-8}$$

The integral on the right-hand side of (D-8) can be recognized as the transfer function of the system at the point $\omega = \omega_0$, that is,

$$y(t) = H(\omega_0)e^{i\omega_0 t} = H(\omega_0)x(t), \tag{D-9}$$

which shows that exponentials are the eigenfunctions of LTI systems, with eigenvalue given by the system's transfer function at the corresponding point to the frequency of the exponential.

This result also shows that, for electromagnetic problems, the response of a particular system to an harmonic excitation given by $e^{i\omega_0 t}$ is equal in magnitude to the impulse response of that system for that particular frequency, that is,

$$|y(t)| = |H(\omega_0)e^{i\omega_0 t}| = |H(\omega_0)|, \tag{D-10}$$

which allows results from time-domain simulation methods and electromagnetic techniques in the frequency domain to be readily compared.

# Bibliography

[1] RAYNER, J. P.; WHICHELLO, A. P. ; CHEETHAM, A. D. **Plasma Science, IEEE Transactions on.** Physical characteristics of plasma antennas, journal, v.32, n.1, p. 269–281, 2004.

[2] HARGREAVE, M.; RAYNER, J.; CHEETHAM, A.; FRENCH, G. ; WHICHELLO, A. **Coupling power and information to a plasma antenna.** In: PLASMA PHYSICS: 11TH INTERNATIONAL CONGRESS ON PLASMA PHYSICS: ICPP2002, volume 669, p. 388–391. AIP Publishing, 2003.

[3] WHICHELLO, A.; RAYNER, J. ; CHEETHAM, A. **Plasma antenna radiation patterns.** In: PLASMA PHYSICS: 11TH INTERNATIONAL CONGRESS ON PLASMA PHYSICS: ICPP2002, volume 669, p. 396–399. AIP Publishing, 2003.

[4] BORG, G.; HARRIS, J.; MARTIN, N.; THORNCRAFT, D.; MILLIKEN, R.; MILJAK, D.; KWAN, B.; NG, T. ; KIRCHER, J. **Physics of Plasmas (1994-present).** Plasmas as antennas: Theory, experiment and applications, journal, v.7, n.5, p. 2198–2202, 2000.

[5] MOISAN, M.; ZAKRZEWSKI, Z. **Journal of Physics D: Applied Physics.** Plasma sources based on the propagation of electromagnetic surface waves, journal, v.24, n.7, p. 1025, 1991.

[6] CHEETHAM, A.; RAYNER, J.; GILBERT, B. ; FRENCH, G. **Surface wave excitation for plasma antenna applications.** In: PROC 23RD AINSE CONFERENCE ON PLASMA SCIENCE AND TECHNOLOGY, p. 17–19, 2000.

[7] KUMAR, R.; BORA, D. **Journal of Applied Physics.** A reconfigurable plasma antenna, journal, v.107, n.5, p. 053303, 2010.

[8] RUSSO, P.; CERRI, G. **Analysis of a reconfigurable plasma antenna.** In: 2016 10TH EUROPEAN CONFERENCE ON ANTENNAS AND PROPAGATION (EUCAP), p. 1–5. IEEE, 2016.

[9] FERRERO, F.; LIZZI, L.; STARAJ, R.; RIBERO, J.-M. ; OTHERS. **IEEE Antennas and Wireless Propagation Letters**. Reconfigurable antenna for future spectrum reallocations in 5g communications, journal, v.15, p. 1297–1300, 2016.

[10] MAJID, H. A.; ABD RAHIM, M. K.; HAMID, M. R. ; ISMAIL, M. F. **Progress In Electromagnetics Research**. Frequency reconfigurable microstrip patch-slot antenna with directional radiation pattern, journal, v.144, p. 319–328, 2014.

[11] HAUPT, R. L.; LANAGAN, M. **IEEE Antennas & Propagation Magazine**. Reconfigurable antennas, journal, v.55, n.1, p. 49–61, 2013.

[12] CHEN, F. **Introduction to Plasma Physics and Controlled Fusion**. New York: Plenum Press, 1984.

[13] KARDAR, M. **Statistical Physics of Particles**. Cambridge University Press, 2007.

[14] CERCIGNANI, C. **Theory and application of the Boltzmann equation**. Scottish Academic Press, 1975.

[15] VLASOV, A. **Physics-Uspekhi**. The vibrational properties of an electron gas, journal, v.10, n.6, p. 721–733, 1968.

[16] CHOQUET, I.; DEGOND, P. ; LUCQUIN-DESREUX, B. **Mathematical and Computer Modelling**. A strong ionization model in plasma physics, journal, v.49, n.1, p. 88–113, 2009.

[17] SHANKAR, R. **Principles of Quantum Mechanics**. Plenum, 1994.

[18] ARNOLD, V. I. **Mathematical Methods of Classical Mechanics**, volume 60. Springer Science & Business Media, 1989.

[19] ALBUQUERQUE, J. P. D. A. E.; FORTES, J. M. P. ; FINAMORE, W. A. **Probabilidade, Variáveis Aleatórias e Processos Estocásticos**. Interciência: PUC-Rio, 2008.

[20] BITTENCOURT, J. A. **Fundamentals of Plasma Physics**. Springer Science & Business Media, 2013.

[21] LASSEN, H. **Jahrb. drahtl. Tel**. Über die ionisation der atmosphäre und ihren einfluß auf die ausbreitung der kurzen elektrischen wellen der drahtlosen telegraphie, journal, v.28, p. 109–139, 1926.

[22] ISHIMARU, A. **Electromagnetic wave propagation, radiation, and scattering**. Prentice-Hall, 1991.

[23] CHEW, W. C. **Waves and fields in inhomogeneous media**, volume 522. IEEE press New York, 1995.

[24] HELALY, A.; SOLIMAN, E. ; MEGAHED, A. **IEE Proceedings-Microwaves, Antennas and Propagation**. Electromagnetic waves scattering by nonuniform plasma cylinder, journal, v.144, n.2, p. 61–66, 1997.

[25] BALANIS, C. A. **Advanced engineering electromagnetics**. John Wiley & Sons, 2012.

[26] MOON, H.; TEIXEIRA, F. L. ; OMELCHENKO, Y. A. **Computer Physics Communications**. Exact charge-conserving scatter–gather algorithm for particle-in-cell simulations on unstructured grids: A geometric perspective, journal, v.194, p. 43–53, 2015.

[27] NA, D.-Y.; MOON, H.; OMELCHENKO, Y. A. ; TEIXEIRA, F. L. **IEEE Transactions on Plasma Science**. Local, explicit, and charge-conserving electromagnetic particle-in-cell algorithm on unstructured grids, journal, v.44, n.8, p. 1353–1362, 2016.

[28] ELIASSON, B. **Numerical vlasov–maxwell modelling of space plasma**, 2002.

[29] ELIASSON, B. **Transport Theory and Statistical Physics**. Numerical simulations of the fourier-transformed vlasov-maxwell system in higher dimensions—theory and applications, journal, v.39, n.5-7, p. 387–465, 2010.

[30] TAFLOVE, A.; HAGNESS, S. C. **Computational Electrodynamics**. Artech house, 2005.

[31] SCHNEIDER, J. B. **Understanding the Finite-Difference Time-Domain Method**. www.eecs.wsu.edu/ schneidj/ufdtd, 2010.

[32] STRAUSS, W. A. **Partial differential equations**, volume 92. Wiley New York, 1992.

[33] YEE, K. S. **IEEE Trans. Antennas Propag**. Numerical solution of initial boundary value problems involving maxwell's equations in isotropic media, journal, v.14, n.3, p. 302–307, 1966.

[34] COURANT, R.; FRIEDRICHS, K. ; LEWY, H. **Mathematische annalen**. Über die partiellen differenzengleichungen der mathematischen physik, journal, v.100, n.1, p. 32–74, 1928.

[35] ENGQUIST, B.; MAJDA, A. **Mathematics of Computation**. Absorbing boundary conditions for the numerical simulation of waves, journal, v.31, p. 629–651, 1977.

[36] ATKINSON, K. E. **An introduction to numerical analysis**. John Wiley & Sons, 2008.

[37] OPPENHEIM, A. V.; WILLSKY, A. S. ; HAMID, S. **Signals and Systems**. Pearson, 1996.

[38] RICHMOND, J. **IEEE Transactions on Antennas and Propagation**. Scattering by a dielectric cylinder of arbitrary cross section shape, journal, v.13, n.3, p. 334–341, 1965.

[39] BUSSEY, H.; RICHMOND, J. H. **IEEE Transactions on Antennas and Propagation**. Scattering by a lossy dielectric circular cylindrical multilayer, numerical values, journal, v.23, p. 723–725, 1975.

[40] FRANKLIN, R. N. **Plasma phenomena in gas discharges**. Oxford and New York, Clarendon Press, 1976.

[41] COUTO, R. T. **Revista Brasileira de Ensino de Física**. Green's functions for the wave, helmholtz and poisson equations in a two-dimensional boundless domain, journal, v.35, n.1, p. 01–08, 2013.